University of Alberta

Understanding zinc sulfide activation mechanism and impact of calcium sulfate in sphalerite flotation

by

Fucheng Teng

A thesis submitted to the Faculty of Graduate Studies and Research
in partial fulfillment of the requirements for the degree of

Master of Science
in
Chemical Engineering

Department of Chemical and Materials Engineering

Spring 2012
Edmonton, Alberta

Abstract

Quartz crystal microbalance with dissipation (QCM-D) was used to study the zinc sulfide activation with silver, copper and lead. The interactions between calcium sulfate and minerals and gypsum nucleation on functional surfaces were investigated using a QCM-D, surface forces apparatus (SFA), and atomic force microscope (AFM).

This study is the first of its kind to apply the QCM-D technique to investigate sphalerite activation, which indroduces a new *in-situ* approach to investigate surface adsorption and activation in many mineral processes and surface modifications. The fitting of adsorption of copper and lead species to sphalerite at pH 6.5 and 9 with kinetic models indicates that the activation in this pH range is a chemisorption process. Gypsum was found to grow on functional surfaces following the growth rates as -COOH>-OH>-CH_3, but not on sphalerite. The uptake of copper and adsorption of xanthate on sphalerite could be retarded in the presence of calcium sulfate.

Acknowledgement

I would like to thank my supervisors, Dr. Qingxia (Chad) Liu and Dr. Hongbo Zeng, for their guidance, encouragement and support throughout the course of this study. It is Chad who guides me into the world of mineral processing with his immense knowledge and experience. He has been always supportive and has given me a lot of creative ideas when I was stuck in the middle of the experiment. I could not gain so much knowledge without his immeasurably valuable advice. I am also very grateful to Hongbo. He taught me how to conduct rigorous research, how to write a scientific paper and many other things about being a researcher. I still can remember how thrilled I was to perform the first SFA experiment with him and many discussions we had to revise the manuscript word by word.

I would also like to thank Dr. Zhenghe Xu for his invaluable suggestions and allowing me to use all the instruments in oil sands research lab. Thanks also go to Mr. Jim Skwarok, Ms. Shiau-Yin Wu, and Ms. Jie Ru for giving me many instrument trainings and creating such a friendly laboratory environment. I would like to thank Drs. Dimitre Karpuzov, Shihong Xu, Anquang He at ACSES for their help in XPS, AES, FTIR and AES measurements. Thanks Ms. Ni Yang at OSCIEF for FTIR test and many helpful discussions on monolayer preparation, Mr. Shiraz Merali for XRD measurement and his help in analyzing the results. Appreciation also goes to Dr. Qi Liu, Dr. Mingli Cao and my friend Peng Huang for permitting to work in their lab and showing me how to use Hallimond tube.

I thank all the members of Dr. Liu's, Dr. Zeng's and Dr. Xu's groups. I had great pleasure to work with them during the past two years.

The financial support from Teck Metal Ltd, Collaborative Research and Development (CRD) Grant of the NSERC, NSERC Discovery Grant Award and an NSERC RTI Grant Award is acknowledged.

Finally, I would like to thank my parents and my wife Lilian Li who stand beside me all the time. Without their support and comfort, I could not go this far.

Table of Contents

List of tables

List of Figures

List of Symbols

K	Equilibrium constant
Δm	Adsorbed mass on a QCM-D sensor, ng/cm^2
n	Number of harmonic overtones of the QCM-D sensor, n=1, 3, 5, 7, 9, 11, 13
C	Constant of the QCM-D sensor, C=17.7ng/(Hz•cm^2) in this study
f, Δf	Frequency and frequency shift, Hz
Γ	The quantity of adsorbed mass, g or mol
t	Time, s
α	Desorption constant, g/(cm^2•s)
β	Initial adsorption rate, g/cm^2
s	The probability that one activator atom jumps to a lattice site
v	The ionic vibration frequency
k	Boltzmann constant
T	Absolute temperature
ΔE	Activation energy, J/m^2
k_{ad}	Adsorption constant
k_d	Desorption constant
Φ ,Φ_0	Concentration of surface sites at time t=t and t=0
θ, θ_e	Surface coverage and equilibrium surface coverage
q, q_e	the quantity of solute sorbed at time t and equilibrium, g or mol
k_1	Apparent adsorption constant for pseudo-first order
k_2	Apparent adsorption constant for pseudo-second order
m	the number of solute molecules adsorbing onto one vacant surface site
r	The jumping rate of one molecule onto a vacant surface site
Z	The collision frequency

ρ	Steric factor
E_a	Energy barrier, J/m^2
R	Gas constant
$[A]$	Concentration of solute in bulk, mol/m^3
ΔG	Gibbs free energy, J/m^2
γ, γ_{eff}	Surface energy and effective surface energy, J/m^2
γ^{LW}	Lifshitz–van der Waals component of surface energy, J/m^2
γ^{+}	Lewis acid component of surface energy, J/m^2
γ^{-}	Lewis base component of surface energy, J/m^2
γ^{AB}	Lewis acid base component of surface energy, J/m^2
θ_i	Contact angle of i liquid on solid surface, °
$\gamma_{ZnS-Gyp}$	Interfacial energy between ZnS and gypsum, J/m^2
$\gamma_{ZnS-Solution}$	Interfacial energy between ZnS and solution, J/m^2
$\gamma_{Gyp-Solution}$	Interfacial energy between gypsum and solution, J/m^2
D	Normal distance between two surfaces, m
$E_{VDW}(D)$	The van der Waal energy per unit between two flat surfaces across with a separation distance, J/m^2
$E_{EDL}(D)$	The electrical double-layer energy per unit between two flat surfaces across with a separation distance, J/m^2
$E_{TOTAL}(D)$	the total interaction energy including van der Waal and electrical double-layer energies between two flat surfaces with a separation distance, J/m^2
$F(D)/R$	the interaction forces between two mica surfaces in crossed-cylinder geometry with radius of R in SFA measurement, mN/m
F_{ad}	Adhesion force, mN/m
W, W_{eff}	The work of adhesion and the effective work of adhesion, J/m^2
$A_{mica\text{-}water\text{-}mica}$	Hamaker constant for mica-water-mica system, J
N_A	Avogadro constant
ψ	surface potential of mica surface, mV

κ	Debye length, nm^{-1}
$f(z)$	The height distribution of asperities
E	Plane stress modulus, GPa
z	The height of a asperity, m
μ	The mean height of asperities, m
$E_{Dissipated}$	The energy dissipated during one period of oscillation, J/m^2
E_{Stored}	The energy stored in the oscillating system, J/m^2

List of Acronyms

AFM	Atomic force microscope
FTIR	Fourier transform infrared spectroscopy
GIXRD	Grazing incidence X-ray diffraction
PAX	Potassium amyl xanthate
QCM-D	Quartz crystal microbalance with dissipation
SEM	Scanning electron microscope
XPS	X-ray photoelectron spectroscopy

Chapter 1 Introduction

1.1 Sphalerite flotation

Zinc sulfide is the most important source of zinc, the fourth most common metal in use with an annual production of about 12 million tonnes [1]. Zinc occurs in nature in two main forms: sphalerite and wurtzite. The main difference between them is shown in Table 1.1. Most researchers who studied flotation properties of zinc sulfide do not distinguish between sphalerite and wurtzite, and they have either known or assumed the samples to be sphalerite. In this thesis, all the research was focused on sphalerite, although it should be noted that the reactivity of wurtzite is probably different from that of sphalerite. In the majority of commercially important deposits, sphalerite is often associated with copper or lead sulfides, sometimes in binary mixtures and sometimes together with pyrite and pyrrhotite in ternary or more complex mixtures [2]. The flotation technology of sphalerite has therefore focused on the separation of it from copper sulfide, iron sulfide, galena and other gangues. The typical sulfides flotation process involves:

1) Grinding ores to particles with certain sizes;
2) Mixing ground particles with water to form a slurry mixture;
3) Adding collector, mostly xanthate for sulfides, into the slurry (some sulfide minerals (e.g. molybdenite) can be floated without collector addition [3]);
4) Bubbling air into the slurry so that some mineral particles adhering to air bubbles due to hydrophobic force rise up and are collected as froth on the top of the slurry.

By collecting the froth, the separation of desired minerals from others is attained. Different from other sulfide minerals, the flotation behaviour of sphalerite has two distinct features. First, it responds poorly to short-chain thiol collectors [4]. Second, it can be activated for flotation by thiols if it is treated with copper and other heavy metal salts [2].

Table 1.1 Physical properties comparison of sphalerite and wurtzite

Property	Sphalerite	Wurtzite
Crystal structure	Cubic	Hexagonal
Lattice constants (A)	a=5.4093	a=3.8226; b=6.2605
Zn-S distance (A)	2.35	2.25
Zn-Zn distance	3.83	2.25
Free energy of formation (Kj per mole)	-198.5	-187
Solubility product	2.57×10^{-26}	5.1×10^{-25}
Band gap (eV)	3.7	-
Adsorption edge (nm)	3.41	-
Cleavage face	110	1120

1.1.1 Sphalerite activation

Activation, defined by Finkelstein and Allison [2], is a process whereby the surface of a mineral surface is modified so as to make it react more readily or more strongly with a collector. A number of transition metal cations, including cupric, lead, silver and cadmium ions, have been reported to successfully activate sphalerite. The most frequently cited driving force for the activation reaction is the solubility difference between zinc sulfide and other metal sulfides as show in Table 1.2.

Table 1.2 Equilibrium constants for metal sulfides dissolution at 25 °C [5]

Metal Sulfides	K^1
Ag_2S	5×10^{-51}
CuS	5×10^{-37}
PbS	3×10^{-28}
CdS	7×10^{-28}
ZnS	2×10^{-25}
FeS	5×10^{-19}
MnS	3×10^{-14}

K^1 is the equilibrium constant for the reaction $M_nS(s)+H_2O\leftrightarrow nM^{2/n+}+OH^-+HS^-$

Take sphalerite activation by cupric ion as an example, the activation mechanism under acidic condition is represented by following equation 1.1:

$$ZnS_{(s)} + Cu^{2+} \leftrightarrow CuS_{(s)} + Zn^{2+} \qquad 1.1$$

The reaction equilibrium constant for equation 1.1 is

$$K = \frac{[Zn^{2+}]}{[Cu^{2+}]} = \frac{K_{ZnS}^{1}}{K_{CuS}^{1}} = 4\times10^{11} \qquad 1.2$$

By following equation 1.1, the surface of sphalerite turns to be copper sulfide. The xanthate collector can then react with the activation product, copper sulfide, to form an insoluble copper xanthate via an electrochemical reaction:

$$CuS_{(surface\ )} + 2EX^{-} \leftrightarrow Cu(EX)_{2(surface\ )} + S^{0} + 2e \qquad 1.3$$

The formed copper (II) xanthate is instable and can decompose to copper (I) xanthate via following reaction:

$$Cu(EX)_{2(surface\ )} \leftrightarrow CuEX_{(surface\ )} + \frac{1}{2}(EX)_{2} \qquad 1.4$$

The xanthate adsorption products render the activated sphalerite surface hydrophobic, facilitating the lifting by air bubbles.

This overall subject of sphalerite activation has been investigated extensively over decades, and both operation of plant processing of sphalerite and experimental work on natural and synthetic sphalerite have established following:

1) Sphalerite can be activated by the other heavy metal ions whose sulfides have smaller solubility than sphalerite. Under acidic condition, the activation can be represented by following equation for divalent ions [6]:

$$ZnS_{(s)} + M^{2+} \leftrightarrow MS_{(s)} + Zn^{2+} \qquad 1.5$$

2) The exchange of Zn^{2+} by Cu^{2+} occurring on the sphalerite surface under acidic condition is almost equimolar [7].

3) At acidic pH, the activation reaction takes place in two stages-a very fast step followed by a slower step [6, 8].

4) Some researchers have tried to fit the two-stage reaction by different mathematical equations, but not widely accepted by others [6].

5) At alkaline pH (7-10), the sphalerite still can be floated by adding activator (cupric or lead ions). Most researchers speculate that metal hydroxide or monohydroxide firstly adsorbs onto the sphalertite surface and then transforms to

metal sulfide [9-11]. However, no direct experimental evidence has been presented to prove this speculation.

6) For sphalerite activation by lead, there are more disputes than other activators. Theoretical calculation and simulation show that the aforementioned exchange process is not energetically favourable at acidic pH [12]. Pattick et al. [12] proposed another mechanism involving the formation of Pb-oxide species which become a point of attachment of xanthate sulphur to the lead. However, this has not been experimentally proved. Under alkaline condition, Rashchi et al.[13] found that sphalerite recovery started to drop from pH 7, and there was almost no recovery at pH 11. It is worthy mention that if the sphalerite was conditioned at pH 11, the sphalerite recovery was always low. Trahar et al. [9] found that the recovery drop took place at around pH 9. Our previous micro-flotation results demonstrated that the recovery drop occurred at pH 6. Laskowski and Liu et al. [14] showed that the recovery rate of sphalerite when activated by lead was high at the pH range from 5 to 12.

It is easy to see from above that although the topic of sphalerite activation has been surveyed for decades, the detailed mechanism under acidic and alkaline condition remains controversial or unknown. To the author’s knowledge, the main obstacle to unveil the nature of activation is the limitation of the experimental techniques. Most studies on sphalerite activation are performed using classical methods such as FTIR, Zeta potential and microflotation etc. Those methods can indeed provide some information on activation reaction, but they are indirect and *ex-situ* methods in nature, indicating some other factors can confound the analysis of results. We believe that more of understanding of sphalerite can only be achieved by introduction of new instruments into this field.

1.1.2 Collector adsorption

In froth flotation, collector is one kind of chemical agents used to increase the hydrophobicity of mineral. For sulfide flotation, xanthate salts are the most widely used collectors, which have following chemical structure.

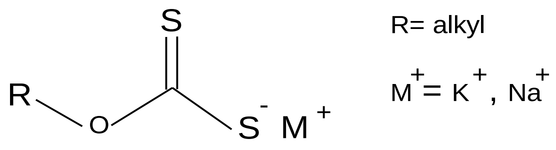

Figure 1.1 Chemical structure of xanthate salts

Some commercially important xanthate salts include:

- sodium ethyl xanthate (SEX), $CH_3CH_2OCS_2Na$,
- potassium ethyl xanthate (KEX), $CH_3CH_2OCS_2K$,
- sodium isopropyl xanthate (SIPX), $(CH_3)_2CHOCS_2K$
- sodium isobutyl xanthate (SIBX), $(CH_3)_2CHCH_2OCS_2K$
- potassium amyl xanthate (PAX), $CH_3(CH_2)_4OCS_2K$

Xanthate can react with some sulfides as shown in equation 1.3. As a result of the reaction, the CS_2 group binds to the sulfide surface sites and CH_3 group extends to solution phase, rendering the surface hydrophobicity. Generally, the xanthate salts with longer alkyl chain give a better flotation performance, which is probably due to the solubility difference between metal xanthate complexes as shown in Table 1.3, which indicates that the longer the alkyl chain of xanthate, the smaller the solubility of metal xanthate is.

Table 1.3 Solubility products (logK) of different metal xanthate complexes (the value of metal hydroxide solubility is given for comparison) [15]

Ligand	Zinc (II)	Lead (II)	Copper (I)	Silver (I)
ethyl xanthate	-8.31	-16.77	-19.28	-18.30
butyl xanthate	-10.43		-20.33	
hexyl xanthate	-12.90			-20.40
octyl xanthate	-15.82		-23.06	-21.86
hydroxide	-16.79	-16.09	-14.70	-7.39

1.1.3 Process water recycling

As mentioned above, the flotation process of minerals requires water to form a slurry mixture with ground ores. Although water consumption by mineral processing only constitutes a small portion of total water consumption by all industries in the world, several factors have led to increasing need of recycling “used” water (process water).

1) Water use in the location where mineral processing plant is located may represent a large proportion of the local water resource [16].

2) The effluents from mineral processing operations are detrimental to the environment as they contain salts with high concentration due to the dissolution of minerals or the addition of depressant and toxic chemicals coming from the addition of flotation agents. It is well known that some mineral processing plants are practicing zero water release or water release with total dissolved solids (TDS) below 1000ppm, which is required by environmental regulation.

3) The mineral processing plants may not always be close to the source of fresh water, so the transportation of fresh water to the production sites affects the operation cost of mineral industry.

Considering these factors, it is pertinent to recycle a great percentage of process water environmentally and economically. Different from fresh water, recycled process water contains many contaminants including Ca^{2+}, Mg^{2+}, Na^{+}, K^{+}, SO_4^{2-}, Cl^{-}, thiolsalts, metal ions, collectos, frothers and silicates. These contaminants affect the flotation performance by altering the chemistry of pulp water and interacting with ores or coating on valuable and gangue particles indiscriminately. In sulfide flotation plants, this problem is aggravated by the presence of a large amount of calcium and sulfate ions with high concentration due to dissolution and oxidation of ores and addition of activator or depressant (copper sulfate is added to activate sphalerite; zinc sulfate is added to depress sphalerite for the flotation of galena). The precipitate of calcium and sulfate ions, calcium sulfate dihydrate (gypsum), has higher solubility than calcium carbonate, which, to some extent, stabilizes the coexistence of both ions. It has also been suspected that gypsum can coat sulfide minerals and gangue particles indiscriminately, leading to reduced selectivity and recovery.

1.2 Objective and techniques

1.2.1 Objective

This research focuses on three parts:

1) Study the activation kinetics in order to understand the activation mechanism.

Sphalerite activation is an activator adsorption process in nature. Studying the kinetics of adsorption is crucial to understand the mechanism since the rate of adsorption gives information on the interaction between activator ions and sphalerite surface. Although the kinetics of zinc sulfide activation has been studied for decades, there are not enough quantitative measurements to conclude the activation mechanism. The major hindrance is limitation of experimental techniques. Most studies on sphalerite activation are performed using classical methods such as FTIR, zeta potential and microflotation etc., which are *ex-situ* methods. Some physical or chemical changes can occur during sample transferring or cleaning. Some other techniques are *in-situ* such as ion selective electrodes, but they are not sensitive enough to track the changes that occur within 1-2 minutes, during which the first stage of zinc sulfide activation with copper under acidic condition is completed [17]. In this study, a new technique, quartz crystal microbalance with dissipation (QCM-D), is employed to study the zinc sulfide activation kinetics. QCM-D has several advantages to investigate zinc sulfide activation. First, the mass change of zinc sulfide due to the adsorption of activator is continuously monitored over time, without the need for sample cleaning or transferring. Therefore, QCM-D is an *in-situ* technique. Second, QCM-D is a very sensitive tool. The maximum mass sensitivity of in liquid is about 0.5ng/cm^2 if measuring at a rate of one data point every five seconds. Finally, the surface area of different zinc sulfide QCM-D sensors (ZnS sensor) can be considered to be constant since the surface of ZnS sensor is very smooth with a roughness of 2 nm. It therefore provides a basis for comparison of experiments using different ZnS sensors.

2) The effect of calcium sulfate on sphalerite flotation

Calcium and sulfate are the most important dissolved inorganic ions in recycled water of sulfide flotation plants. At Red Dog mine, calcium and sulfate ions comprise of 90% of total dissolved solids in process water. They can adsorb onto different mineral surfaces to change the surface charge, as a result of which undesired surface interaction may occur. Apart from ion adsorption, they can precipitate from solution to form calcium sulfate dihydrate (Gypsum). The presence of large amount of gypsum can cause a lot of problems in flotation plants including surface coating on mineral surfaces indiscriminately, scaling, decreasing grade etc. In this study, a preliminary investigation of calcium adsorption on ZnS sensor with QCM-D, micro-flotation of sphalerite in presence of calcium ions and gypsum precipitation on sphalerite surface is conducted.

3) The selective precipitation of gypsum on functional surfaces

Considering the negative effect of calcium sulfate on sulfide flotation, it is imperative to remove it from process water. Studies at the Red Dog operation have shown that addition of gypsum as nucleation seeds decreases the concentrations of calcium and sulfate ions in treated water; however this effect could not be sustained. Fine particles of gypsum without surface treatment cannot act as nucleation seed in aqueous solution probably due to the aging of nucleation site. Based on our experience, we can employ surface functionalization technology to manufacture the wet gypsum seeds that will be effective at a wide range of temperatures for accelerating the nucleation and crystallization of gypsum. Generally speaking, our idea is to use gypsum or other mineral coated with certain chemicals to function as an effective nucleation seed to increase the gypsum precipitation rate in the process water, decreasing calcium sulfate concentration. In this study, a preliminary investigation of gypsum nucleation on different functional surfaces is performed to understand what functional group induces the maximum gypsum nucleation rate.

1.2.2 Quartz crystal microbalance with dissipation (QCM-D)

The development of quartz crystal microbalance (QCM) goes back to 1959 when G. Sauerbrey found that the resonance frequency shift of a quartz crystal was proportional to the mass change of itself [18]. Q-sense Company, founded in 1996 by a group of researchers at the Department of Applied physics, Chalmers University of Technology in Gothenburg, is a pioneer in the commercialization of QCM technique. The latest model of quartz crystal microbalance with dissipation, Q-sense E4, can monitor the real-time adsorption/desorption rate and structure change of adsorbed layer by measuring changes in resonance frequency (Δf) and energy dissipation (ΔD) of adsorbed film at 8 different harmonics simultaneously. A picture of E4 is shown in Figure 1.2.

Figure 1.2 Quartz crystal microbalance with Dissipation (QCM-D) (Q-sense, Gothenburg, Sweden)

The core part of a QCM is a thin quartz disc sandwiched between a pair of gold electrodes. Due to the piezoelectric properties of quartz, it is possible to excite the crystal to oscillate by applying an AC voltage across its electrodes as shown in Figure 1.3. When a mass is added to the crystal, its resonance frequency will decrease. If the adsorbed film is rigid and thin, the mass increase will be proportional to the frequency shift. A soft film dampens the crystal's oscillation. The dissipation factor (D) of the crystal's oscillation reveals the film's softness.

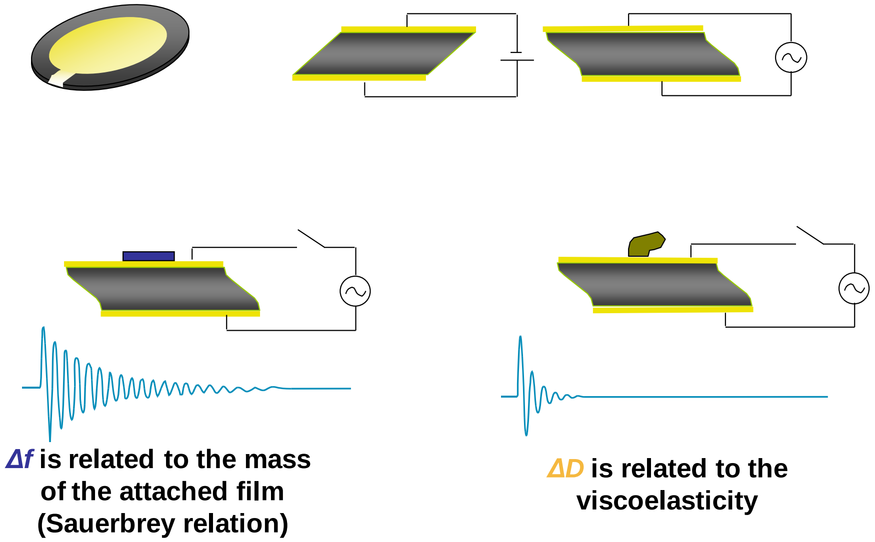

Figure 1.3 Schematic showing of the resonance of a QCM-D sensor

In this study, a zinc sulfide coated quartz crystal sensor (ZnS) was used. The real-time adsorption of activator on ZnS sensor was monitored by the QCM-D, the result of which can be converted to a plot of Δm versus t.

1.3 Literature review

1.3.1 Activation kinetics

Sphalerite (zinc sulfide) does not respond well to short chain thiol collectors due to the high solubility of zinc-xanthate in water, and therefore its flotation process requires the use of activator to enhance the adsorption of collectors onto sphalerite surface. Transition metal ions such as cupric, silver, lead and cadmium ions have been proved to be effective activators in sphalerite flotation [4].

Acidic pH

It is generally accepted that the overall activation reaction at acidic pH is an ion exchange process [4, 19]:

$$M_{aq}^{2+} + ZnS_{surface} \rightarrow Zn_{aq}^{2+} + MS_{surface} \qquad 1.5$$

The evidence advanced for this proposed reaction rests on two key points. Firstly, the ratio of adsorbed M_{aq}^{2+} and released Zn_{aq}^{2+} remains unity for divalent metal ions [6] and two for monovalent ions [20]. Secondly, the exchange reaction has been shown to be thermodynamically favorable [21].

Previous studies have shown conflicting results regarding the activation kinetics with silver, copper and lead as activators. Activation kinetics models including one-stage, two-stage or three-stage have been reported [10, 17, 20, 22-24]. Although most researchers agree that the activation is a two-stage reaction, they vigorously disagree in certain extent as to which kinetics law applies to each stage. These disagreements are partly due to the variation among the samples used in previous studies, which have different specific surface areas and impurity contents [6]. The results between various studies were further complicated by the different techniques used. The progress and remaining challenging issues in understanding the activation kinetics of sphalerite are summarized as follows.

Gaudin et al. [22] investigated the adsorption of silver ions on sphalerite by feeding the blending solution of radioactive and ordinary silver nitrate to a column filled with sphalerite particles and then monitoring the silver content of the effluent solution. It was suggested that two reactions were involved in the silver adsorption process, based on the observation that all the silver ions were initially removed by sphalerite in the feeding solution until a “break-through” time, after which the removal of silver continued but at a decreased rate. Without mentioning the mechanism for the first rapid reaction, Gaudin et al. concluded that diffusional rearrangement within the mineral solid occurred all the time within the second reaction, although the actual mechanism was not clear. This diffusional rearrangement provided new capacity for silver adsorption on the surface. No significant difference was observed from the adsorption curve in the pH range (5.4 to 6.4) investigated. A subsequent study by Gaudin et al. [20] using Ag^{110} tracer found that the Ag^+ formed a silver sulfide layer on sphalerite through an exchange mechanism according to equation 1.6.

$$ZnS_{(s)} + 2Ag^{+} \rightarrow Ag_2S_{(s)} + Zn^{2+} \qquad 1.6$$

The exchange was proportional to the logarithm of the time and proceeded until either of the reactants was consumed.

Ralston and Healy [17, 23] studied the activation kinetics of synthetic zinc sulfide with Cu(II), Pb(II) and Cd(II) at pH ranging from 4 to 9 using ion selective electrodes. Three reaction stages were distinguished for adsorption of Cu(II) , and two stages for Pb(II) and Cd(II). For Cu(II), the adsorption followed direct logarithmic kinetics in the first two stages. One layer of copper was first adsorbed within 1.5 min, and the uptake of Cu(II) was independent of initial ion concentration and pH (4–6.5). In the following 15 min considered as the second stage, less than half of monolayer was adsorbed at a smaller rate than the first one. The rate equation for Cu(II) adsorption between 15min to 2 hours was not well-defined in the study by Ralston and Healy. For Cadmium adsorption, it was reported that both stages followed direct logarithmic kinetics, which lasted for 1 min. and 2 hours respectively. Lead showed logarithmic adsorption kinetics for the first 1.5 min, and the reaction continued in an undefined way. The total amount of adsorbed Cd(II) and Pb(II) and their adsorption rates in all stages were significantly lower than that of Cu(II).

Harris and Richter [25] investigated the adsorption of Cu(II) on synthetic zinc sulfide and natural sphalerite at pH~5 using a Ag-plate electrode. The activation reactions on both types of samples were shown to have two stages following logarithmic kinetics: rapid adsorption of up to 2 monolayers in the first minute followed by adsorption of 3-4 monolayers until the end of the test (~10 min). No rate equation was identified for either stage.

The two-stage reaction in the activation of sphalerite by copper at acidic pH was also reported by Jain and Fuerstenau [8]. They investigated the effects of agitation, solid-to-liquid ratio and initial copper concentration on the copper uptake by monitoring the changes of copper ion concentration with an ion selective electrode. The results indicated that the adsorption of copper in the first stage, lasting up to 15 min, followed a direct logarithmic law. The second stage followed parabolic kinetics as long as the reaction was followed up to 64 hours, and the slopes of the uptake vs. time$^{1/2}$ curves for various initial copper concentrations were very close. One-stage reaction kinetics was suggested by Sui et al. [10] who showed that the adsorption kinetics of copper and lead on sphalerite at pH 3 during a 60 min experiment period could be fitted by a logarithmic function.

Alkaline pH

It is well documented that sphalerite can be activated by copper in neutral and alkaline media, although the flotation of activated sphalerite by copper is depressed in pH range of 6 to 9, depending on the amount of copper added [26]. Fuerstenau and Metzger [27] reported that, based on solution analysis, the adsorption of Pb(II) was quite slow and could be described by a power law. Ralston et al. [23] followed the copper and lead activation reaction for up to two hours under neutral to weakly alkaline condition using ion-selective electrodes. For both copper and lead, the metal ion uptake was enhanced, compared with activation at acidic pH values. At least two steps were observed in the activation reaction when it came to fit the real-time metal ion uptake curves with different mathematical equations. For the first activation step, the copper and lead ions uptakes followed a logarithmic equation. It was found that 1-1.5 layers of copper and about 0.3 layer of lead on sphalerite surface were formed in the first step that lasted for 5 minutes. In second step, the copper uptake still obeyed a logarithmic law but with a lower rate, while there was no equation that could describe the lead uptake. Sui et al. [10] showed that, based on metal ion content analysis using atomic analysis spectroscopy, the copper adsorption rate at pH 6 and 9.2 was characterized by two stages: a rapid stage that occurred over first minute and followed logarithmic equation and a slow stage that was fitted with a parabolic equation. The exchange ratio of Cu to Zn was close to one at three pH values(3, 6 and 9.2), which was a characteristic of ion exchange reaction. Three stages were found in the lead uptake curves at pH 6 and 9.2, and all of them followed logarithmic equation. The adsorption rate of lead increased as pH increased from 3 to 9. Different from copper activation, the exchange ratio of Pb to Zn was much higer than one. A recent XPS study by Kartio et al. [24] on sphalerite activation by copper found that the copper uptake at pH 9.2 showed a logarithmic time dependence during the first hour, which was not consistent with the results by Sui et al.

It should be noted that the amount of metal ions adsorbed on sphalerite surfaces was calculated by taking samples at different time intervals during the activation process and then analyzing the concentrations of metal ions through atomic adsorption spectroscopy in the study by Sui et al. Adsorption of metal ions determined at high pH by this method was complicated by the difficulty in distinguishing the hydroxide precipitates in the bulk solution from those adsorbed on or coagulated with sphalerite.

In summary, the activation of sphalerite has been studied extensively over half a century. However, the actual activation and flotation mechanisms as well as associated surface reaction products still remain controversial.

1.3.2 Effect of calcium sulfate on sphalerite flotation

The quality of process water can significantly affect the flotation performance in a number of ways at sulfides processing plants. Some of effects have been studied and easily understood (e.g. pH) but more are hardly measurable and controlled. The following list indicates important parameters and components of process water quality that result in low selectivity and recovery.

1) Although it is well reported that pH plays a crucial role in sulfide flotation, the variability of pH from different streams comprising the process water makes the routine pH survey unrepresentative of the nature of real condition.

2) Precipitation of colloidal particles from various species in the process water is unrecognizable in chemical assays. These colloidal species may remain well dispersed in the solution or attached to mineral surfaces as hydrophilic layers leading to reduced recovery. They can be categorized as metal hydroxides, calcium/magnesium carbonate and sulfate, aluminosilicates and metal-organic complexes.

3) Adsorption of cations and anions alters the surface charge of some mineral particles in the flotation circuit, which may result in undesired aggregation and hetero-coagulation.

Among all components in recycled process water, calcium and sulfate ions are the most frequently experienced species in sulfide flotation plants. Not only can calcium ions interact with mineral particles, collector and other reagents, the precipitation of calcium and sulfate ion, calcium sulfate dihydrate (gypsum), also can coat sulfide and other heavy mineral sands surfaces. In one processing plant, up to 70% of the sulfide mineral surfaces was obscured by deposited calcium sulfate layers.

1.3.2.1 Origin of calcium and sulfate ions

The origins of calcium and sulfate ions mainly are the dissolution of ores and addition of reagents for various purposes. Several sulfide processing plant practices will be listed in following part to explain the source of calcium and sulfate species.

Red Dog mine

The Red Dog mine, located in Alaska, is the world's largest producer of zinc, accounting for 10% of world's zinc production. The main deposit in Red Dog is zinc-lead sulfide ore at a grade of 17% and 5% respectively. The Red Dog mine annually discharges about 1.5 billion wastewater, despite water reclamation is implemented. A simplified flow chart of the plant water system is shown in Figure 1.4.

Calcium concentration in the plant pulp solutions is 600-720 ppm. It is comparable with the Ca concentration in the reclaimed water (720 ppm). Considering that the Ca concentration in the pulp solutions produced during ore dissolution test in De-ionised water was 120 ppm and the Ca concentration in the pulp solutions produced during laboratory flotation test in De-ionised water is only 75 ppm, the relatively high concentration of calcium in process water is mainly from reclaimed water. As shown in Figure 1.4, the reclaimed water is recycled by pumping treated tailing water back to Mill, and the origin of calcium in reclaimed water is the addition of lime to precipitate heavy metal ions.

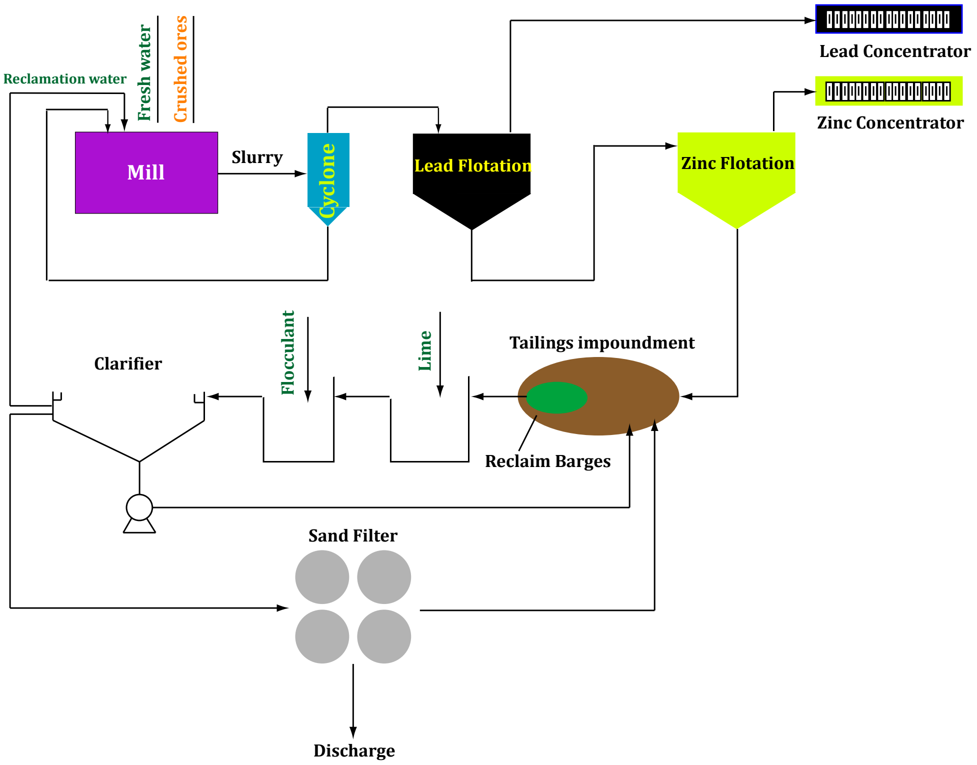

Figure 1.4 Process flow chart of Red Dog mine

Sulfate concentration in the plant pulp solutions is 2400-2800 ppm. It is comparable with the sulfate concentration in the reclaimed water (2700 ppm). Considering that the sulfate concentration in the pulp solutions produced during ore dissolution test in De-ionised water is around 245 ppm and the sulfate concentration in the pulp solutions produced during laboratory flotation test in De-ionised water is about 400 ppm, this indicates that the sulfate concentration in the plant pulp solutions originates mainly from reclaimed water additions in the plant. Ore dissolution and reagent additions in the plant ($ZnSO_4$) also contribute to some extent to the high sulfate levels in the flotation circuits.

Hilton mine

The Hilton mine is situated 20km north of Mt. Isa in north-west Queensland, Australia. The concentrator produces separate products of lead, zinc and a combined lead/zinc concentrate. In the Hilton ore, lead and zinc occur as galena and sphalerite, as for Mt. Isa ore. Pyrrhotite is the predominant iron sulfide mineral in the hanging wall and Pyrite is the predominant iron sulfide mineral in the footwall ore. Dolomite is a significant component of non-sulfide gangue ore.

The calcium concentration plant pulp is about 600ppm. Generally, the high level of calcium in the circuit water is derived from the following two sources:

1) Dissolution of the domolitic component of the ore.

$$Fe_7S_8 + 12O_2 + 12H_2O + 12CaCO_3 \rightarrow FeS_2 + 6Fe(OH)_2 + 6Ca(HCO_3)_2 + 6CaSO_4 \quad 1.7$$

2) Addition of line for pH control during sphalerite flotation

The flotation of sphalerite is carried out under alkaline condition, hence lime is added into the circuit to adjust pH. The contained calcium in tailing goes back to circuit water via recycling thickener overflow. The concentration of sulfate ion in flotation pulp is about 2800ppm, and the source of sulfate ion is mainly the dissolution of sulfide ores and the addition of $ZnSO_4$ as depressant during galena flotation.

Kristineberg mine

Kristineberg mine, located in northern Sweden, was opened in 1940 during World War II. Annual output of this mine comprises 35kt copper concentrate, 65kt zinc concentration, 5kt lead concentrate and 100kt pyrite concentrate. The calcium concentration in the reuse water is about 500ppm, and the source of calcium is the addition of lime into rod mill to adjust pH to 12. Recycling of process water does not significantly change the calcium concentration. Sulfate concentration in the flotation circuit is about 500~ 1400ppm and it is mainly from reuse water.

1. 3.2.2 Calcium adsorption

Moignard et al. [28] studied the calcium adsorption on synthetic ZnS from pH 6 to pH 11 using an atomic adsorption spectrophotometer. The results indicated that adsorption density of calcium commenced between pH 7 to pH 8 and continued to increase until pH 11, at which 45% calcium was adsorbed. Electrokinetic measurement showed that the zeta potential of ZnS became less negative below pH 7 in presence of 20 ppm calcium ions, and a charge reversal was observed between pH 7.5 to pH 8.0, after which the zeta potential became less negative again. Considering the significant adsorption of calcium ions on ZnS under alkaline condition, it is anticipated that Ca^{2+} has a depressing effect on sphalerite flotation at high pH similar to its effect on pyrite.

Sui et al. [29] investigated the interaction of sphalerite with Ca and precipitates of calcium sulfate. In presence of 500ppm calcium ions, the zeta potential of sphalerite increased significantly at the whole range of pH. Three ieps were observed as compared to one iep of pure sphalerite. The increase in zeta potential was attributed to adsorption of calcium ions. In presence of 1200ppm calcium ions and 4800ppm sulfate ions, the zeta potential of spahlerite was quite similar to that in presence of calcium ions alone. This observation implied that sulfate ions did not contribute to the zeta potential of sphalerite in presence of both calcium and sulfate ions. The same conclusion is drawn by Ikumapayi [30] who found that zeta potentials of sphalerite did not change with sulfate concentration at pH 11.5, but increased with calcium concentration at the same pH. In presence of calcium ion alone, the zeta potential became less negative as compared to without calcium ions from pH 3 to pH 12. At pH 11.5, Hallimond flotation of unactivated sphalerite was slightly depressed with the addition of calcium ions up to 200ppm, above which the flotation recoveries were either increased marginally or averagely constant.

A similar ion adsorption on mineral surface is observed by Peng et al. [31] who conducted flotation tests to study recovery of pentlandite and serpentine from Mt. Keith mine in bore water containing 20,000 ppm Na^+, 400 ppm Ca^{2+}, 5100 ppm Mg^{2+}, 32,000 ppm Cl^- and 23,000 ppm SO_4^{2-}. It was found that the flotation of pentlandite was depressed due to the coating of serpentine on pentlandite particles since they carried opposite surface charge at neutral and alkaline pH in de-ionised water. In bore water, Ni recovery was increased significantly while MgO recovery was decreased implying the disappearance of coating. This was supported by the zeta potential measurements that showed zeta potential of both penlandite and serpentine were close to zero in a solution with only 2% bore water.

Liu et al. [32] performed micro-flotation tests to study the effect calcium and sulfate ions on recoveries of sphalerite, galena, and pyrite. At pH<10, the recovery of sphalerite was not affected by calcium ions up to 3000ppm while the recoveries of galena and pyrite decreased as calcium concentration increased. Sulfate ions did not impact the recoveries of sphalerite and galena, but deteriorated the recovery of pyrite. UV-Vis measurement showed that the adsorption peak of xanthate at 190-400nm^{-1} did not change in the presence of calcium ions.

1.3.2.3 Gypsum precipitation

When the concentrations of calcium and sulfate ions are high enough to exceed the solubility of calcium sulfate dihydrate (gypsum), gypsum will crystallize on surface of mineral or in the bulk solution.

$$Ca^{2+} + SO_4^{2-} + 2H_2O \leftrightarrow CaSO_2 \bullet 2H_2O_{(s)} \qquad 1.8$$

The crystallization of gypsum has two steps: nucleation and crystal growth. Nucleation can be defined as the formation of nuclei that can develop to crystal as more molecules grow on it in the early stage. The prerequisite of nucleation is the achievement of supersaturated solution, where nucleus has opportunity to grow to big enough size. In most cases, the nucleus may only compose of dozens of molecules and it also may evolve in very short time, so it is difficult to trace the development of nucleus with current experimental techniques. Classical nucleation theory (CNT) is widely used to describe the nucleation theoretically due to its analytic simplicity. Initially, CNT is derived from condensation from vapor to liquid, which is employed to explain the nucleation from solution later. CNT can be summarized as the competing between negative Gibbs energy produced by formation of new solid phase from solution and the positive energy required to create new interfacial surface between new solid phase and solution phase.

After the formation of nuclei, molecules in the solution can diffuse to the surface of formed nuclei, and they only can fill in the position of “kinks” as shown in Figure 1.5 [33]. The process of molecules building up on formed nuclei is called crystal growth.

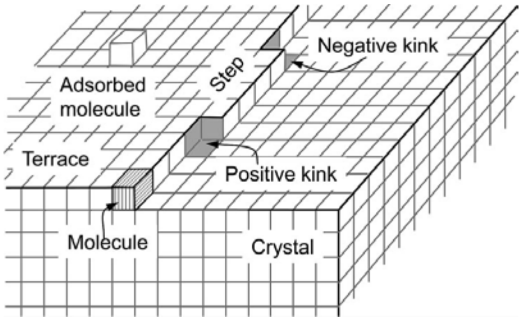

Figure 1.5 Schematic showing of kinks on a crystal surface

So the crystallization rate depends on three factors: diffusivity of molecules, number of kink sites on every nucleus as well as the number of nucleus in the bulk solution.

Generally, there are two conventional direct methods to measure the growth rate. The first one is to measure the conductivity of the solution and the second one is to measure the turbidity. Another indirect method to describe the growth rate is induction time, which is defined as the time between the achievement of saturated solution and appearance of nucleus. Owing to this arbitrary definition, different instrument and people will get different results.

1.4 Outline of this thesis

This thesis consists of six chapters**:**

Chapter 1: This chapter provides the research background of the thesis. The sphalerite flotation process and process water recycling are briefly introduced. Previous work on zinc sulfide activation kinetics and the effect of calcium sulfate on sphalerite flotation are reviewed.

Chapter 2: In this chapter, the surface of zinc sulfide coated quartz crystal sensor (ZnS sensor) is characterized. After confirming ZnS sensor has the similar surface property to sphalerite, the kinetics of zinc sulfide activation with silver at acidic pH is investigated with quartz crystal microbalance with dissipation (QCM-D). The fitting of silver uptake with kinetics models is discussed.

Chapter 3: With demonstrated capability of QCM-D, zinc sulfide activation with copper and lead under neutral and alkaline condition is investigated in this chapter. The adsorption rate of copper and lead hydrolysis species is fitted with three kinetics models.

Chapter 4: This chapter focuses on the impact of calcium sulfate in sphalerite flotation. The effect of calcium is studied with QCM-D and micro-flotation. Surface energy calculation and SEM characterization are performed to understand the interaction between calcium sulfate dihydrate and sphalerite.

Chapter 5: In this chapter, the results of surface force measurement between two mica surfaces in the presence of calcium sulfate solution with various concentrations are presented, and the nature of the interaction is discussed. Three methods are used to deposit gypsum on mica surface, and the morphology of gypsum is characterized with atomic force microscope (AFM) and scanning electron microscope (SEM).

Chapter 6: The chapter presents the preliminary results of selective gypsum precipitation on functional surfaces. This work will shed light on the development of future techniques of removing gypsum from process water.

Chapter 7: The overall conclusions and future work are outlined in this chapter.

1.5 References

[1] A. Tolcin, Mineral Commodity Summaries, (2011).
[2] N. Finkelstein, S. Allison, Fuerstenau, MC, Editor, (1976) 414-457.
[3] J. Wie, D. Fuerstenau, International Journal of Mineral Processing, 1 (1974) 17-32.
[4] A.M. Gaudin, Flotation, McGraw-Hill, 1957.
[5] D.W. Oxtoby, H.P. Gillis, A. Campion, Principles of modern chemistry, Brooks/Cole Pub Co, 2007.

[6] N. Finkelstein, International Journal of Mineral Processing, 52 (1997) 81-120.

[7] A. Chandra, A. Gerson, Advances in colloid and interface science, 145 (2009) 97-110.

[8] S. Jain, D. Fuerstenau, Flotation of Sulphide Minerals, (1984) 159-174.

[9] W. Trahar, G. Senior, G. Heyes, M. Creed, International Journal of Mineral Processing, 49 (1997) 121-148.

[10] C. Sui, D. Lee, A. Casuge, J. Finch, Minerals and Metallurgical Processing(USA), 16 (1999) 53-61.

[11] C.A. Prestidge, W.M. Skinner, J. Ralston, R.S.C. Smart, Applied surface science, 108 (1997) 333-344.

[12] R. Pattrick, J. Charnock, K. England, J. Mosselmans, K. Wright, Minerals Engineering, 11 (1998) 1025-1033.

[13] F. Rashchi, C. Sui, J.A. Finch, International Journal of Mineral Processing, 67 (2002) 43-58.

[14] J. Laskowski, Q. Liu, Y. Zhan, Minerals Engineering, 10 (1997) 787-802.

[15] S.R. Rao, J. Leja, Surface Chemistry of Froth Flotation: Reagents and mechanisms, Plenum Pub Corp, 2004.

[16] S. Rao, J. Finch, Minerals Engineering, 2 (1989) 65-85.

[17] J. Ralston, T.W. Healy, International Journal of Mineral Processing, 7 (1980) 175-201.

[18] Z. Sauerbrey, Full Text via CrossRef, 206.

[19] N. Finkelstein, S. Allison, M. Fuerstenau, AIME. New York, l976. pp. 4l4-457.

[20] A. Gaudin, D. Fuerstenau, M. Turkanis, Trans. Am. Inst. Mining Met. Engrs, 203 65-69.

[21] R. King, South African Institute of Mining and Metallurgy, Kelvin House, 2 Holland St, Johannesburg, South Africa, 1982. 268, (1982).

[22] A. Gaudin, H. Sfledden, M. Corriveau, Mining Engineering, (1951).

[23] J. Ralston, T.W. Healy, International journal of mineral processing, 7 (1980) 203-217.

[24] I. Kartio, C. Basilio, R.H. Yoon, Langmuir, 14 (1998) 5274-5278.

[25] K.S.E. Forssberg, Stockholm, Sweden, June 1984, (1984) 1985.

[26] J. Steininger, Trans. AIME, 241 (1968) 34.

[27] D. Fuerstenau, P. Metzger, Trans. AIME, 217 (1960) 119.

[28] M. Moignard, R. James, T. Healy, Australian Journal of Chemistry, 30 (1977) 733-740.

[29] C. Sui, F. Rashchi, Z. Xu, J. Kim, J. Nesset, J. Finch, Colloids and Surfaces A: Physicochemical and Engineering Aspects, 137 (1998) 69-77.

[30] F.K. Ikumapayi.

[31] Y. Peng, D. Seaman, Minerals Engineering, (2011).

[32] S. LIU, C. SUN, X. CHEN, Nonferrous Metals(Mineral Processing Section), 2 (2007).

[33] J.W. Mullin, Crystallization, Butterworth-Heinemann, 2001.

Chapter 2 *In-situ* kinetic study of zinc sulfide activation using a quartz crystal microbalance with dissipation (QCM-D)*

2.1 Introduction

Flotation is a critical mineral processing step for selective separation of minerals from gangue, which generally relies on the surface interactions (mainly hydrophobic interactions) between air bubbles and mineral surfaces [1]. The collectors and activators have been widely used in sulphide flotation to increase hydrophobicity of target minerals. In general, sphalerite (zinc sulfide) does not respond well to short chain thiol collectors due to the high solubility of zinc-xanthate in water and therefore its flotation process requires the use of activators to enhance the adsorption of collectors onto sphalerite surface. Transition metal ions such as cupric, silver, lead and cadmium ions have been proved to be effective activators in sphalerite flotation [2].

It is generally accepted that the overall activation reaction at acidic pH is an ion exchange process [2, 3]:

$$M_{aq}^{2+} + ZnS_{surface} \leftrightarrow Zn_{aq}^{2+} + MS_{surface} \qquad 2.1$$

The evidence advanced for this proposed reaction rests on two key points. Firstly, the ratio of adsorbed M_{aq}^{2+} and released Zn_{aq}^{2+} remains unity for divalent metal ions [4] and two for monovalent ions [5]. Secondly, the exchange reaction has been shown to be thermodynamically favourable [6].

Previous studies have shown conflicting results regarding the activation kinetics with silver, copper and lead as activators. Activation kinetics models including one-stage, two-stage or three-stage have been reported [5, 7-11]. Although most researchers agree with that the activation is a two-stage reaction, they vigorously disagree in certain extent as to which kinetic law applies to each

---

*Published paper: F. Teng, Q. Liu, H. Zeng, Journal of Colloid and Interface Science, 2011 (in press).

stage. These disagreements are partly due to the variation among the samples used in previous studies, which have different specific surface areas and impurity contents [4]. The results between various studies were further complicated by the different techniques used. The progress and remaining challenging issues in understanding the activation kinetics of sphalerite is summarized as follows.

Gaudin et al. [8] investigated the adsorption of silver ions on sphalerite by feeding the blending solution of radioactive and ordinary silver nitrate to a column filled with sphalerite particles and then monitoring the silver content of the effluent solution. It was suggested that two reactions were involved in the silver adsorption process, based on the observation that all the silver ions were initially removed by sphalerite in the feeding solution until a “break-through” time, after which the removal of silver continued but at a decreased rate. Without mentioning the mechanism for the first rapid reaction, Gaudin et al. concluded that diffusional rearrangement within the mineral solid occurred all the time within the second reaction, although the actual mechanism was not clear. This diffusional rearrangement provided new capacity for silver adsorption on the surface. No significant difference was observed from the adsorption curve in the pH range (5.4 to 6.4) investigated. A subsequent study by Gaudin et al. [5] using Ag^{110} tracer found that the Ag^+ formed a silver sulfide layer on sphalerite through an exchange mechanism according to equation 2.2.

$$ZnS_{(s)} + 2Ag^{+} \leftrightarrow Ag_{2}S_{(s)} + Zn^{2+} \qquad 2.2$$

The exchange was proportional to the logarithm of the time and proceeded until either of the reactants was consumed.

Ralston and Healy [9, 10] studied the activation kinetics of synthetic zinc sulfide with Cu(II), Pb(II) and Cd(II) at pH ranging from 4 to 9 using ion selective electrodes. Three reaction stages were distinguished for adsorption of Cu(II) , and two stages for Pb(II) and Cd(II). For Cu(II), the adsorption followed direct logarithmic kinetics in the first two stages. One layer of copper was first adsorbed within 1.5 min, and the uptake of Cu(II) was independent of initial ion concentration and pH (4–6.5). In the following 15 min. considered as the second stage, less than half of monolayer was adsorbed at a lower rate than the first one.

The rate equation for Cu(II) adsorption between 15 min. to 2 hours was not well-defined in the study by Ralston and Healy. For Cadmium adsorption, it was reported that both stages followed direct logarithmic kinetics, which lasted for 1 min. and 2 hours respectively. Lead showed logarithmic adsorption kinetics for the first 1.5 min, and the reaction continued in an undefined way. The total amount of adsorbed Cd(II) and Pb(II) and their adsorption rates in all stages were significantly lower than that of Cu(II).

The two-stage activation kinetic was reported by Harris and Richter [12] and Jain and Fuerstenau [13] who investigated the adsorption of Cu(II) on synthetic zinc sulfide and natural sphalerite under acidic condition using selective ion electrodes. The results indicated that the first and second stage followed logarithmic and parabolic kinetics, respectively.

One-stage reaction kinetics was suggested by Sui et al. [7] who showed that the adsorption kinetics of copper and lead on sphalerite at pH 3 during a 60 min experiment period could be fitted by a logarithmic function. However, when the pH increased to 6.0 and 9.2, the copper adsorption process was characterized by two stages: a rapid stage that occurred over the first minute that followed a logarithmic relation and a slow stage (1-60 min) that could be fitted by a parabolic function. A recent XPS study by Kartio et al. [11] on sphalerite activation by copper found that the copper uptake at pH 9.2 showed a logarithmic time dependence during the first hour, which was not consistent with the results by Sui et al.

In summary, the activation of sphalerite has been studied extensively over half a century. However, the actual activation and flotation mechanisms and associated surface reaction products still remain controversial, although there is general agreement on the overall process. The controversial results are not only due to the complex nature of the activation process and diversity of the mineral samples, but also due to the limitation of the techniques employed in the previous studies. The techniques applied were either *ex-situ* methods (atomic adsorption spectroscopy, radioactive tracer, XPS, FTIR) or not sensitive enough to detect the changes taking place within a short period (one minute) (various ion selective electrodes) since the reaction mostly takes place within the first 10-15 mintues. The objective of the present work is to apply a quartz crystal microbalance with dissipation (QCM-D) to an *in-situ* investigation of sphalerite activation kinetics with silver as the activator. QCM-D measures the mass change per unit area with a sensitivity of ~0.1 ng/cm^2 by monitoring the frequency change of a quartz crystal sensor with various coatings on the top (zinc sulfide coating in this study). With the capability of measuring the dissipation and frequency shift simultaneously as a function of time [14], QCM-D can be applied to determine the state of molecular layers bound to the sensor surfaces, i.e., mass, thickness, viscoelastic or other structural properties in real-time with extremely high sensitivity. To our best knowledge, the present study is the first of its kind to apply the QCM-D technique to investigate sphalerite activation, which indroduces a new *in-situ* approach to investigate the surface adsorption and activiation in many mineral proccesses and surface modifications.

2.2 Materials and Experimental Methods

2.2.1 Materials

Silver nitrate (BDH chemicals, Canada) was used as received without further purification. A high purity sample of sphalerite was acquired from Ward's Natural Science. The sample was crushed, hand-sorted and dry screened to collect the 38 to 75 μm size fraction for X-ray diffraction measurement. Commercial potassium amyl xanthate (Prospec Chemicals Ltd, Canada) was purified by following method: 100 g xanthate was added to 1000 ml of warm acetone (40°C) on a water bath and stirred for a few minutes. The solution was then filtered through a hot water funnel and discarded [15]. Nitric acid (Fisher Scientific Company, Canada, 99%) and sodium hydroxide (Fisher Scientific Company, Canada, 99%) were used to adjust solution pH. All solutions used in experiments were prepared using Milli-Q water (Millipore deionized, >18.2 MΩcm, 0.22-μm-filtered) and then filtered by 0.2 μm filter after complete mixing. All tests using QCM-D were conducted under room temperature of 22 °C.

2.2.2 Quartz Crystal Microbalance with Dissipation (QCM-D)

The reaction rate of activation was investigated using a QCM-D (Q-sense E4, Q-sense AB, Gothenburg, Sweden) with the capacity of measuring changes in resonance frequency (Δf) and energy dissipation (ΔD) of QCM-D sensors at 7 different harmonics simultaneously. The data were collected every 0.5 second by the Q-sense Qsoft 401. The AT-cut quartz crystal with zinc sulfide coating on the top surface (shown in Figure 1) was purchased from Q-sense.

A quartz crystal sensor is a thin piezoelectric plate with gold electrodes on each side. When a mass is added to the sensor, its resonance frequency will decrease due to the piezoelectric effect of quartz. After the experiment, data modeling and analysis were carried out with Q-sense Qtools 3.0, in which Sauerbrey model and Viscoelastic model could be chosen to convert frequency change to mass change. When the adsorbed film on the surface of sensor is relatively uniform, rigid and thin compared to the sensor itself, and the dissipation change ΔD is smaller than 10^{-6} for a 10Hz frequency change [16], the Sauerbrey model is used in the form of so-called Sauerbrey equation:

$$\Delta m = \mathrm{C}\frac{\Delta f}{n} \qquad 2.3$$

Where Δm and Δf is mass and frequency change respectively, and n is the resonance number of sensor (n=1, 3, 5, 7, 9, 11, 13). C is a constant depending on the physical property of sensor (C=17.7 ng/cm^2 in our system). For the sake of simplicity, only three harmonics (n = 3, 5 and 7) are shown in the results. In this study, the fifth harmonic was used to determine the frequency and dissipation shifts and to calculate the corresponding mass change.

Prior to each experiment, the quartz crystal sensor with zinc sulfide coating (referred to as ZnS sensor hereafter) was cleaned as follows: soaked in hydrochloride acid solution (0.01 M) and sonicated for 5 minutes, followed by thorough rinsing with Milli-Q water. For a typical QCM-D experiment, a cleaned ZnS sensor was inserted into flow module with the ZnS surface facing testing solution. The flow module was then mounted on the Q-sense E4 chamber platform. Milli-Q water at pH 5 was pumped into the flow module by an IPC-N peristaltic pump (Ismatec, Switzerland) at a flow rate of 0.15 ml/min. For each measurement, a stable baseline (with frequency variation less than 1 Hz for at least 10 minutes) was first achieved using Milli-Q water and then followed by injection of testing solution, which was silver nitrate solution at pH 5 in this study. Subsequent xanthate adsorption test was performed by injecting potassium amyl xanthate solution of 5×10^{-5} M at pH 5 into the flow module at 0.15 ml/min. After QCM-D measurement, the ZnS sensor was taken out, rinsed with Milli-Q water, and then fully dried with nitrogen for surface characterization.

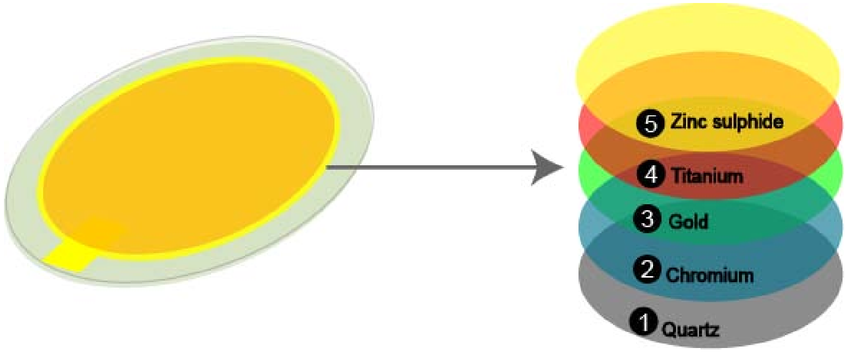

Figure 2.1 Schematic showing of the layer structure of ZnS QCM-D sensor

2.2.3 X-ray diffraction (XRD)

Grazing incidence X-ray diffraction (GIXRD) was used for the crystalline characterization of ZnS sensor using a Rigaku ULTIMA IV system with Cu K_α radiation (λ=1.54Å). X -ray radiation was operated at 40 kV and 44 mA. The intensity data were collected in the 2θ range of 10-110° with a scanning speed of 2°/min. GIXRD uses a small incident angle (2°) for the incoming X-rays so that the diffraction is surface sensitive, minimizing the contribution from the substrate.

2.2.4 Atomic Force Microscope (AFM) Imaging

Morphology of sample surfaces was characterized with an atomic force microscope (AFM) (Agilent 5500, Agilent Technologies, Inc., Chandler, AZ, USA), operated under AAC mode in air using silicon nitride cantilevers (RTESP, Veeco, Santa Barbara, CA) with a nominal resonance frequency of 200-300 kHz.

During AFM imaging, the amplitude set point (A_s) was set at 95-98% of the free amplitude (A_0). At this A_s/A_0 ratio, the force applied by the cantilever tip on the sample surfaces was sufficiently low to avoid damaging the sample surfaces. Multiple locations were imaged for all the samples at room temperatures (21.0 $\pm$0.5 °C), and a representative image was presented.

2.2.5 X-ray photoelectron spectroscopy (XPS)

An AXIS 165 spectrometer (Kratos Analytical) was used to determine the chemical composition of untreated and treated ZnS sensors. The base pressure in the analytical chamber was lower than 5×10^{-8} Pa, and the working pressure was better than 3×10^{-7} Pa. A monochromatic Al Kα (hν 1486.6 eV) source of 210 W was used. The analyzer was operated infixed analyzer transmission (FAT) mode. The high resolution XPS spectra were obtained at a pass-energy of 20 eV with a step of 0.1 eV. The sampling spot size was 700 × 400 µm. The binding energy 284.6 eV of C1s in hydrocarbon was used as reference.

2.2.6 Contact angle measurement

Static contact angles of water on sample surfaces were measured using a drop shape analyzer (DSA100, Krüss, Germany) equipped with an optical microscope and illumination system. The sessile drop method with drop volumes of 10-20µL was employed at room temperature (21.0$\pm$0.5°C). Contact angle was measured within 5 sec after the water droplet was dropped onto ZnS sensor surface. The shape of the sessile drop was recorded and fitted by the computer to calculate the contact angle.

2.3 Results and discussion

2.3.1 ZnS sensor chracterization

2.3.1.1 X-ray diffaction

By measuring the crystallographic structure using GIXRD, the X-ray diffraction (XRD) patterns of a ZnS sensor and sphalerite sample were compared.

Although not all peaks of ZnS sensor matching that of natural sphalerite, the three characteristic peaks corresponding to plane (111), (220) and (311) of sphalerite are at 2θ° of 28.5°, 47.3° and 55.9°, respectively (JCPDS card, No. 00-005-0566 sphalerite) [17]. The XRD analysis showed that the ZnS coating had the polycrystalline cubic structure with a=5.389 Å , which is close to the lattice constants of sphalerite in this work (a=5.40 Å) and ZnS presented in literature (a=5.34 Å [18] and a=5.41 Å [19]).

2.3.1.2 AFM imaging

The topographical image of cleaned ZnS sensor surface was obtained using AFM. The root mean square (RMS) roughness is ~2nm. The smooth surface provides a consistent surface area for repetitive tests using different ZnS sensors.

2.3.1.3 X-ray photoelectron spectroscopy (XPS)

Binding energy

The XPS spectra were obtained from freshly cleaned ZnS sensor. In order to analyse the possible components in the spectrum, a deconvolution of the spectrum into individual components was carried out. Each XPS spectrum was fitted by symmetric Gaussian-Lorentzian functions. Argon sputtering was followed by XPS measurement on the surface to investigate the state of elements at different depths and the atomic concentration distribution across the zinc sulfide layer. Figure 2.2 shows the spectra of element C 1S, Zn 2P, S 2P and O 1S on the cleaned ZnS sensor surface.

Three peaks at 284.6, 286.3 and 288.6 eV were found in C 1s XPS spectra of ZnS sensor as shown in Figure 2.2a. The first two peaks originate from hydrocarbon contamination [20, 21], and the peak at 284.6 eV is used to calibrate entire XPS spectra. The high energy binding component (288.6eV) with low intensity is attributed to carbonate species that originate from adsorption of carbon dioxide onto oxide and hydroxide groups on the surface [20, 21]. It should also be noted that there was only one peak at 284.6 eV in the C 1s spectrum after Argon sputtering (results not shown), and the absence of the latter two peaks is reasonable since little carbon dioxide and dust from environment is expected in the protection of Argon during sputtering.

The Zn 2p spectrum in Figure 2.2b composes of two states ($2p_{3/2}$ and $2p_{1/2}$), and only one peak was found for each state. The binding energy attributed to Zn $2p_{3/2}$ agrees well with the values reported for Zn^{2+} in an environment of zinc sulfide and zinc oxide (1020.9-1022.1 eV) [11, 22]. Chemical shifts in the Zn 2p peak are relatively small based on which it is hard to conclude if the present peak is due to ZnO or ZnS. The binding energy difference of 23 eV between Zn $2p_{3/2}$ and $2p_{1/2}$ agrees with the previous results reported for zinc sulfide [11, 23]. No peak shape difference or binding energy shift was observed between before and after sputtering. The exact chemical state of Zn was further inferred from S 2p peak and atomic concentration ratio of Zn and S, which were discussed in later section.

It has been widely reported that there are five possible components (sulfide S^{2-}, polysulfide S_n^{2-}, elemental sulphur S_n^0, metal-deficient sulfide and sulfate) in the S 2p spectrum of sphalerite depending on different oxidization and treatment conditions [17, 21, 24-26]. Each component consists of two peaks with the intensity of the lower binding energy peak doubling that of the higher binding energy peak [26]. In this work, as indicated in Figure 2.2c, the S 2p spectrum shows only one doublet (two peaks) with its S $2p_{3/2}$ binding energy at 161.2 eV and its S $2p_{½}$ binding energy at 162.4 eV. It is suggested that this component with its S $2p_{3/2}$ at 161.2 eV is the S^{2-} species of unactivated ZnS [27-29]. Therefore, the XPS result confirms that sulphur exists only in the form of sulfide on the sensor surface. As indicated in Figure 2.2d, the O 1s spectra can be divided into three components, i.e. oxide, hydroxide species and adsorbed water. The band occurring at 530.7 eV is due to the presence of oxide species, while the hydroxide species emit at a slight higher binding energy around 531.5 eV. The binding energy at 533.1 eV in the spectra is attributed to adsorbed water [21, 25]. Among the three components, the one at 531.5 eV shows much higher intensity than other two, which indicates hydroxide is the major component for oxygen on the sensor surface.

Binding energies and line width of characteristic emission of elements of interest are given in Table 2.1, which also includes the atomic concentration of each element detected at the upmost layer of the ZnS sensor. The presence of strong oxygen signal is due to oxide layer on the sensor surface, which is removed after sputtering for 30 s (~1.5 nm), as shown in Figure 2.3.

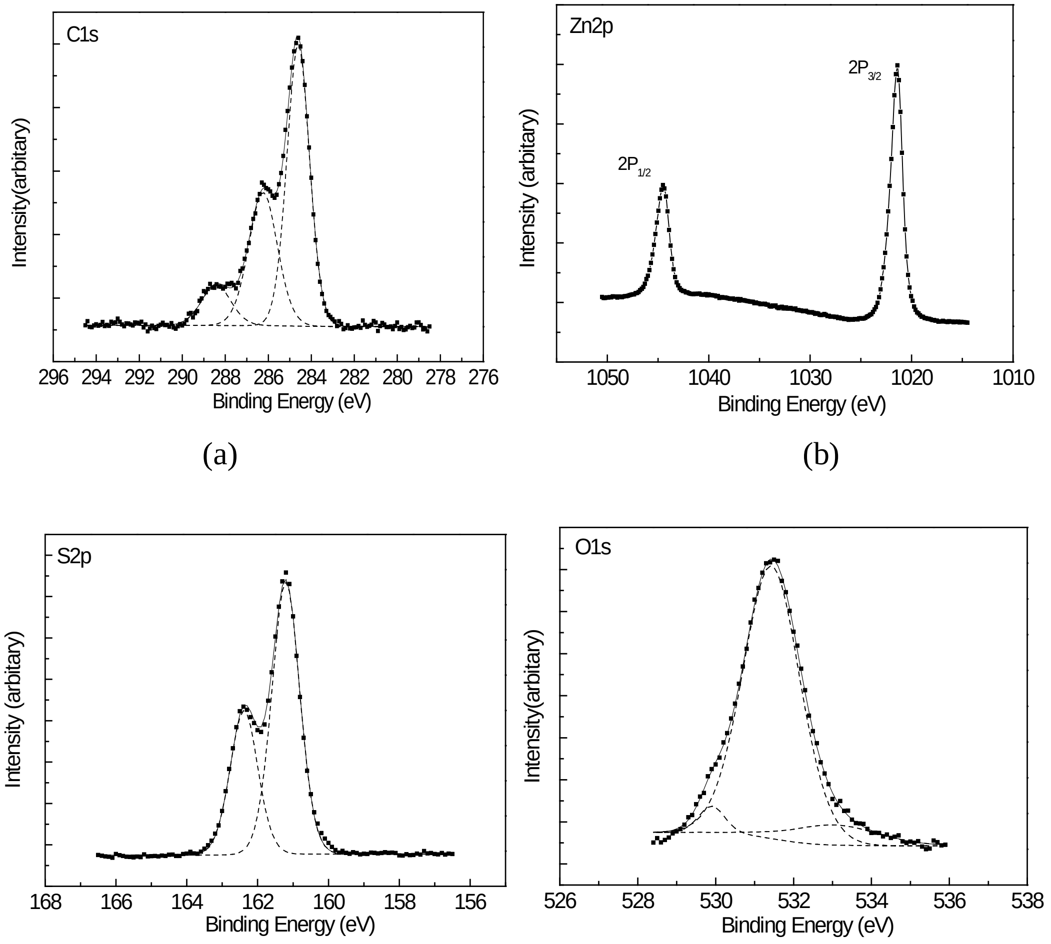

(a) (b)

(c) (d)

Figure 2.2 XPS spectra (C 1s, Zn 2p, S 2p, O 1s) of cleaned ZnS sensor surface.

Table 2.1 Band positions and atomic concentration of elements measured on the upmost surface of cleaned ZnS sensor by XPS.

	Elements detected			
	Zn $2p_{3/2}$	C 1s	O 1s	S $2p_{3/2}$
Binding Energy (eV)	1021.4	284.6	531.5	161.2
fwhm	1.5	1.3	1.9	0.9
Atomic concentration (%)	40.3	15.0	22.2	22.0

XPS sputtering

After initial XPS analysis, argon sputtering was applied to freshly cleaned ZnS sensor at a rate of 3.3 nm/min. As shown in Figure 2.3, four elements (Zn, S, C, O) were detected on the etched sensor surface, and zinc and sulphur were observed in the XPS spectra even after 600 seconds argon ion bombardment, i.e., an etch depth of 33 nm. A 33 nm layer corresponds to 60 unit cell dimensions of zinc sulphide, which is thick enough to perform all activation tests [30]. Within this layer, the ratio of zinc and sulphur concentration remains unity, and the total concentration of both elements exceeds 90%. The presence of small amount of oxygen (~5%) in the zinc sulfide layer was probably due to the presence of small amount of oxygen in the XPS chamber during XPS measurement or the embedded oxygen element during the preparation of ZnS layer by Q-sense.

The spectra of Zn 2p, S 2p and O 1s, in combination of the sputtering-XPS results that show the atomic concentration of each element across the zinc sulfide layer, indicates that the coating on ZnS sensor surface is zinc sulfide (~33 nm) with a slightly oxidized layer (~1.5 nm) at the outmost surface.

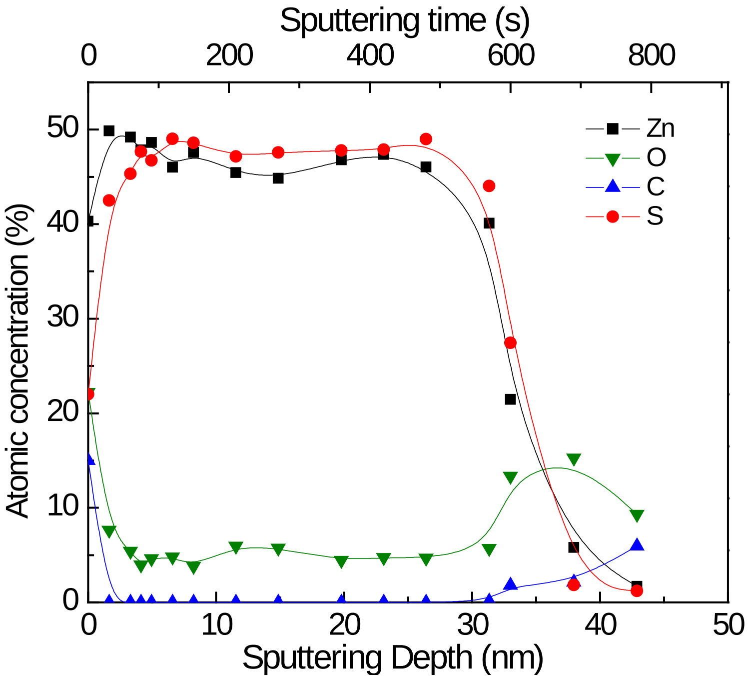

Figure 2.3 Atomic concentrations of four elements detected by XPS *vs.* argon sputtering time (sputtering depth) of freshly cleaned ZnS sensor

2.3.1.4 Potassium amyl xanthate adsorption using QCM-D

It is well known that xanthate hardly adsorbs onto natural sphalerite without activation at pH>2 (although the adsorption may vary for different sphalerite samples) [2, 31, 32]. In order to compare with nature sphalerite samples, the adsorption of potassium amyl xanthate (5×10^{-5} M) on freshly cleaned ZnS sensor was conducted using QCM-D at pH 6.5. As shown in Figure 2.4, no frequency change was observed, indicating that ZnS sensor behave similarly to natural sphalerite in term of xanthate adsorption.

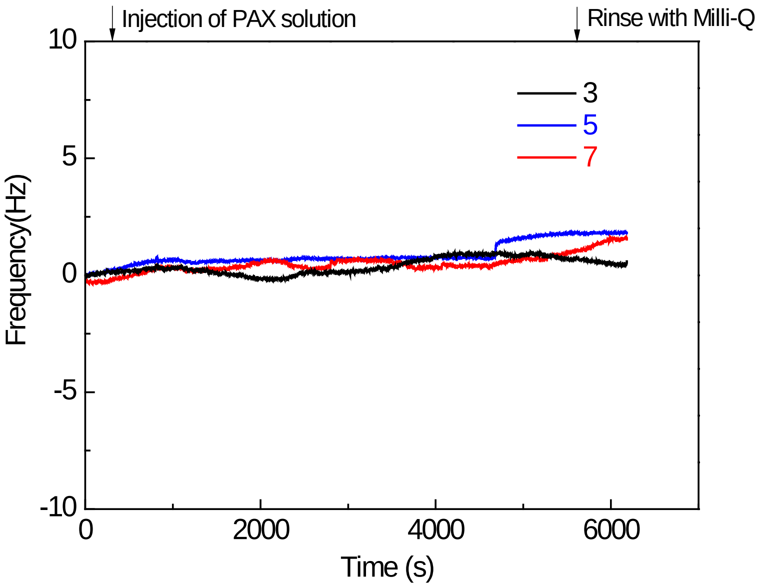

Figure 2.4 QCM-D measurement of potassium amyl xanthate (5×10^{-5}M) adsorption on freshly cleaned ZnS sensor at pH 6.5.

2.3.2 Activation by silver

Upon pumping silver nitrate solution of 2.5×10^{-4} M at pH 5 into the flow module with ZnS sensor mounted, a negative frequency change was observed and accompanied by a small increase in dissipation as shown in Figure 2.5. When the frequency curve reached a plateau, pump was stopped and the flow module was rinsed with Milli-Q water at pH 5 to remove all ions that were not bonded onto the sensor surface. The negative frequency shift in Figure 2.5, due to decrease of the crystal's resonance frequency of oscillation, indicates a mass increase (uptake) of the sensor. The mass increase could be attributed to two aspects: adsorption of silver ions or substitution of zinc atoms on the sensor surface by silver atoms from the bulk solution. The large frequency drop and relatively small dissipation increase ($\Delta D/\Delta f < 2\times10^{-9}$) indicate that it is mainly a zinc-silver substitution process rather than silver ion adsorption, as the latter process always shows overtone dependence of frequency shift and relatively large dissipation increase.

At pH 5, the main species on zinc sulfide surface are |SH and |SZn and there is no zinc hydroxide [33, 34]. During the activation reaction with silver nitrate, the substitution process can be described by the well-established activation mechanism – an ion exchange reaction shown as equation 2 [5]. It clearly shows that solid phase gains mass by replacing one zinc atom with two silver atoms, which leads to the frequency decrease observed in Figure 2.5. Figure 2.6 as shown below illustrates the mass increase (frequency drop) of ZnS sensor due to equation 2.2. The frequency drop can be converted to mass increase in ZnS sensor based on Sauerbrey equation. The silver uptake can be further calculated from mass increase by considering the mass change in solid phase in equation 2, in which ~216 g silver uptake corresponds to ~150.4 g mass increase in solid phase (ZnS sensor) observed from the QCM-D measurement.

The real-time silver uptake is shown in Figure 2.7a, from which two regimes can be identified and fitted with different kinetic laws as shown in Figure 2.7b. Logarithmic and parabolic equations were used to fit the curve in each regime very well, shown in Figure 2.7c and 2.7d. The reaction in the logarithmic regime started from the injection of silver nitrate solution and ended at around 18 minutes. The later regime followed parabolic kinetics and lasted for ~4 hours, which was expected to continue with the presence of sufficient silver nitrate in the bulk solution [8]. Similar results were reported by Jain and Fuerstenau [13] who found the first and second stage lasted for 15 min and 64 hours, respectively. Using a QCM-D, the present work confirmed the two-stage reaction during zinc sulfide activation by silver ions, e.g., direct logarithmic kinetics in the initial state followed by a parabolic law.

The logarithmic-dependence silver uptake observed in the first stage can be described by the Elovich model, which has been widely applied to describe the adsorption kinetics of gas adsorption on solid surfaces [35], adsorption of phosphate on gibbsite [36], phosphate and arsenate on goethite [37] and kinetics of silicate adsorption and desorption on aluminum hydroxide [38]. The derivative form of Elovich model is given by:

$$\frac{d\Gamma}{dt} = \alpha exp(-\beta\Gamma) \qquad 2.4$$

where Γ is the quantity of adsorbent adsorbed during the time t, α and β are constants during the experiment.

By analogy with the growth rate of oxide film, Ralston et al. [9] suggested that the probability that one activator atom (silver in this case) jumped to a lattice site of zinc sulfide should be:

$$s = v exp(-\Delta E/kT) \qquad 2.5$$

where s is the probability, ν is the ionic vibration frequency, k is Boltzmann constant, T is the absolute temperature and ΔE is activation energy or energy barrier height. Therefore, the rate of uptake could be obtained by multiplying the amount of vacant sites by the probability of single activator atom jumping to one vacant site.

$$\frac{d\Gamma}{dt} = As = A\nu exp(-\Delta E/kT) \qquad 2.6$$

where A is a constant and Γ is adsorbed quantity during the time t. If the activation energy is proportional to uptake of activator or surface coverage ($\Delta E \propto \Gamma$ [39], equation 2.6 becomes:

$$\frac{d\Gamma}{dt} = B\nu exp(-\Gamma/kT) \qquad 2.7$$

where B is a constant. According to equation 2.4, the uptake of activator can be described with the Elovich model (see equation 2.4).

It should be noted that two important assumptions have to be made in deriving equation 2.7. First, the probability of one activator atom incorporating into zinc sulfide lattice has to be described with an exponential function of adsorbed quantity, although there are some experimental and theoretical evidences to support this assumption. [40, 41] Second, the amount of vacant lattice sites should be very large so that A in equation 2.6 is not a function of Γ, which may not be always true in certain adsorption systems. It should also be noted that it is hard to infer the adsorption mechanism based only on the fitting of kinetic data to a particular model. The kinetics and mechanism of zinc sulfide activation will be continuously investigated in future study.

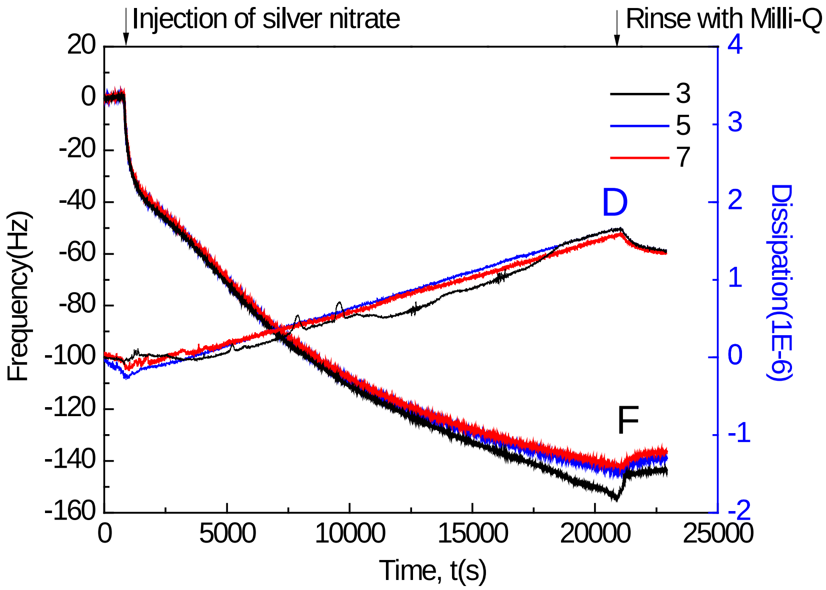

Figure 2.5 Frequency and dissipation changes with time during the QCM-D measurement on the activation of zinc sulfide sensor by silver nitrate solution. A baseline with Milli-Q water (pH=5) was stabilized at first 13 minutes, and silver nitrate solution (pH=5) with concentration of $2.5*10^{-4}$ M was pumped into the chamber at a flow rate of 0.15 ml/min. 30 Hz frequency drop was observed for all three overtones (n=3, 5 and 7) within 5 minutes right after the injection while the dissipation kept constant at the range of $0.3\text{-}0.1\times10^{-6}$. Thereafter, frequency continued to decrease at a lower rate than the initial rapid drop. Data at multiple overtones (n=3, 5 and 7) are presented to show the overlap of different overtones, which indicates the adsorbed layer is rigid and thin.

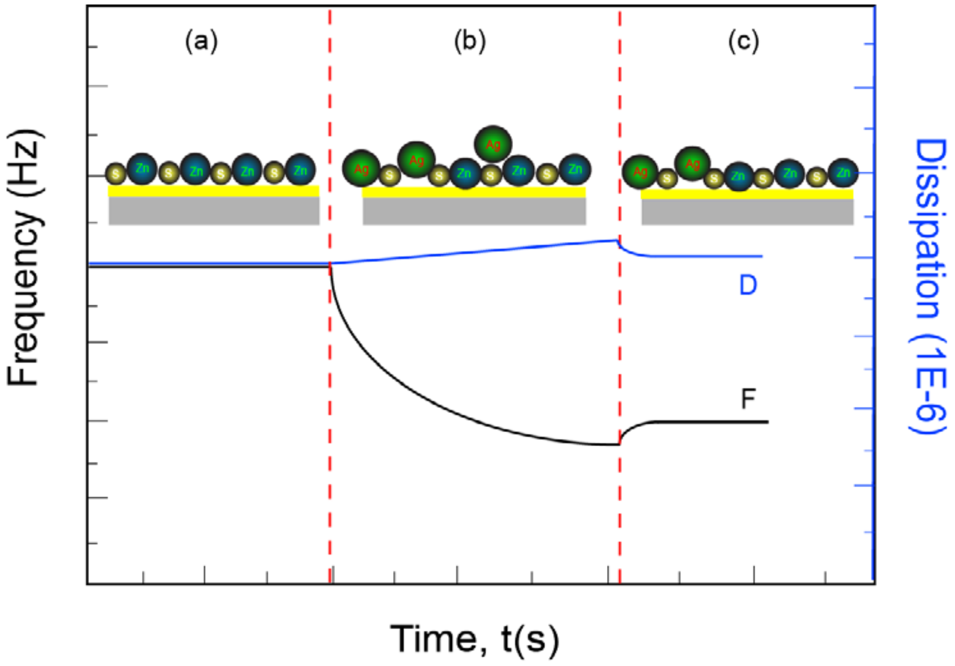

Figure 2.6 Schematic drawing of the mass increase of ZnS sensor during silver activation measurement using QCM-D. (a) rinsing the cleaned ZnS sensor with Milli-Q water; (b) injecting silver nitrate solution into the chamber where zinc on the surface were substituted by silver from bulk solution; (c) rinsing the QCM-D chamber with Milli-Q water to remove the ions that were not strongly bonded to the sensor surface.

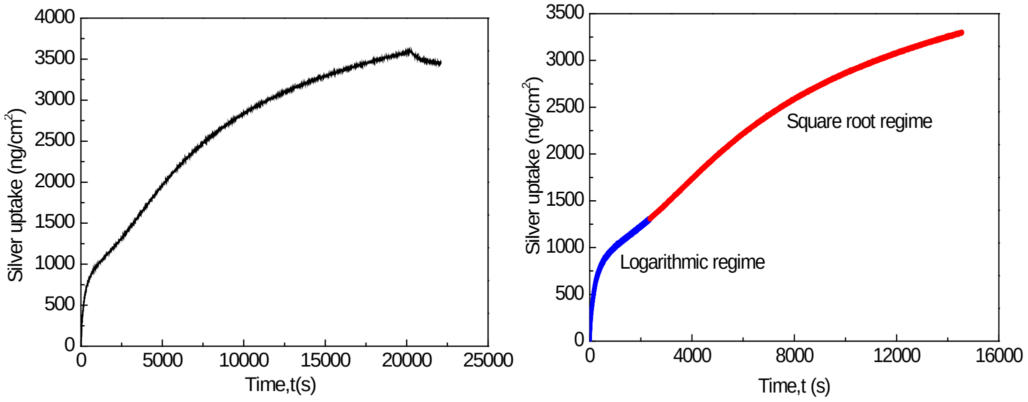

(a) (b)

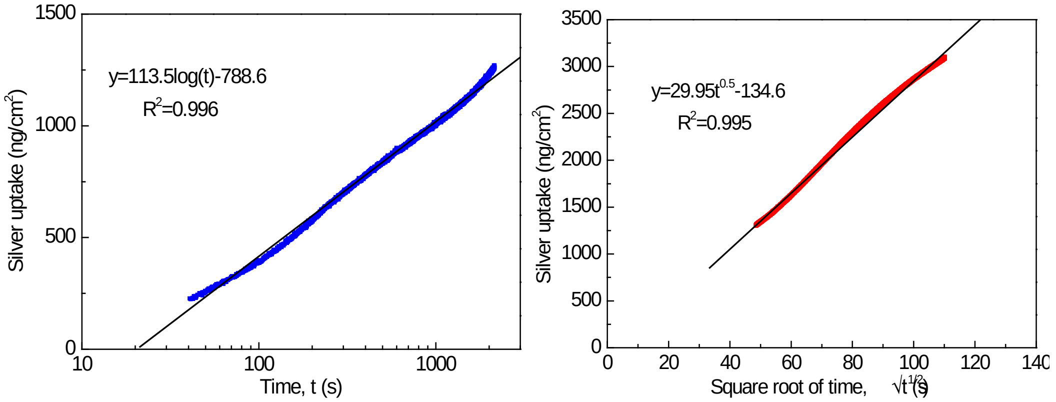

(c) (d)

Figure 2.7 ZnS activation kinetics converted from the QCM-D data in Figure 2.5. (a) Silver uptake calculated from ΔF (n=5) versus time. (b) Silver uptake calculated from ΔF (n=5) showing the two mathematical regimes. (c) Logarithmic fitting for the first regime. (d) Parabolic fitting for the second regime.

2.3.3 Potassium amyl xanthate adsorption

After activation with silver, purified potassium amyl xanthate (PAX) with a concentration of 5×10^{-5} M at pH 5 was pumped through the QCM-D flow module. Figure 2.8 shows the frequency and dissipation shift of activated ZnS sensor upon pumping the PAX solution.

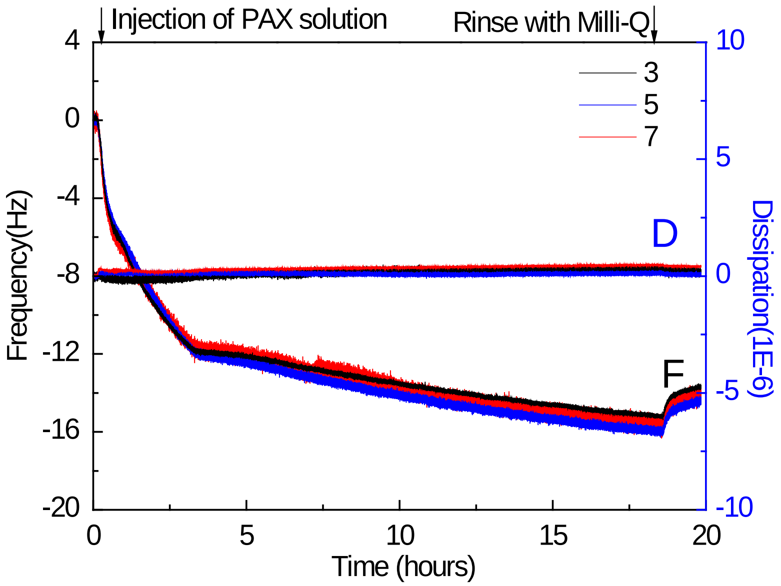

Figure 2.8 Frequency and dissipation changes with time for QCM-D monitoring of potassium amyl xanthate adsorption on activated ZnS sensor with silver at pH=5. A baseline with Milli-Q water (pH=5) was stabilized at about 10 minutes, and potassium amyl xanthate solution (pH=5) with concentration of 5×10^{-5} M was pumped into the chamber at a flow rate of 0.15 ml/min.

A sharp frequency drop (~3 Hz) was observed for the first 10 minutes, followed by a continuous drop at decreased rate to 12 Hz after 3 hours. In the following 15 hours, the frequency only dropped by another 2 Hz. The frequency drop was due to the adsorption and reaction of PAX with the activated ZnS sensor surfaces as shown in equation 2.8 [42]:

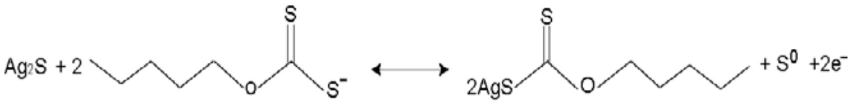

2.8

Fully covering the activated (molecularly smooth) ZnS sensor by a monolayer of potassium amyl xanthate would cause a 9.2 Hz frequency drop, based on the assumption that each head group of xanthate occupies an area of 20.8 $Å^2$ and the xanthate molecules are densely packed on the sensor surface. Thus the 12 Hz frequency drop indicates that the adsorbed xanthate on activated ZnS sensor (with rms~2 nm) is densely packed, which is also demonstrated by the low dissipation (0.4×10^{-6} for 18hours). After the experiment, the ZnS sensor was rinsed thoroughly with Milli-Q water and dried with nitrogen. The contact angle of water on the ZnS sensor surface with adsorbed xanthatewas was 95±1.5°, compared with 40±2.6°of clean ZnS sensor surface, suggesting the sensor surface became more hydrophobic after adsorption of xanthate. The contact angle measurement together with the observed frequency drop confirm the adsorption of a PAX layer on activated ZnS sensor, which modulates the wetability of ZnS surface via binding one end of the PAX molecule (EX^-) to the surface site with Ag^+ and exposing the other end ($-CH_3$) to solution phase.

2.3.4 X-ray photoelectron spectroscopy

Broad scan XPS results for freshly cleaned and silver activated ZnS sensors are shown in Figure 2.9. The two spectra (a) and (b) are similar in general but with two major differences. Silver was only observed in the spectra (b) in Figure 2.9 and the intensity of zinc on activated ZnS sensor (b) is lower than that of cleaned ZnS sensor (a). The presence of silver and the decrease in zinc intensity on the activated ZnS sensor surface, to some extent, demonstrate the zinc-silver exchange reaction during QCM-D measurement.

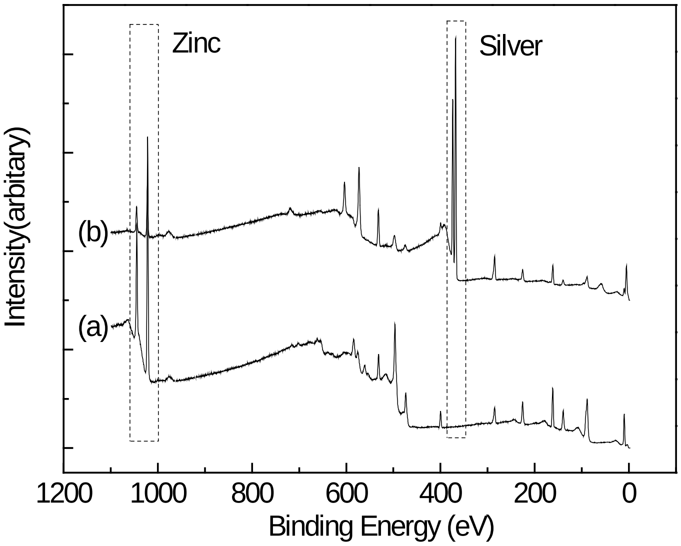

Figure 2.9 Broad scan XPS spectra for (a) clean ZnS sensor and (b) activated ZnS sensor by 2.5×10^{-4} M silver nitrate solution at pH 5 flowing through QCM-D flow module for 5 hours at a flow rate of 0.15 ml/min.

Figure 2.10 shows the high resolution XPS spectra of Ag 3d and S 2p of activated ZnS sensor. As shown in Figure 2.10a, the binding energy of Ag $3d_{5/2}$ is determined to be 367.8 eV, which agrees well with the value reported previously for Ag_2S [43-45]. The formation of Ag_2S is further supported by the measured S 2p binding energy value of 161.4eV as shown in Figure 2.10b [45, 46].

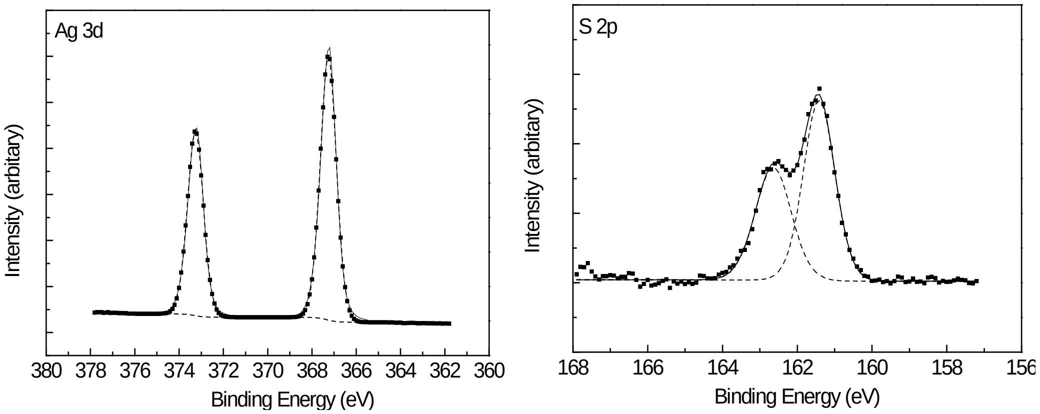

(a)

(b)

Figure 2.10 XPS spectra (a) Ag 3d and (b) S 2p of activated ZnS sensor by silver.

2.3.5 X-ray photoelectron spectroscopy-argon sputtering

After initial XPS analysis, argon sputtering was applied to silver activated ZnS sensors at a rate of 3.3 nm/min. Figure 2.11 shows the atomic concentrations of zinc, sulphur and silver as a function of sputtering time. Silver is observed to be on the surface till 200 seconds of sputtering, which corresponds to a depth of 11 nm. The results confirm the zinc-silver exchange reaction and the penetration of silver into zinc sulfide lattices.

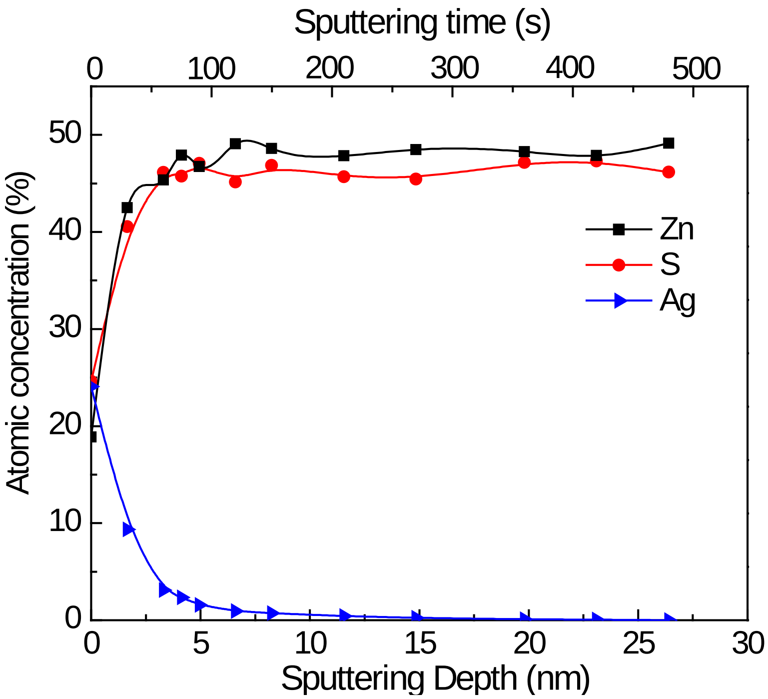

Figure 2.11 Atomic concentration of Zn, Ag and S detected by XPS *vs* argon sputtering time (sputtering depth) of activated ZnS sensor with silver nitrate solution of 2.5×10^{-4} M.

2.4 Conclusions

Taking advantage of the unique ability of QCM-D to simultaneously monitor mass and structure change with superior precision in mass (0.1 ng/cm^2), we employed a commercially available ZnS sensor to study the zinc sulfide activation by silver for the first time in the field of mineral processing. The following conclusions were derived from this work:

1) The zinc sulfide coating on ZnS sensor (Q-sense) used in this study had the similar surface properties as natural sphalerite. Three characteristic peaks of sphalerite were found in the X-ray diffraction pattern of zinc sulfide coating on ZnS sensor surface. The XPS spectra of Zn 2p and S 2p indicated the coating layer was zinc sulfide with a thickness of 33 nm confirmed by argon sputtering. It was found that potassium amyl xanthate did not adsorb onto clean ZnS sensor surface during QCM-D measurement, which was the same as natural sphalerite.

2) ZnS sensor was found to be successfully activated by silver. The frequency drop upon injection of silver nitrate solution at pH 5 indicated a mass increase of ZnS sensor. The relatively large frequency drop and low dissipation increase implied that it was the substitution of zinc atoms by silver leading to the observed frequency drop, not pure silver ion adsorption. Potassium amyl xanthate adsorption onto activated ZnS sensor was confirmed and monitored by the QCM-D measurement, and the adsorbed amount was close to a densely packed monolayer. The significant wettability change (from hydrophilic to hydrophobic) of ZnS sensor after QCM-D measurement further demonstrated the adsorption of xanthate onto activated ZnS sensor surface.

3) With the extreme sensitivity of monitoring a mass change of 0.1 ng/cm^2 within 0.5 second by QCM-D, two domains were found on the curve of silver uptake *vs* time: a logarithmic kinetics region followed by a parabolic kinetics region, which agrees with some of the previous studies using other techniques. Meanwhile, it is suggested that a single logarithmic law reported in some previous studies was probably due to the limitation of the techniques used which could not collect enough sensitive data within a reasonable period of time. Different adsorption kinetics provide useful information on the possible reaction mechanisms involved, i.e., Elovich model in the form of logarithmic equation is the characteristic of chemisorption involving valency forces through sharing or the exchange of electrons between activator and zinc sulfide , and parabolic equation indicates that the rate-determining step in adsorption process is the diffusion of activator atom into bulk of zinc sulphide [7].

4) After activation with silver during QCM-D measurement, the XPS spectra confirmed that the activation product was silver sulfide, and silver ion was found to diffuse into bulk of zinc sulfide layer.

In this study, QCM-D has been demonstrated to be capable of *in-situ* studying zinc sulfide activation kinetics with high precision in both time and mass. Detailed characterization of the activation kinetics sheds some light on the fundamental mechanism of mineral activation that has been a critical issue of study on sphalerite flotation for decades.

Supporting Information

In-situ kinetics study of zinc sulfide activation using a quartz crystal microbalance with dissipation (QCM-D)

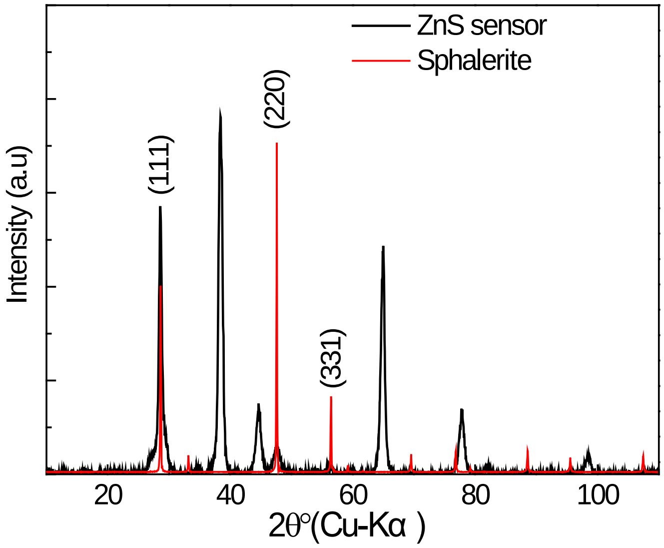

Figure s2.1 X-ray diffraction pattern of ZnS sensor and sphalerite

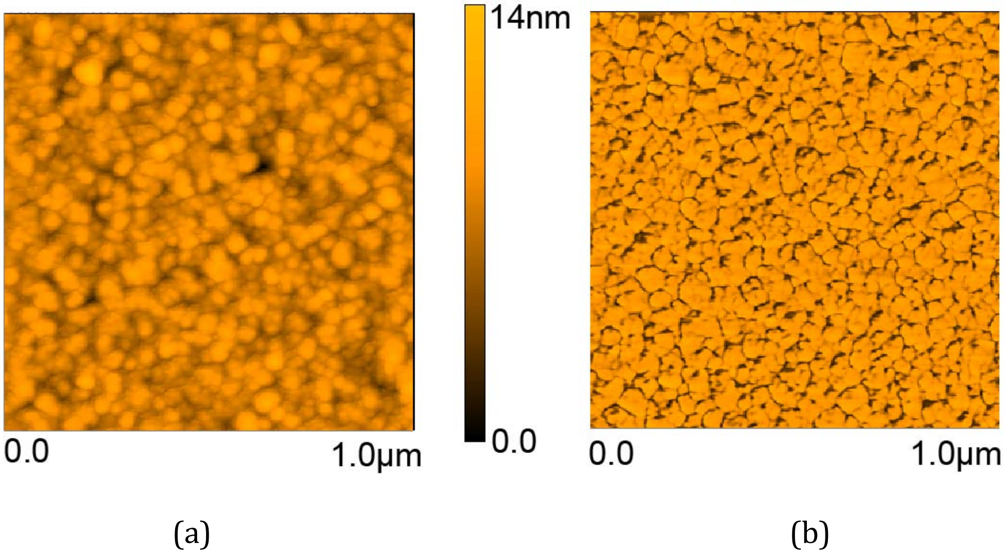

(a)

(b)

Figure s2.2 Topographic (a) and phase contrast (b) AFM images of freshly cleaned ZnS sensor

2.5 References

[1] M.C. Fuerstenau, G.J. Jameson, R.H. Yoon, Froth flotation: a century of innovation, Society for Mining Metallurgy, 2007.

[2] A.M. Gaudin, Flotation, McGraw-Hill, 1957.

[3] N. Finkelstein, S. Allison, M. Fuerstenau, AIME. New York, l976. pp. 4l4-457.

[4] N. Finkelstein, International Journal of Mineral Processing, 52 (1997) 81-120.

[5] A. Gaudin, D. Fuerstenau, M. Turkanis, Trans. Am. Inst. Mining Met. Engrs, 203 65-69.

[6] R. King, South African Institute of Mining and Metallurgy, Kelvin House, 2 Holland St, Johannesburg, South Africa, 1982. 268, (1982).

[7] C. Sui, D. Lee, A. Casuge, J. Finch, Minerals and Metallurgical Processing(USA), 16 (1999) 53-61.

[8] A. Gaudin, H. Sfledden, M. Corriveau, Mining Engineering, (1951).

[9] J. Ralston, T.W. Healy, Int. J. Miner. Process., 7 (1980) 175-201.

[10] J. Ralston, T.W. Healy, Int. J. Miner. Process., 7 (1980) 203-217.

[11] I. Kartio, C. Basilio, R.H. Yoon, Langmuir, 14 (1998) 5274-5278.

[12] K.S.E. Forssberg, Stockholm, Sweden, June 1984, (1984) 1985.

[13] S. Jain, D. Fuerstenau, Flotation of Sulphide Minerals, (1984) 159-174.

[14] M. Rodahl, F. Hook, C. Fredriksson, C.A. Keller, A. Krozer, P. Brzezinski, M. Voinova, B. Kasemo, Faraday Discuss., 107 (1997) 229-246.

[15] S.R. Rao, Xanthates and related compounds, M. Dekker, 1971.

[16] P. Ekholm, E. Blomberg, P. Claesson, I.H. Auflem, J. Sjöblom, A. Kornfeldt, J. Colloid Interface Sci., 247 (2002) 342-350.

[17] J.D.G. Durán, M.C. Guindo, A.V. Delgado, F. González-Caballero, J. Colloid Interface Sci., 193 (1997) 223-233.

[18] J. Vidal, O. de Melo, O. Vigil, N. Lopez, G. Contreras-Puente, O. Zelaya-Angel, Thin Solid Films, 419 (2002) 118-123.

[19] International Centre for Diffraction Data, 04-004-3804 (Cubic ZnS).

[20] A. Boulton, D. Fornasiero, J. Ralston, Int. J. Miner. Process., 70 (2003) 205-219.

[21] G. Fairthorne, D. Fornasiero, J. Ralston, Int. J. Miner. Process., 49 (1997) 31-48.

[22] M.N. Islam, T. Ghosh, K. Chopra, H. Acharya, Thin Solid Films, 280 (1996) 20-25.

[23] S.H.R. Brienne, Q. Zhang, I.S. Butler, Z. Xu, J.A. Finch, Langmuir, 10 (1994) 3582-3586.

[24] R.S. Smart, W.M. Skinner, A.R. Gerson, Surf. Interface Anal., 28 (1999) 101-105.

[25] A. Buckley, R. Woods, H. Wouterlood, Int. J. Miner. Process., 26 (1989) 29-49.

[26] A. Pratt, ECS Meeting Abstracts, 1001 (2010) 1357.

[27] T. Khmeleva, T. Georgiev, M. Jasieniak, W. Skinner, D. Beattie, Surf. Interface Anal., 37 (2005) 699-709.

[28] G.J. Janz, J.R. Downey, E. Roduner, G.J. Wasilczyk, J.W. Coutts, A. Eluard, Inorg. Chem., 15 (1976) 1759-1763.

[29] C.A. Prestidge, W.M. Skinner, J. Ralston, R.S.C. Smart, Appl. Surf. Sci., 108 (1997) 333-344.

[30] C.A. Prestidge, A.G. Thiel, J. Ralston, R.S.C. Smart, Colloids and Surfaces A: Physicochemical and Engineering Aspects, 85 (1994) 51-68.

[31] J. Leppinen, Int. J. Miner. Process., 30 (1990) 245-263.

[32] N. Finkelstein, S. Allison, Fuerstenau, MC, Editor, (1976) 414-457.

[33] R. Williams, M.E. Labib, J. Colloid Interface Sci., 106 (1985) 251-254.

[34] L. Rönngren, S. Sjöberg, Z.-X. Sun, W. Forsling, J. Colloid Interface Sci., 162 (1994) 227-235.

[35] J.A. Schwarz, C.I. Contescu, Surfaces of nanoparticles and porous materials, CRC, 1999.

[36] R.J. Atkinson, J.P. Quirk, A.M. Posner, Journal of Inorganic & Nuclear Chemistry, 34 (1972) 2201-&.

[37] J. Zhang, R. Stanforth, Langmuir, 21 (2005) 2895-2901.

[38] N. Anderson, A.J. Rubin, Adsorption of inorganics at solid-liquid interfaces, Ann Arbor Science Publishers, Inc., 1981.

[39] A. Dąbrowski, V. Tertykh, Adsorption on new and modified inorganic sorbents, Elsevier Science, 1996.

[40] J. Engstrom, T. Engel, Physical Review B, 41 (1990) 1038.

[41] D.D. Eley, P.R. Wilkinson, Proceedings of the Royal Society of London. Series A, Mathematical and Physical Sciences, 254 (1960) 327-342.

[42] A.N. Buckley, R. Woods, Colloids and Surfaces A: Physicochemical and Engineering Aspects, 104 (1995) 295-305.

[43] J. Vinkevicius, I. Mozginskiene, V. Jasulaitiene, J. Electroanal. Chem., 442 (1998) 73-82.

[44] V.K. Kaushik, J. Electron. Spectrosc. Relat. Phenom., 56 (1991) 273-277.

[45] S. Shukla, S. Seal, S. Mishra, J. Sol-Gel Sci. Technol., 23 (2002) 151-164.

[46] N. Turner, J. Murday, D. Ramaker, Anal. Chem., 52 (1980) 84-92.

Chapter 3 Activation of zinc sulfide by copper and lead in neutral and alkaline media-an adsorption kinetics study

3.1 Introduction

Sphalerite can be activated by heavy metal ions to enhance the adsorption of thiols collector, which renders the surface hydrophobicity by forming insoluble metal xanthate on sphalerite surface. It is well known that the activation reaction is sensitive to pH. At acidic pH, many researchers agree that it is an ion exchange process in which zinc atom is substituted by activator atom. At neutral and alkaline pH there are, however, large discrepancies in the theories on activation mechanism. The objective of present study is to investigate the mechanism of zinc sulfide activation in neutral and alkaline media from the perspective of activation kinetics.

It is well documented that sphalerite can be activated by copper in neutral and alkaline media, although the flotation of sphalerite in the presence of copper is depressed in pH range of 6 to 9, depending on the amount of copper added [1]. Different from the well accepted ion exchange of Cu^{2+} and Zn^{2+} mechanism under acidic condition, the activation of sphalerite by copper under neutral and alkaline condition involves the interaction between copper hydrolysis species and sphalerite surface. Jain and Fuerstenau [2] and Laskowski et al. [3] extended the activation mechanism under acidic condition to alkaline condition by considering the presence of copper hydroxide species ($Cu(OH)^+$, $Cu(OH)_2$ and $\mathrm{Cu(OH)}_3^-$), which served as a “pool” to supply the Cu^{2+} that activated sphalerite via the ion exchange mechanism under acidic condition. The reaction can be represented as:

$$Cu(OH)_x^{2-x} \rightarrow Cu^{2+} + +xOH^- \qquad 3.1$$

$$|ZnS + Cu^{2+} \rightarrow |CuS + Zn^{2+} \qquad 3.2$$

Combining two equations gives:

$$|ZnS + Cu(OH)_x^{2-x} \rightarrow |CuS + Zn(OH)_x^{2-x} \qquad 3.3$$

Girczys et al. [4] proposed another adsorption mechanism for ZnS activation by $Cu(OH)^+$ at neutral pH:

$$Zn - OH_{surface} \ + Cu(OH)^+ \rightarrow Zn - O - Cu_{surface}^+ \ + H_2O \qquad 3.4$$

From equation 3.4, it can seen that the activated sphalerite becomes positively charged, which has been confirmed by others [3, 5, 6].

Considering the presence of $Zn(OH)_2$ at alkaline pH, Girczys et al. [4] suggested the mechanism of sphalerite activation by copper as:

$$ZnS + 2OH^- \rightarrow |Zn(OH)_2 + S|^{2-}_{surface} \qquad 3.5$$

$$|Zn(OH)_2 + S|^{2-}_{Surface} + Cu^{2+}_{aq} \rightarrow Zn(OH)_{2(surface\ )} + CuS_{surface} \qquad 3.6$$

The elemental sulphur at the surface has been demonstrated to be instable at alkaline pH; therefore, the proposed mechanism is not viable [7].

There is also plentiful evidence that lead can activate sphalerite. Trahar et al. [8] demonstrated that sphalerite could be floated upon addition of lead ions up to pH 9. Rashchi et al. [9] found that the recovery of sphalerite activated by lead significantly depended on contamination and flotation pH, and the flotation of sphalerite was apparently depressed at contamination pH above 9 or flotation pH above 10. However, the activation mechanism with lead is poorly understood compared to copper activation. At acidic pH, Basilio et al. [10] found that lead activation of sphalerite occurred through a similar ion exchange mechanism to copper activation under acidic condition. Chandra and Gerson [11], quoting Pattrick et al. [12], showed that lead ion was not compatible in zinc sites in a sphalerite lattice and the exchange process was not energetically favourable. At alkaline pH, more studies support the adsorption of lead hydrolysis species rather than ion exchange of Pb and Zn [9, 13]. By analogy with mechanism for copper activation, Houot and Ravenau [14] and Rashchi et al. [9] proposed following surface reaction applicable at neutral and moderately alkaline pH:

$$|SZn - OH_{surface} + Pb(OH)^+ \rightarrow |SZn - O - Pb^+_{surface} + H_2O \qquad 3.7$$

Or a more general form for all hydrolysis species:

$$|SZn - OH_{surface} + Pb(OH)^{2-x}_x \rightarrow |SZn - O - Pb^+_{surface} + xOH^- + H^+ \qquad 3.8$$

At higher pH (10-12) where $Pb(OH)_{2(s)}$ forms, the lead hydroxide adsorbed onto sphalerite surface, depressing the flotation, which is represented as:

$$|SZn - OH_{surface} + Pb(OH)_{2(s)} \rightarrow |SZnOH(Pb(OH)_{2(s)})_{surface} \qquad 3.9$$

It remains questionable why the flotation of activated sphalerite by lead at high pH (>10) is depressed.

There are more arguments on the kinetics aspect of activation reaction under neutral and alkaline condition. The time scale for copper activation at alkaline pH could be several hours [3, 15], which does not conform to plant practices where the conditioning times for copper activation of sphalerite are only a few minutes [16]. Fuerstenau and Metzger [17] reported that, based on solution analysis, the adsorption of Pb(II) was quite slow and could be described by a power law. Ralston et al. [7] followed the copper and lead activation reaction for up to two hours under neutral to weakly alkaline condition using ion-selective electrodes. For both copper and lead, the metal ion uptake was enhanced, compared with activation at acidic pH values. At least two steps were observed in the activation reaction when it comes to fit the real-time metal ion uptake curves with different mathematical equations. For the first activation step, the copper and lead ions uptakes followed a logarithmic equation. It was found that 1-1.5 layers of copper and about 0.3 layer of lead on sphalerite surface were achieved in the first step that lasted for 5 minutes. In second step, the copper uptake still obeyed a logarithmic law but with a lower rate, while there was no equation that could describe the lead uptake. Sui et al. [16] showed that, based on metal ion content analysis using atomic analysis spectroscopy, the copper adsorption rate at pH 6 and 9.2 was characterized by two stages: a rapid stage that occurred over first minute and followed logarithmic equation and a slow stage that fitted a parabolic equation. The exchange ratio of Cu to Zn was close to one at three pH values(3, 6 and 9), implying the nature of ion exchange. Three stages were found in the lead uptake curves at pH 6 and 9.2, and all of them followed logarithmic equation. The adsorption rate of lead increased as pH increased from 3 to 9. Different from copper activation, the exchange ratio of Pb to Zn was much higer than one.

The above mechanism discussions imply that the nature of the activation reaction under neutral and alkaline condition is the adsorption of heavy metal hydrolysis species onto Sphalerite (zinc sulfide) surface. However, no theoretical kinetics model has been used to describe the adsorption of heavy metal ions on zinc sulfide surface although extensive experimental studies on activation have been done. In recent years, many reserchers have studied the adsorption of heavy metal ions on the surface of metal oxide, and numerous kinetics models have been developed and used to fit the kinetics data. The objective of this study was to apply these well-accepted models to investigate the kinetics of copper and lead ions adsorption onto zinc sulfide surface at neutral to alkaline pH, at which the surface property of zinc sulfide is similar to metal oxide since both carries negative surface charge [18].

Given the demonstrated ability of quartz crystal microbalance (QCM-D) with dissipation to study zinc sulfide activation [19] where a ZnS sensor was used to represent zinc sulfide, the zinc sulfide activation with copper and lead at neutral and alkaline pH was investigated. The kinetics of xanthate adsorption on activated ZnS was also investigated using a QCM-D.

3.2 Experimental

3.2.1 Theretical basis

Predicting and measuring the rate of adsorption a given system is one of the most important manners to understand the mechanism of adsorption process. The adsorption process can be expressed as the form of chemical reaction as equation 3.10:

$$A + n * \leftrightarrow A(*)_m \tag{3.10}$$

Where A is the sorbent and * represents the available vacant sites on surface of the adsorbent , and *n* is the number of surface sites occupied by each molecule of sorbent (A). In most cases, the adsorption rate can be espressed as:

$$\frac{d\Phi}{dt} = k_{ad} C(\Phi_0 - \Phi)^m - k_d \Phi \tag{3.11}$$

Where k_{ad} and k_d are the adsorption and desorption rate constants and Φ_0 and Φ is the initial concentration of vacant sites at t=0 and the concentration of sites occupied by sorbent at t=t, respectively. C is the concentration of sorbent in the solution phase at time t.

Based on different assumption, numerous widely used kinetics models can be derived from equation 3.11. In this study, pseudo-first order, pseudo-second order and Elovich models were used to fit the kinetics data of zinc sulfide activation.

3.2.1.1 Pseudo-first order

When m=1 and the concentration of sorbent is very high compared to the adsorbed amount on the surface, equation 3.11 can be rewriten as

$$\frac{d\Phi}{dt} = k_{ad}C(\Phi_0 - \Phi) - k_d\Phi \tag{3.12}$$

By defining $\theta=\Phi/\Phi_0$, the surface coverage fraction $(0 \leq \theta \leq 1)$ at time t, equation 3.12 becomes

$$\frac{d\theta}{dt} = k_{ad}C - (k_{ad}C + k_d)\theta \tag{3.13}$$

Rearrange and integrate equation 3.13 from 0 to t,

$$\int_0^{\theta} \frac{d\theta}{k_{ad}C-(k_{ad}C+k_d)\theta} = \int_0^t dt \tag{3.14}$$

$$ln\left(1 - \frac{k_{ad}C+k_d}{k_{ad}C}\theta\right) = -(k_{ad}C + k_d)t \tag{3.15}$$

$$\theta = \frac{k_{ad}C}{k_{ad}C+k_d}(1 - e^{-(k_{ad}C+k_d)t}) \tag{3.16}$$

At $t\rightarrow\infty$, the adsorption is in equilibrium, $\theta=\theta_e$, so Equation 3.16 becomes

$$\theta_e = \frac{k_{ad}C}{k_{ad}C+k_d} \tag{3.17}$$

The observed rate constant of the pseudo-first order model is

$$k_1 = k_{ad}C + k_d \tag{3.18}$$

By inserting equation 3.17 and 3.18 into equation 3.16, we obtain

$$\theta = \theta_e(1 - e^{-k_1t}) \tag{3.19}$$

For most adsorption processes, the quantity of solute sorbed is proportional to the surface coverage at any time.

$$\frac{q}{q_e} = \frac{\theta}{\theta_e} \tag{3.20}$$

where q and q_e is the quantity of solute sorbed at time t and equilibrium, respectively.

And therefore equation 3.19 converts to

$$q = q_e(1 - e^{-k_1t}) \tag{3.21}$$

3.2.1.2 Pseudo-second order

When m= 1 and the concentration of solute is not high enough, C term in equation 3.11 is no longer a constant.

$$\frac{d\theta}{dt} = k_{ad}\,(C_0 - \rho\theta)(1 - \theta) - k_d\theta \tag{3.22}$$

Where C_0 is the initial concentration of solute at t=0 and $\beta\theta$ is the adsorbed amount of solute at time t, and σ is

$$\sigma = \frac{C_0 - C_e}{\theta_e} \tag{3.23}$$

By integrating equation 3.22, we obtain the expression of q in a linear form [20]

$$\frac{t}{q} = \frac{1}{k_2 q_e^2} + \frac{t}{q_e} \tag{3.24}$$

Where k_2 is the observed rate constant of pseudo-second order model.

At m=2, if the concentration of solute (C) is high and the $k_d\theta$ term in equation 3.11 is small compared to the first term, equation 3.11 becomes

$$\frac{d\Phi}{dt} = k_{ad}\,C(\Phi_0 - \Phi)^2 \tag{3.25}$$

We know that at equilibrium $d\Phi/dt$=0, and therefore the concentration of sites occupied by solute is Φ_0 at equilibrium. Assuming every molecule of solute occupies μ sites at any time of the adsorption process, we will have

$$\frac{q}{\Phi} = \frac{q_e}{\Phi_0} \propto \mu \tag{3.26}$$

Rewrite equation 3.26

$$\frac{\Phi_0 - \Phi}{q_e - q} = \frac{\Phi}{q} \tag{3.27}$$

Inserting equation 3.27 into equation 3.25 gives

$$\frac{dq}{dt} = k_{ad}\,C\gamma(q_e - q)^2 \tag{3.28}$$

Where γ is a constant, proportional to μ in equation 17.

Separating the variables in equation 19 gives

$$\frac{dq}{(q_e - q)^2} = k_{ad}\,C\gamma dt \tag{3.29}$$

And integrating this for the boundary conditions t=0 to t=t and q=0 to q=q, gives

$$q = \frac{q_e^2 k_{ad}\,C\gamma t}{1 + q_e k_{ad}\,C\gamma t} \tag{3.30}$$

which has a linear form of

$$\frac{t}{q} = \frac{1}{k_{ad}\,C\gamma q_e^2} + \frac{t}{q_e} \tag{3.31}$$

Compare equation 3.24 and 3.31, we know the observed rate k_2=$k_{ad}\,C\gamma$ in this senario.

3.2.1.3 Elovich model

When *m*=1, equation 3.11 can be coverted to equation 3.32

$$\frac{d\Phi}{dt} = k_{ad}\,C(\Phi_0 - \Phi) - k_d\Phi \qquad 3.32$$

Substitute Φ with q based on equation 3.27

$$\frac{dq}{dt} = k_{ad}\,C(q_e - q) - k_d q \qquad 3.33$$

By defining C_0 as initial concentration of the solute and V as the volume of the container, so the concentration of solute at time t is

$$C = C_0 - \frac{q}{V} \qquad 3.34$$

Inserting equation 3.24 into equation 3.33 gives

$$\frac{dq}{dt} = k_{ad}\,(C_0 - \frac{q}{V})(q_e - q) - k_d q \qquad 3.35$$

$$\frac{dq}{dt} = k_{ad}\,C_0 q_e\left[1 + \left(-\frac{1}{q_e} - \frac{1}{C_0V} - \frac{kd}{C_0 q_e k_{ad}}\right)q + \frac{q^2}{C_0 V q_e}\right] \qquad 3.36$$

Since $C_0V \gg q_e$, so $\frac{q^2}{C_0Vq_e} \ll (\frac{q}{q_e})^2$

Therefore the third term inside the bracket is in the order of $(q/q_e)^2$. It is much smaller than the second term, which is in the order of (q/q_e), when $q/q_e \ll 1$.

Ignoring the third term inside the bracket gives

$$\frac{dq}{dt} = k_{ad}\,C_0 q_e\left[1 + \left(-\frac{1}{q_e} - \frac{1}{C_0V} - \frac{kd}{C_0 q_e k_{ad}}\right)q\right] \qquad 3.37$$

By definition of

$$x = -\left(\frac{1}{q_e} + \frac{1}{C_0V} + \frac{kd}{C_0 q_e k_{ad}}\right)q \qquad 3.38$$

Inserting equation 3.38 into equation 3.37 gives

$$\frac{d\theta}{dt} = k_{ad}\,C(1 + x) \qquad 3.39$$

For small values of x ($q \ll q_e$), we have the following mathmatical approximation:

$$e^x = 1 + x \qquad 3.40$$

Replacing 1+ x in equation 3.39 using above approximation gives

$$\frac{dq}{dt} = k_{ad}\,C_0 q_e e^x \qquad 3.41$$

Inserting equation 3.38 into equation 3.41 gives

$$\frac{dq}{dt} = k_{ad}C_0q_e e^{-\left(\frac{1}{q_e}+\frac{1}{C_0V}+\frac{kd}{C_0q_ek_{ad}}\right)q} \tag*{3.42}$$

By definition of

$$\alpha = k_{ad}C_0q_e \tag*{3.43}$$

$$\beta = \left(\frac{1}{q_e} + \frac{1}{C_0V} + \frac{kd}{C_0q_ek_{ad}}\right) \tag*{3.44}$$

And substitution of equation 3.43 and 3.44 into equation 3.42, we have

$$\frac{dq}{dt} = \alpha e^{-\beta q} \tag*{3.45}$$

Which is the form of commonly called Elovich equation.

To solve and simplify Elovich equation, Chien and Clayton assumed [21] that $\alpha\beta t \gg 1$ and by applying the boundary conditions of q=0 at t=0 and q=q at t=t, then the solution of equation 3.45 is:

$$q = \left(\frac{1}{\beta}\right) lnt + \left(\frac{1}{\beta}\right) ln(\alpha\beta) \tag*{3.46}$$

3.2.2 Materials

Lead nitrate (BDH chemicals, Canada) and copper sulfate (Scientific Company, Canada, 99%) were used as received without further purification. Commercial potassium amyl xanthate (Prospec Chemicals Ltd, Canada) was purified by following method: 100 g xanthate was added to 1000 ml of warm acetone (40°C) on a water bath and stirred for a few minutes. The solution was then filtered through a hot water funnel and discarded [22]. Nitric acid (Fisher Scientific Company, Canada, 99%) and sodium hydroxide (Fisher Scientific Company, Canada, 99%) were used to adjust solution pH. All solutions used in experiments were prepared using Milli-Q water (Millipore deionized, >18.2 MΩcm, 0.22-µm-filtered) and then filtered by 0.2 µm filter after complete mixing. All tests using QCM-D were conducted under room temperature of 22 °C.

3.2.3 Quartz Crystal Microbalance with Dissipation (QCM-D)

The activation kinetics of zinc sulfide was investigated using a QCM-D (Q-sense E4, Q-sense AB, Gothenburg, Sweden) with the capacity of measuring changes in resonance frequency (Δ*f*) and energy dissipation (ΔD) of QCM-D sensors at 8 different harmonics simultaneously. For the sake of simplicity, only three harmonics (n = 3, 5 and 7) are shown in the results. The data were collected by the Q-sense Qsoft 401. The AT-cut quartz crystal with zinc sulfide coating on the top was purchased from Q-sense.

A quartz crystal sensor is a thin piezoelectric plate with gold electrodes on each side. When a mass is added to the sensor, its resonance frequency will decrease due to the piezoelectric effect of quartz. After the experiment, data modeling and analysis were carried out with Q-sense Qtools 3.0, in which Viscoelastic model was chosen to convert frequency change to mass change.

Prior to each experiment, the quartz crystal sensor with zinc sulfide coating (referred to as ZnS sensor hereafter) was cleaned as follows: soaked in hydrochloride acid solution (0.01 M) and sonicated for 5 minutes, followed by thorough rinsing with Milli-Q water. For a typical QCM-D experiment, a cleaned ZnS sensor was inserted into flow module with the ZnS surface facing testing solution. The flow module was then mounted on the Q-sense E4 chamber platform. Milli-Q water at same pH of the testing solution was pumped into the flow module by an IPC-N peristaltic pump (Ismatec, Switzerland) at a flow rate of 0.15 ml/min. For each measurement, a stable baseline (with frequency variation less than 1 Hz for at least 10 minutes) was first achieved using Milli-Q water and then followed by injection of testing solution. Subsequent xanthate adsorption test was performed by injecting potassium amyl xanthate solution of 5×10^{-5} M into the flow module at 0.15 ml/min.

3.3. Results and discussions

3.3.1 Activation kinetics

3.3.1.1 Copper

Copper sulfate solution with concentration 10^{-4} M was adjusted to pH 6.5 by titration with sodium hydroxide. At pH 6.5, no precipitate was observed in the duration of QCM-D measurement. The solution was pumped into the flow module of QCM-D with ZnS sensor mounted right after the pH adjustment. A negative frequency change was observed, which was accompanied by dissipation increase as shown in Figure 3.1. When the frequency curve reached a plateau, pump was stopped and the flow module was rinsed with Milli-Q water at pH 6.5 to remove all ions that were not bonded onto the sensor surface. The negative frequency shift in Figure 3.1, due to decrease of the crystal's resonance frequency of oscillation, indicates a mass increase of the sensor. The spreading of different overtones (3, 5 and 7) implies that the adsorbed film is not thin or rigid. The mass increase of ZnS sensor is believed to be due to the adsorption of hydrolysis species in the copper sulfate solution.

The species distribution diagram (Figure 3.2) illustrates that the species in copper sulfate solution are Cu^{2+}, $Cu(OH)^{+}$, $Cu(OH)_{2(aq)}$ and $Cu(OH)_{2(s)}$ at pH 6.5. Previous QCM-D measurement studies showed that ZnS activation by Cu^{2+} could not cause significant frequency shift because the mass change due to substitution of Zn atom (molecular weight: 65) by Cu atom (molecular weight: 64) was negligible (result not shown here). Therefore, the main species contributing to the frequency drop observed in Figure 3.1 are considered to be $Cu(OH)^{+}$, $Cu(OH)_{2(aq)}$ and $Cu(OH)_{2(s)}$. The adsorption of $Cu(OH)^{+}$ on sphalerite surface causing surface charge reversal has also been shown by zeta potential measurements at pH 6 to 7 [2, 3, 23].

The frequency shift was converted to mass change using Viscoelastic model (Voigt) of Q-sense Qtools, as shown in Figure 3.3 (a). The substantial mass increase clearly denies the possibility of equation 3.3 as the activation mechanism under neutral to alkaline condition, whereby the mass of solid phase will not change significantly in despite of copper uptake. The fittings of adsorption kinetics using three models, Pseudo-first order (equation 3.21), Pseudo-second order (equation 3.24) and Elovich model (equation 3.46), are presented in Figure 3.3. Table 3.1 lists the fitting parameters. Clearly, the Pseudo-second order gives the best fitting among three models, indicating that the adsorption of copper hydrolysis products on zinc sulfide surface follows second order kinetics which has been widely reported to describe the adsorption of copper and lead on various substrates [24, 25]. The second order adsorption implies that rate determining step is chemical sorption or chemisorption involving valence forces through sharing or exchange of electrons between sorbent and adsorbent [26]. Different from previous works on zinc sulfide activation that characterized the uptake of activators (Cu or Pb) under neutral to alkaline condition as two or more stages that were fitted with logarithmic or parabolic laws [7, 16], this *in-situ* activation study with high precision in both time and mass for the first time reports that the zinc sulfide activation with copper at neutral follows pseudo second order kinetics. The absence of a diffusion-controlled stage observed by Teng et al. [19] in Figure 3.3 is probably due to the fact that the ion exchange of Cu^{2+} and Zn^{2+} followed by diffusion of Cu^{2+} through ZnS coating layer does not contribute to the mass increase.

At pH 9, large amount of copper hydroxide precipitated in the solution and aggregated to form big flocs. The formation of flocs can easily block the pipe used to pump solution to the QCM-D chamber, as a result of which the attempts at investigating the zinc sulfide activation with copper at pH 9 have proved unsuccessful.

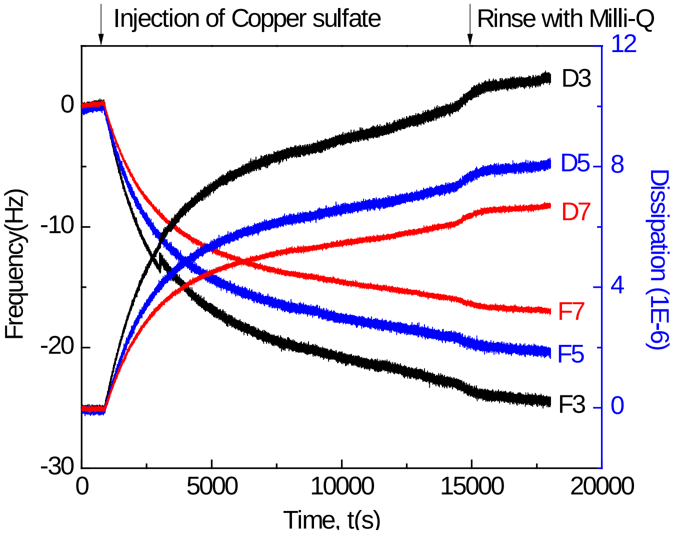

Figure 3.1 Frequency and dissipation shifts with time during the QCM-D measurement of ZnS activation by copper. A baseline with Milli-Q water (pH=6.5) was stabilized at first 14 minutes, and copper sulfate solution (pH=6.5) with concentration of 10^{-4} M was pumped into the chamber at a flow rate of 0.15 ml/min. Data at multiple overtones (n=3, 5 and 7) are presented to show the

dependence of frequency on overtones, indicating the characteristic of a viscoelastic layer.

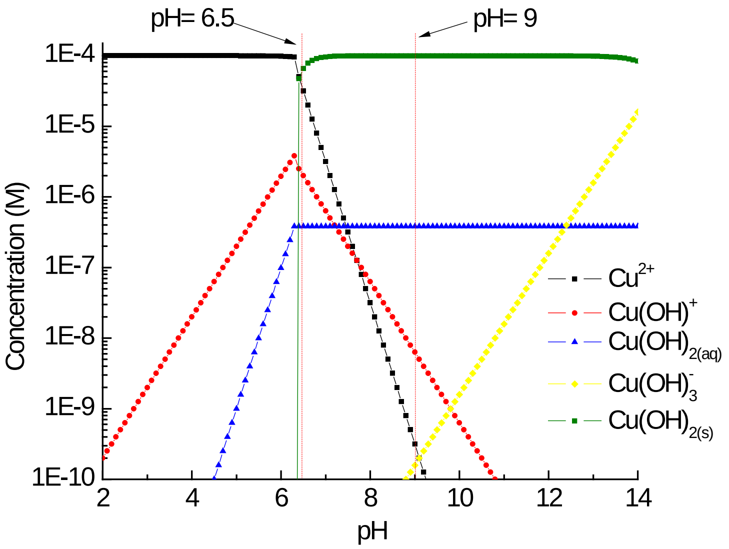

Figure 3.2 Cu speciation distribution diagram ($[Cu]^{2+}_{\text{Initial}}$ =10^{-4}M)

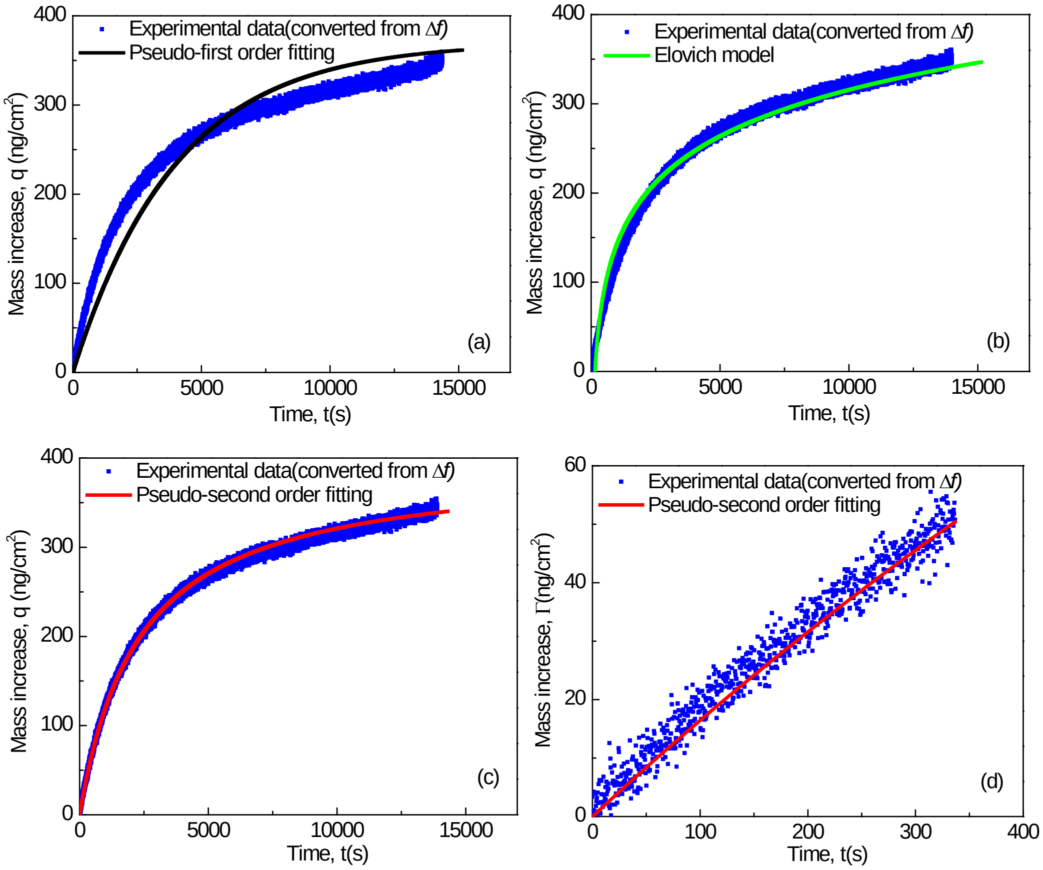

Figure 3.3 Kinetics models fitting of the real-time mass increase of ZnS sensor activated by 10^{-4}M copper sulfate at pH 6.5. (a) Pseudo-first order fitting of the

activation kinetics; (b) Elovich model fitting of the activation kinetics; (c) Pseudo-second order fitting of the activation kinetics; (d) Pseudo-second order fitting for the initial 5 mins.

3.3.1.2 Lead

Figure 3.4 shows the frequency and dissipation shifts upon injection of lead nitrate solution with concentration 10^{-4} M at pH 6.5 into QCM-D chamber with ZnS sensor mounted. The frequency drop and relatively large dissipation increase ($\Delta D/\Delta f > 2\times10^{-7}$) indicate the adsorption of a viscoelastic layer of lead hydrolysis species that are Pb^{2+} and $Pb(OH)^{+}$ as indicated by the species distribution diagram in Figure 3.5. Same as activation with copper at pH 6.5, pseudo-second order model gives the best fitting, which implies that the mechanism of activation with copper and lead at this pH may be the same.

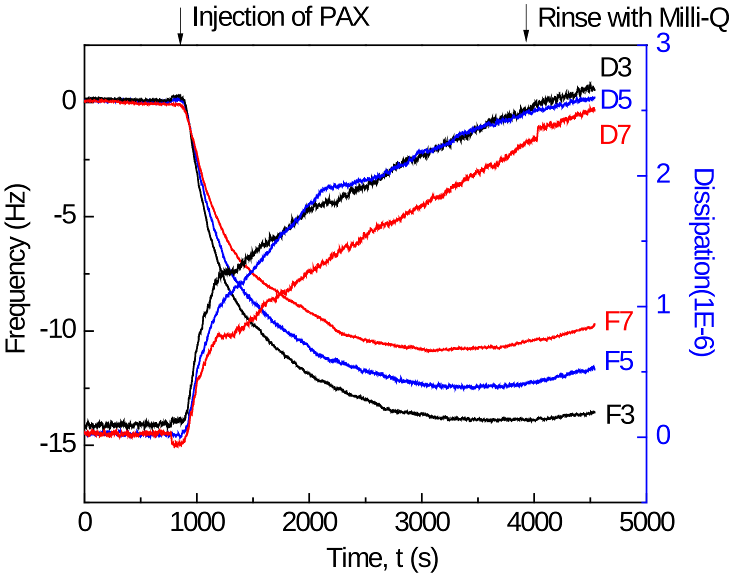

Figure 3.4 Frequency and dissipation shifts with time during the QCM-D measurement of ZnS activation by lead. A baseline with Milli-Q water (pH=6.5) was stabilized at first 15 minutes, and lead nitrate solution (pH=6.5) with concentration of 10^{-4} M was pumped into the chamber at a flow rate of 0.15 ml/min. Data at multiple overtones (n=3, 5 and 7) are presented to show the dependence of frequency on overtones, indicating the characteristic of a viscoelastic layer.

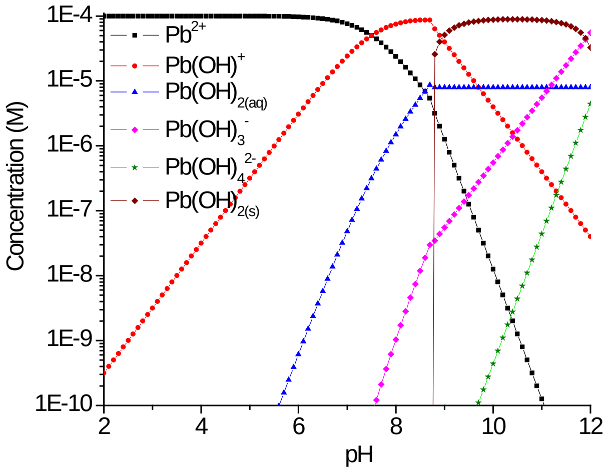

Figure 3.5 Pb speciation distribution diagram ($[Pb]^{2+}_{\text{Initial}}$ =10^{-4}M)

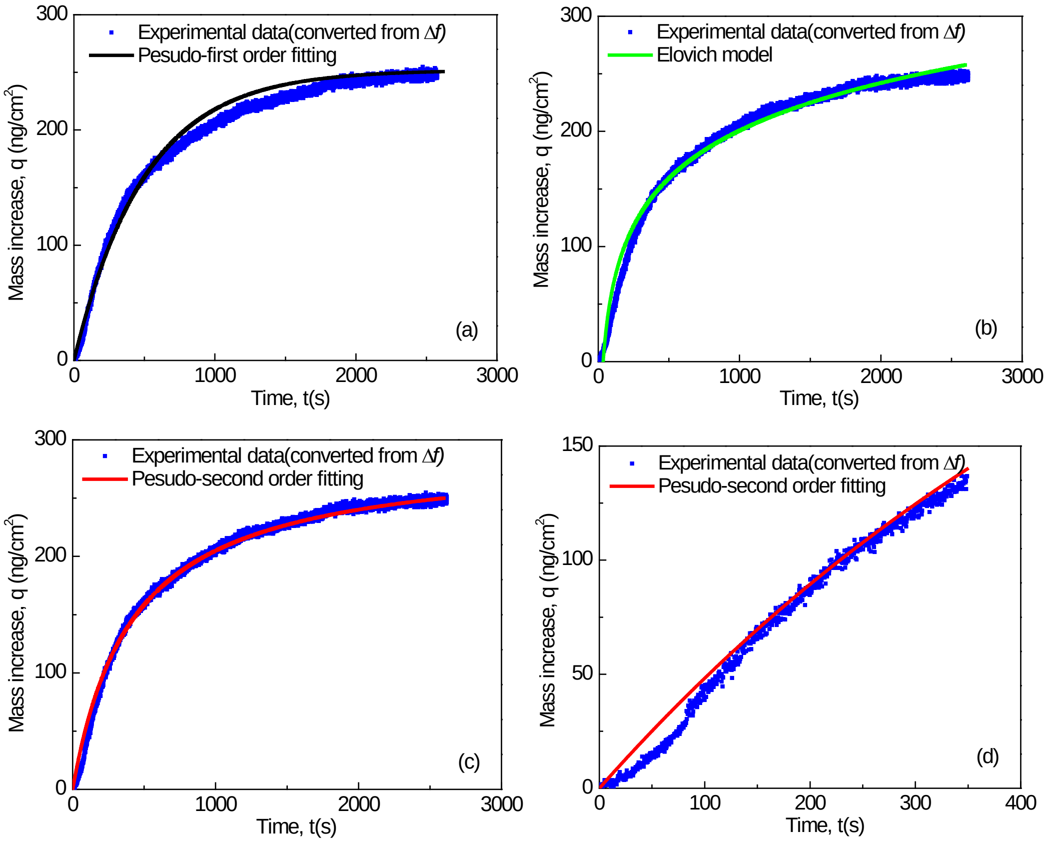

Figure 3.6 Kinetic models fitting of the real-time mass increase of ZnS sensor activated by 10^{-4}M lead nitrate at pH 6.5. (a)Pseudo-first order fitting of the activation kinetic; (b) Elovich model fitting of the activation kinetic; (c) Pseudo-second order fitting of the activation kinetic; (d) Pseudo-second order fitting for the initial 5 mins.

Different from copper, lead hydroxide precipitate in 10^{-4} M lead nitrate solution at pH 9 did not aggregate to form flocs. The solution was a stable suspension without obvious settling in the duration of QCM-D measurement. The result of zinc sulfide activation with lead at pH 9 is shown in Figure 3.7. Upon injection of lead nitrate solution, a sharp frequency drop by 20 Hz was observed in the first 5 minutes. Thereafter the frequency continued to drop at a decreasing rate. After rinsing with Milli-Q water at pH 9, about one quarter of the adsorbed material was rinsed away, indicating a relatively weak bonding between adsorbed layer and ZnS sensor surface. The overtone dependence of frequency drop and large dissipation ($\Delta D/\Delta f > 10^{-7}$) indicate that the adsorbed lead hydrolysis products form a viscoelastic layer on ZnS sensor surface.

As shown in Figure 3.8 and Table 3.1, Elovich model gives the best fitting for the mass increase of ZnS sensor caused by the adsorption of lead hydrolysis species at pH 9. However, the inset in Figure 3.8(b) indicates that Elovich model fails to fit the initial 200-300s (about 5 mins), which corresponds to the sharp frequency drop of 20 Hz in Figure 3.7. The kinetics of initial 5 min was analysed separately by pseudo-first order, pseudo-second order and Elovich model. The rate constants and their correlation coefficients are given in Table 3.1, respectively. Clearly, pseudo-first order gives a better fitting than the other two models.

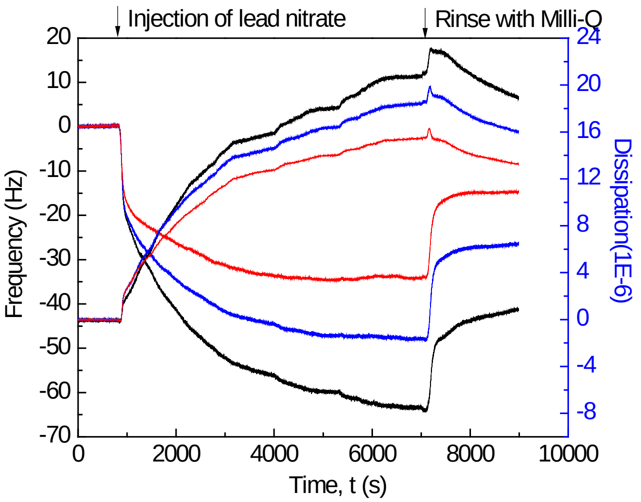

Figure 3.7 Frequency and dissipation shifts with time during the QCM-D measurement of ZnS activation by lead. A baseline with Milli-Q water (pH= 9)

was stabilized at first 15 minutes, and lead nitrate solution (pH= 9) with concentration of 10^{-4} M was pumped into the chamber at a flow rate of 0.15 ml/min. Data at multiple overtones (n=3, 5 and 7) are presented to show the dependence of frequency on overtones, indicating the characteristic of a viscoelastic layer.

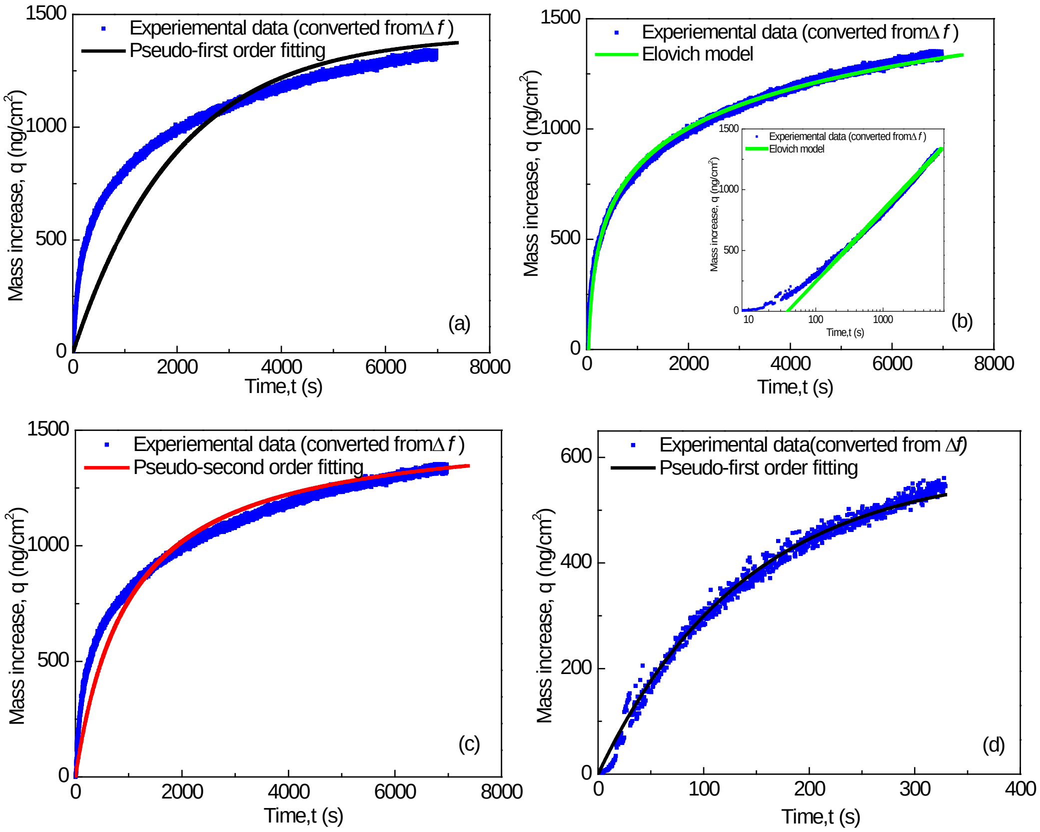

Figure 3.8 Kinetic models fitting of the real-time mass increase of ZnS sensor activated by 10^{-4}M lead nitrate at pH 9. (a) Pseudo-first order fitting of the activation kinetic; (b) Elovich model fitting of the activation kinetic. Inset shows the semi-log plot of the fitting; (c) Pseudo-second order fitting of the activation kinetic; (d) Pseudo-first order fitting for the initial 5 mins.

Table 3.1 Fitting parameters and correlation coefficients for the fitting of zinc sulfide activation kinetics using three kinetic models

Activator	pH	Pseudo-first order			Pseudo-second order			Elovich model		
		k_1 (s^{-1})	q_e (ng/cm^2)	R^2	k_2 (cm^{2}ng^{-1}s^{-1})	q_e (ng/cm^2)	R^2	α	β	R^2
Cu	6.5	2.5×10^{-4}	370	0.9196	1.1×10^{-6}	395	0.9938	0.5087	0.0133	0.9722
Pb	6.5	0.0020	252	0.9803	8.3×10^{-6}	280	0.9944	1.7221	0.0167	0.9745
Pb	9.0	0.0005	1410	0.7301	6.5×10^{-7}	1530	0.9520	0.6689	0.0039	0.9931
Initial stage		0.0069	595	0.9920	6.4×10^{-6}	845	0.9914	0.0056	10.4444	0.9767

To extract more information of the structure change of the adsorbed layer during activation, the ΔD versus Δ*f* was plotted in Figure 3.9, in which only the values of the fifth overtone were shown. For activation with copper at pH 6.5, the slope of ΔD-Δ*f* is almost constant, indicating no structure change during adsorption of hydrolysis products. On ΔD-Δ*f* plot of activation with lead at pH 6.5, there is a slight decrease in slope, which suggests that the adsorbed layer becomes more rigid due to rearranging of adsorbed molecules as activation process continues. Two straight lines are observed on ΔD-Δ*f* plot of activation with lead at pH 9. The slope of the first straight line is smaller than that of second line, implying that there is a significant structure change as adsorption process proceeds. The transition point of structure change (~20 Hz) is same as that between pseudo first order and Elovich model fitting.

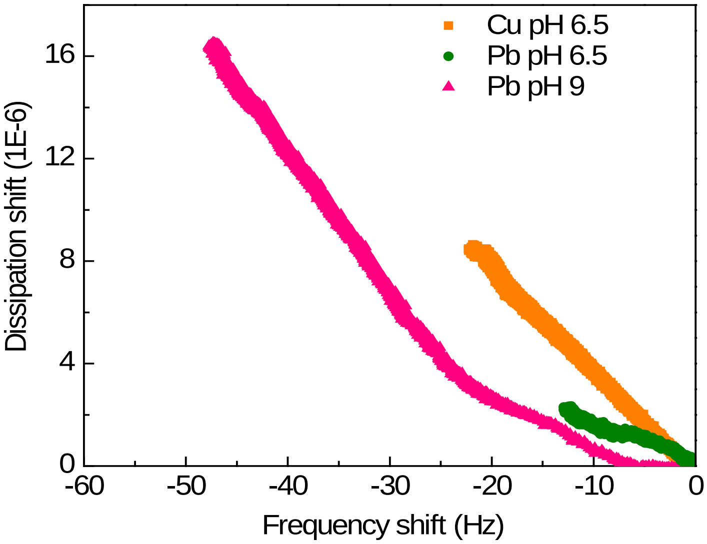

Figure 3.9 ΔD-Δ*f* (*n*=5) plot of Figure 3.1, 3.4 and 3.7.

3.3.2 Kinetics of xanthate adsorption

After each QCM-D measurement of activation, the ZnS sensor was taken out from the flow module and rinsed with Milli-Q water at same pH with the testing solution gently. The flow module was soaked in Milli-Q water and sonicated for 30 minutes, followed by thorough rinsing with Milli-Q water. The activated ZnS sensor was re-mounted on cleaned flow module for xanthate adsorption measurement. After stabilizing baseline with Milli-Q water, potassium amyl xanthate (PAX) solution with a concentration of 5×10^{-5}M at same pH with the activator solution was pumped into the flow module, and the frequency and dissipation shifts were monitored by Q-soft 401.

The results of PAX adsorption on copper and lead activated ZnS sensors are given in Figure 3.10. For all three tests, an initial frequency drop was observed in the first minute, followed by continuous drop at a decreasing rate. Kinetics fitting showed that two stages of PAX adsorption existed: a fast initial adsorption process taking about 1 min that was best fitted with pseudo-first order model, and a slower process that was best fitted with pseudo-second order. The fitting parameters and correlation coefficients are given in Table 3.2, and the best fittings for each stage are shown in Figure 3.11, 3.12 and 3.13.

Considering many laboratory and plant practices where the conditioning times for xanthate collector are only up to a few minutes, the rapid adsorption of PAX within first minute observed in Figure 3.10-3.13 may provide adequate hydrophobicity for bubble attachment, although the PAX adsorption continues for much longer time. The existence of two kinetics stages implies two different adsorption mechanisms.

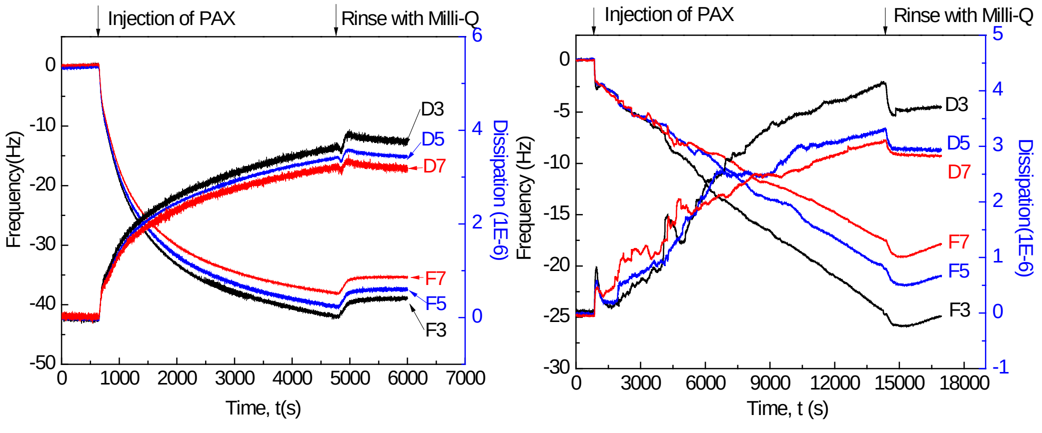

(a) (b)

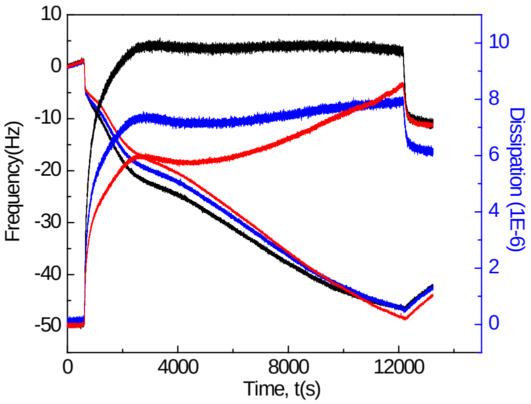

(c)

Figure 3.10 QCM-D monitoring of potassium amyl xanthate (PAX) adsorption on copper and lead activated ZnS sensor surfaces. (a) The frequency and dissipation shifts of activated ZnS sensor by copper at pH 6.5 upon injection of 5×10^{-5}M PAX solution at pH 6.5; (b) The frequency and dissipation shifts of activated ZnS sensor by lead at pH 6.5 upon injection of 5×10^{-5}M PAX solution at pH 6.5; (c) The frequency and dissipation shifts of activated ZnS sensor by lead at pH 9 upon injection of 5×10^{-5}M PAX solution at pH 9.

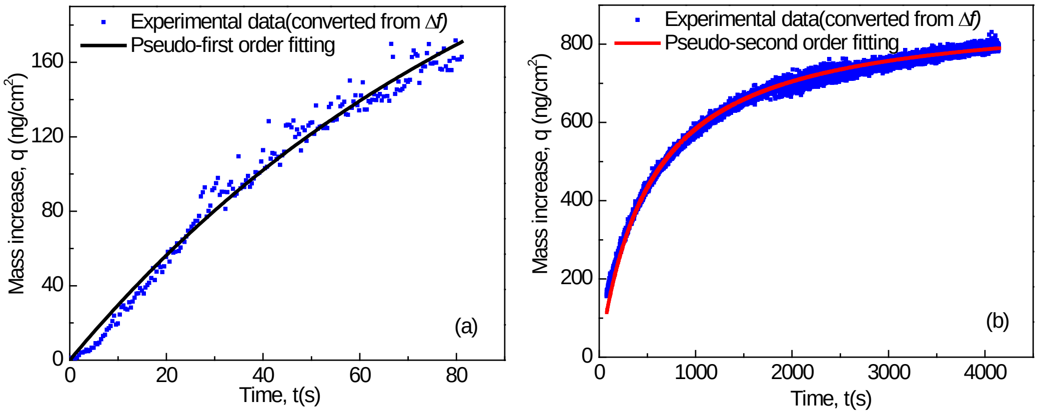

Figure 3.11 The best kinetics fitting for PAX adsorption on copper activated ZnS sensor at pH 6.5. (a) Pseudo-first order fitting for the initial rapid stage; (b) Pseudo-second order fitting for second stage.

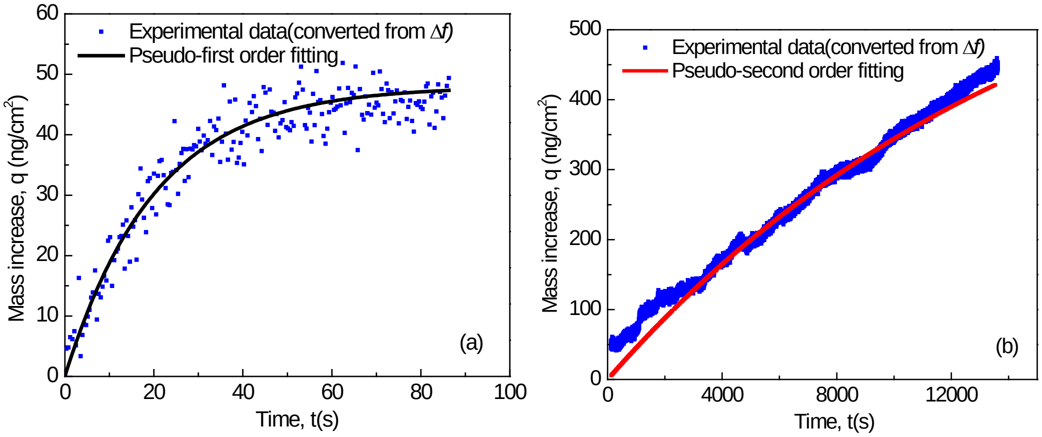

Figure 3.12 The best kinetics fitting for PAX adsorption on lead activated ZnS sensor at pH 6.5. (a) Pseudo-first order fitting for the initial rapid stage; (b) Pseudo-second order fitting for second stage.

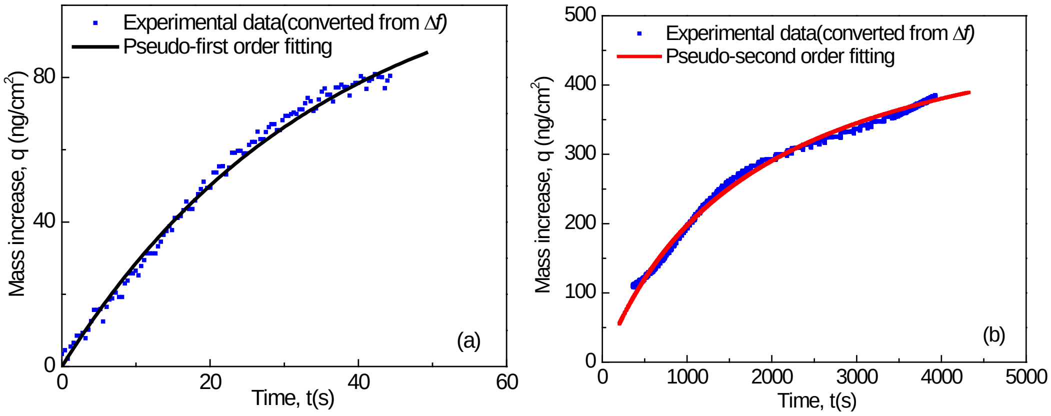

Figure 3.13 The best kinetics fitting for PAX adsorption on lead activated ZnS sensor at pH 9. (a) Pseudo-first order fitting for the initial rapid stage; (b) Pseudo-second order fitting for second stage.

Table 3.2 Fitting parameters and correlation coefficients of pseudo-first order, pseudo-second order and Elovich model fittings for PAX adsorption kinetics

System	pH	Stage	Pseudo-first order			Pseudo-second order			Elovich model		
			k_1 (s^{-1})	q_e (ng/cm^2)	R^2	k_2 ($cm^2ng^{-1}s^{-1}$)	q_e (ng/cm^2)	R^2	α	β	R^2
PAX on Cu activated ZnS	6.5	Initial	0.0104	300	0.9822	7.20×10^{-5}	260	0.9488	9.3632	0.0164	0.9395
		Later	0.0011	820	0.9137	2.14×10^{-6}	890	0.9940	5.4406	6.11×10^{-3}	0.9791
PAX on Pb activated ZnS	6.5	Initial	0.0466	48	0.9283	1.20×10^{-3}	55	0.9163	5.3962	0.0622	0.9101
		Later	6.50×10^{-5}	720	0.9760	1.30×10^{-7}	710	0.9814	0.2048	9.2×10^{-3}	0.8187
PAX on Pb activated ZnS	9.0	Initial	0.0286	115	0.9917	3.00×10^{-3}	130	0.9446	8.4426	0.0307	0.9633
		Later	6.85×10^{-4}	400	0.9890	1.02×10^{-6}	550	0.9904	1.1580	0.0109	0.8842

3.3.3 Activation mechanism discussion

The kinetics of zinc sulfide activation with copper and lead at pH 6.5 and 9 was invetigated with a QCM-D in the present study. The mjaor findings are summarized as follows:

1) After the activation, adsorbed copper and lead species on ZnS sensor surface could not be rinsed away easily, indicating the adsorption is irreversible at neutral and alkaline pH.
2) Large dissipation drop ($\Delta D/\Delta f > 2\times10^{-7}$) implies that the adsorbed layer of metal species is “soft” at pH 6.5 and 9.
3) For activation at pH 6.5, the activation kinetics could be fitted with pseudo second order model.. For activation at pH 9, the initial rapid stage was fitted with pseudo first order model and second stage was fitted Elovich model. As most studies suggest, psudo second order and Elovich model fitting are the characteristic of chemisorption.
4) At pH 6.5 the slope of ΔD vs. Δf plot was a constant for activation with copper and gradually decreased for activation with lead. At pH 9 two straight lines were observed on ΔD vs. Δf plot with the transition point at ~20Hz, which correspondes to the transition between the fitting of pseudo first order and Elovich model.
5) The uptake rate of lead at pH 6.5 was larger than that of copper (k_2(Pb)> k_2(Cu)). The equilibrium adsorption amount of lead at pH 9 was larger than that at pH 6.5.

Based on above findings, the zinc sulfide actiavtion with copper and lead at neutral pH should be the adsorption of hydrolysis products rather than ion exchange mechanism that dominates at acidic pH. During the adsorption, new chemical bonds between activator species and avaiable surface sites are formed. Since one pseudo second order model was used to fit the whole activation kinetics at pH 6.5, only one mechanism is considered to be involved in the course of activation experiment. The straight line in ΔD vs. Δf plot of activation with copper indicates that the adsorption occurs in 2-demension. Otherwise, the dissipitation shift per frequency drop will keep increasing due to the building up of later molecues on previously adsorbed ones. The decreasing slope of ΔD vs. Δf plot of activation with lead implies that the adsorbed molecues contract to the zinc sulfide surface as adsorption process goes on. Different from activation at pH 6.5, the lead activation kinetics at pH 9 was fitted with two models: a initial rapid stage fitted with pseudo first oder and a slower stage fitted with Elovich model. The difference may come from the activation species at neutral and alkaline pH. Rather than forming Pb^{2+} and $PbOH^{+}$ in lead nitrate solution at pH 6.5, the main species at pH 9 is $Pb(OH)_2$, which aggregates to form colloidal particles. So the frequency drop in Figure 3.7 is attributed to the adsorption of lead hydroxide particles, which leads to a much larger equilibrium adsorption amount of lead species at pH 9 than that at pH 6.5.

Considering the findings and direct or indirect inferences drawn, the authors agree on following activation mechanism.

At neutral pH

$$Zn - OH_{surface} + M(OH)^{+} \rightarrow Zn - O - M^{+}_{surface} + H_2O \qquad 3.47$$

Where each $M(OH)^{+}$ molecue is loosely surrounded by 3-5 water molecules, which results in large dissipation while $M(OH)^{+}$ adsorbs on zinc sulfide surface.

At alkaline pH

$$Zn - O^{-}{}_{surface} + M(OH)_2 \rightarrow Zn - O - M - O^{-}{}_{surface} + H_2O \qquad 3.48$$

Although $M(OH)_2$ is used to represent the one of the reactant in the formula, the actual activation species should be the clusters comprising of many $M(OH)_2$ molecules.

Further discussion on activation kinetic

Although the three kinetics models used in this study have been widely reported, the assumption of deriving the equation may not be valid in some circumstances. For instance, the adsorption rate for all three models is not always a constant during the whole adsorption process. Here we propose another model accounting for chemisorption on a molecular or atomic scale.

As shown in Figure 3.14, there are many vacant sites available for adsorption of solute from the solution phase initially. Due to van der Waals or electrostatic forces, the solute molecule is adsorbed close to the substrate surface, forming a physisorption layer. This process is very fast and diffusion-controlled. The molecue in physisorption layer can then jump onto vacant surface site to form a new chemical bond, and the position left by the molecue in physisorption layer can be quickly filled by another molecue from the solution. The adsorption is writted in the form of chemical reaction as shown in equation 3.49

$$A + * \leftrightarrow A* \qquad 3.49$$

Where A denotes one molecue and * is a vacant site, A* is the reaction product (occupied site).

On an average basis, the jumping rate (the number of molecues adsorbing onto one vacant site per unit time) or the rate of forming new chemical bond can be expressed in Arrhenius form [27-29].

$$r = Z\rho[A]\exp(\frac{-Ea}{RT}) \qquad 3.50$$

Where *r* is jumping rate, *Z* is collosion frequency, ρ is steric factor, [A] is the number of molecues that are close to the specific vacant site (based on collision theory, the molecues that are close to another reactant molecue have large probability to have successful collision) *Ea* is the energy barrier, *R* is gas constant and *T* is absolute temperature.

Given that the number of vacant sites at time *t* is n_v, the number of molecues adsorbed within time *dt* can be expressed as

$$dq = rn_v dt = n_v Z\rho[A]\,exp\left(\frac{-Ea}{RT}\right)dt \qquad 3.51$$

Where *q* is the number of molecues adsorbed at time t and dq is the number of adsorb molecues within time dt.

By moving *dt* to left hand side, equation 3.51 gives

$$\frac{dq}{dt} = rn_v = n_v Z\rho[A]\,exp(\frac{-Ea}{RT}) \qquad 3.52$$

By definition of

$$n_v = n_0 - n_a \qquad 3.53$$

Where n_0 is the initial number of vacant sites on substrate surface and n_a is the number of occupied surface sites at time t.

Inserting 3.53 into equation 3.52 gives

$$\frac{dq}{dt} = (n_0 - n_a)Z\rho[A]\exp(\frac{-Ea}{RT}) \qquad 3.54$$

Since the adsorbed amount is proportional to occupied sites on substract surface, so na can be writted as

$$n_a = \alpha q \qquad 3.55$$

Where α is a constant and have the physical meaning of the number of molecues adsorbing on each vacant site.

By inserting equation 3.55 into equation 3.54, equation 3.54 becomes

$$\frac{dq}{dt} = (n_0 - \alpha q)Z\rho[A]\, exp\left(\frac{-Ea}{RT}\right) = \left(\frac{n_0}{\alpha} - q\right)\alpha Z\rho[A]\, exp\left(\frac{-Ea}{RT}\right) \qquad 3.56$$

In equation 3.56, n_0, Z, ρ, R, α and T can be considered as constant in the duration of adsorption process. Only q and Ea are functions of t and q.

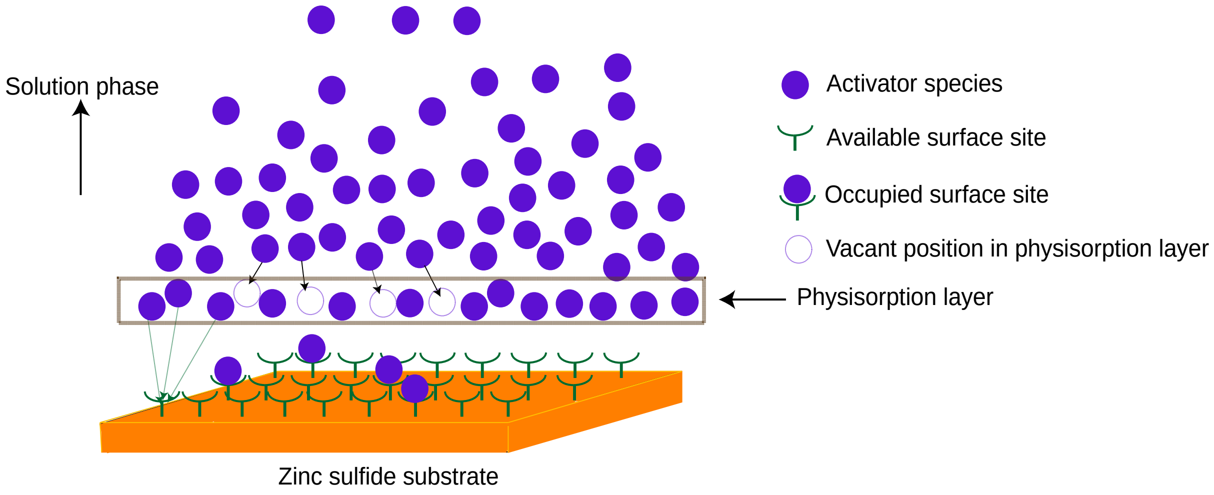

Figure 3.14 A schematic showing of proposed chemisorption process

Relation between [A] and adsorption kinetics

[A] is the number of molecues close to each vacant site, and it should be proportional to the concentration of the solute in physisorption layer, which is function of solute concentration and sign and size of surface charge of solute molecue and substrate surface. When the solution is dilute, [A] is expected to increase as solution concentration increases. Therefore, adsorption rate increases since it is proportional to [A] as shown in equation 3.56. When the solution is very concentrated, the solute in physisorption layer is “saturated”, the adsorption rate achieve maximum and will not increase as solution concentration increases.

Relation between Ea and kinetic model

Ea is the energy barrier for one molecue adsorbing onto one vacant site. If Ea is a constant in the adsorption process, which means that the adsorption behavior of solute molecue is independent of each other. In other word, the presence of adsorbent on occupied site of substrate surface does not alter the property of other vacant sites, and no charge transfer across the surface is expected to occur. In this case, $\alpha Z\rho[A]\exp\left(\frac{-Ea}{RT}\right)$ in equation 3.56 is a constant. By definition of

$$k = \alpha Z\rho[A]\exp\left(\frac{-Ea}{RT}\right) \qquad 3.57$$

Inserting 3.57 into 3.56 gives

$$\frac{dq}{dt} = k\left(\frac{n_0}{\alpha} - q\right) \qquad 3.58$$

Equation 3.58 is the form of Lagergren equation , which can be integrated to pseudo first order model.

In most cases, *Ea* is not a constant. It increases as adsorption process continues because the adsorption of solution molecue will affect state of neighboring vacant site due to either steric effect or charge transfer between surface sites. As a result of the increase of *Ea*, the adsorption rate will be decreased as compared to first order kinetic (constant *Ea*). If *Ea* and q have following relation

$$\frac{Ea}{RT} = -\kappa\, ln(q_e - q) \qquad 3.59$$

Where κ is a constant, q_e is the equilibrium adsorption amout and q_e-q is the driving force for adsorption. Interting equation 3.59 into equation 3.56 gives

$$\frac{dq}{dt} = \kappa\alpha Z\rho[A]\left(\frac{n_0}{\alpha} - q\right)(q_e - q) \qquad 3.60$$

Equation 3.60 can be easily rearranged to the form of equation 3.28, which is the integration form of pseudo second order model. Therefore, second order model actually is the simplied version of equation 3.56 with the relation of equation 3.59.

If $n_0/\alpha >> q$, meaning the number of adsorbed molecules is much smaller than the number of vacant site, and Ea is proportional to q.

$$Ea = \omega q \qquad 3.61$$

Where ω is a constant. Inserting equation 3.61 into equation 3.56 gives

$$\frac{dq}{dt} = n_0 Z\rho[A]\, exp\left(\frac{-\omega}{RT} q\right) \qquad 3.62$$

Since $n_0 Z\rho[A]$ is a constant, equation 3.62 can be rearranged to the form of equation 3.45, which is Elovich model.

From above disccusion, it can be seen that different kinetics models actually describe how Ea increases with q. Figure 3.15 shows the comparision of three kinetic models with the same intial adsorption rate. It can be seen that the adsorption rate of Elovich model is decreased the most, implying that Ea increases significantly as adsorption process goes on.

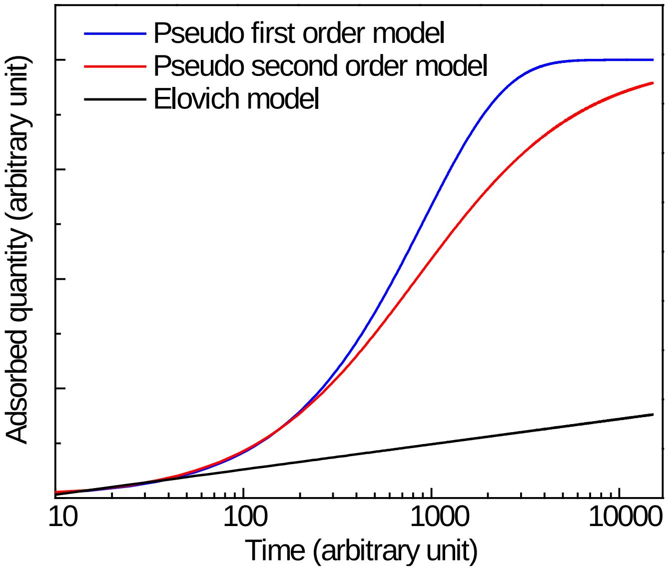

Figure 3.15 Comparision of three kinetic models with the same initial adsorption rate

Significance to understand activation kinetics

At pH 6.5, the kinetics of activation with copper and lead was fitted with pseudo second order model, which suggests that charge transfer across zinc sulfide surface occurs at the beginning of the adsorption process. At pH 9, pseudo first order model was used to fit the kinetic of the first stage activation with lead, indicating the *Ea* does not change in this case. It can be attributed to two scenarios: 1) it is physisorption that does not chang the *Ea*; 2) the adsorbed lead hydroxide particles are very far away from each other on zinc sulfide surface, and therefore the presence of adsorbed particles does not change the *Ea* of the adsorption on neibouring sites. In the second stage that was fitted with Elovich model, the adsorbed particles significantly inhibit the later adsorption of lead hydroxide particles probably due to steric effect.

3.4 Conclusions

The kinetics of zinc sulfide activation with copper and lead and xanthate adsorption were investigated with a quartz crystal microbalance with dissipation (QCM-D). Three kinetic models were used to fit the adsorption kinetics. The finding and conclusions are listed below:

1) Significant frequency drops were observed for QCM-D study of ZnS activation with copper and lead at pH 6.5 and 9. After rinsing with Milli-Q water, the frequency did not shift back to its value before addition of activator solution, implying the adsorption was irreversible. Subsequent potassium amyl xanthate (PAX) adsorption on activated ZnS sensor confirmed the successful activation.

2) For activation with copper at pH 6.5, the observed frequency drop was due to the adsorption of $Cu(OH)^+$ since activation with Cu^{2+} does not cause frequency drop. For activation with lead, the main activation species are Pb^{2+} and $Pb(OH)^+$ at pH 6.5 and $Pb(OH)^+$ and $Pb(OH)_2$ at pH 9.

2) For activation with either copper or lead at pH 6.5, pseudo-second order gave a better fitting, which suggests the activation is a chemisorption process . For activation with lead at pH 9, the adsorption of $Pb(OH)^+$ and $Pb(OH)_2$ was fitted with Elovich model.

3) The uptake of copper or lead species was dependent on pH. Alkaline pH was favourable for the uptake of lead. The uptake rate of lead is greater than that of copper at pH 6.5.

4) The uptake of xanthate on activated zinc sulfide was dependent on pH and activator. Two domains were indentified on the xanthate uptake of curve: a initial rapid domain fitted with pseudo-first order, then a slower domain following pseudo-second order kinetics. The maximum xanthate adsorption rate was found at pH 6.5 on lead activated zinc sulfide and copper activated zinc sulfide for initial and second domain, respectively.

3.5 References

[1] J. Steininger, Trans. AIME, 241 (1968) 34.
[2] S. Jain, D. Fuerstenau, Flotation of Sulphide Minerals, (1984) 159-174.
[3] J. Laskowski, Q. Liu, Y. Zhan, Minerals engineering, 10 (1997) 787-802.
[4] J. Girczys, J. Laskowski, J. Lekki, Canadian Metallurgical Quarterly, 11 (1972) 553-558.
[5] S.R. Popov, D.R. Vučinić, Colloids and Surfaces, 47 (1990) 81-94.
[6] R.O. James, T.W. Healy, Journal of Colloid and Interface Science, 40 (1972) 65-81.
[7] J. Ralston, T.W. Healy, International Journal of Mineral Processing, 7 (1980) 203-217.
[8] W. Trahar, G. Senior, G. Heyes, M. Creed, International Journal of Mineral Processing, 49 (1997) 121-148.
[9] F. Rashchi, C. Sui, J.A. Finch, International Journal of Mineral Processing, 67 (2002) 43-58.
[10] C. Basilio, I. Kartio, R.H. Yoon, Minerals engineering, 9 (1996) 869-879.
[11] A. Chandra, A. Gerson, Advances in colloid and interface science, 145 (2009) 97-110.
[12] R. Pattrick, J. Charnock, K. England, J. Mosselmans, K. Wright, Minerals engineering, 11 (1998) 1025-1033.

[13] M.S. Morey, S.R. Grano, J. Ralston, C.A. Prestidge, B. Verity, Minerals engineering, 14 (2001) 1009-1017.

[14] R. Houot, P. Raveneau, International Journal of Mineral Processing, 35 (1992) 253-271.

[15] C.A. Prestidge, W.M. Skinner, J. Ralston, R.S.C. Smart, Applied surface science, 108 (1997) 333-344.

[16] C. Sui, D. Lee, A. Casuge, J. Finch, Minerals and Metallurgical Processing(USA), 16 (1999) 53-61.

[17] D. Fuerstenau, P. Metzger, Trans. AIME, 217 (1960) 119.

[18] Q. Zhang, Z. Xu, J. Finch, Minerals engineering, 8 (1995) 999-1007.

[19] F. Teng, Q. Liu, H. Zeng, Journal of Colloid and Interface Science, accepted (2011).

[20] S. Azizian, Journal of Colloid and Interface Science, 276 (2004) 47-52.

[21] S. Chien, W. Clayton, Soil Science Society of America Journal, 44 (1980) 265-268.

[22] S.R. Rao, Xanthates and related compounds, M. Dekker, 1971.

[23] T. Healy, M. Moignard, Flotation--A. M. Gaudin Memorial, (1976).

[24] S. Quek, D. Wase, C. Forster, WATER SA, 24 (1998) 251-256.

[25] K. Periasamy, C. Namasivayam, Chemosphere, 32 (1996) 769-789.

[26] C. Namasivayam, K. Prathap, Colloids and Surfaces A: Physicochemical and Engineering Aspects, 295 (2007) 55-60.

[27] F.M. Zimmermann, X. Pan, Physical Review Letters, 85 (2000) 618-621.

[28] M. Balooch, M. Cardillo, D. Miller, R. Stickney, Surface Science, 46 (1974) 358-392.

[29] J.I. Steinfeld, J.S. Francisco, W.L. Hase, (1989).

Chapter 4 Effect of calcium sulfate on sphalerite flotation

4.1 Introduction

Froth flotation is a process for separating valuable minerals from gangues by taking advantage of difference in their hydrophobicity. More than one billion tons of sulfide ores is concentrated annually with this method [1]. Due to the huge volume of processed ores, froth flotation requires billion of gallons of water in the process. In order to reduce the supply of fresh water, a great percentage of process water needs to be recycled. The chemistry of recycled water is significantly different from fresh water due to the presence of residual chemical agents, cations of metals, anions of inorganic and organic pollutants and suspended particles [2]. In sulfide processing plants, calcium and sulfate ions are the most experienced ions in recycled water. At some mines, the concentration of calcium and sulfate can be as high as 3000 ppm. The Ca^{2+} ion mainly comes from dissolution of calcium-containing minerals [3] and the addition of lime as a pH modifier and pyrite depressant [4]. A high concentration of sulphate ions (SO_4^{2-}) is from either oxidization of sulphide or addition of zinc sulphate and copper sulphate as deactivator and activator in the case of sphalerite flotation [5]. Identifying the impact of calcium sulfate on sulfide flotation has been a difficult task as flotation is very complex and involves many physical or chemical processes.

Generally, the effect of calcium sulfate can be understood from three aspects: 1) calcium adsorption: The adsorption of calcium on sphalerite surface can make surface charge less negative, which in turn affects the interaction between sphalerite, gangues and chemical reagents; 2) Sphalerite surface induced crystallization of gypsum: the gypsum coating on sphalerite surface will hinder the activation and subsequent xanthate adsorption, leading to decreased recovery; 3) At high concentration of calcium and sulfate ions, the gypsum precipitate may heterocoagulate with sphalerite and other minerals: same as above, the presence of gypsum on sphalerite surface will affect the flotation of sphalerite. A number of studies carried out in the past deal with the general effect of calcium and sulfate on sphalerite flotation [6-9]. Little is generally known about the concentrated calcium sulfate solution on separate steps during sphalerite flotation since flotation of sphalerite is a complex process including activation, xanthate adsorption, bubble attachment etc. Calcium sulfate can affect any of these steps, resulting in depressed flotation.

In this study, a systematic investigation of calcium adsorption on sphalerite, surface induced gypsum crystallization and heterocoagulation is conducted using a quartz crystal microbalance with dissipation (QCM-D), micro-flotation, scanning electron microscope and theoretical calculation.

4.2 Materials and Experimental techniques

4.2.1 Materials

Calcium chloride and sodium sulfate solutions were prepared by dissolving $CaCl_2 \cdot 2H_2O$ (Fisher, 99.5%) and Na_2SO_4 (Fisher, 99%) in 18MΩcm Milli-Q water. Copper sulfate (Scientific Company, Canada, 99%) was used as received without further purification. A high purity sample of sphalerite was acquired from Ward's Natural Science. The sample was crushed, hand-sorted and dry screened to collect the three size fraction ~35-78μm, ~100μm and ~5μm. Commercial potassium amyl xanthate (Prospec Chemicals Ltd, Canada) was purified by following method: 100 g xanthate was added to 1000 ml of warm acetone (40°C) on a water bath and stirred for a few minutes. The solution was then filtered through a hot water funnel and discarded [10]. Nitric acid (Fisher Scientific Company, Canada, 99%) and sodium hydroxide (Fisher Scientific Company, Canada, 99%) were used to adjust solution pH. All solutions used in experiments were prepared using Milli-Q water (Millipore deionized, >18.2 MΩcm, 0.22-μm-filtered) and then filtered by 0.2 μm filter after complete mixing. All tests using QCM-D were conducted under room temperature of 22 °C.

4.2.2 Quartz crystal microbalance with dissipation (QCM-D)

The calcium adsorption and activation kinetics of zinc sulfide were investigated using a QCM-D (Q-sense E4, Q-sense AB, Gothenburg, Sweden) with the capacity of measuring changes in resonance frequency (Δf) and energy dissipation (ΔD) of QCM-D sensors at 8 different harmonics simultaneously. For the sake of simplicity, only three harmonics (n = 3, 5 and 7) are shown in the results. The data were collected by the Q-sense Qsoft 401. The AT-cut quartz crystal with zinc sulfide coating on the top surface was purchased from Q-sense. Prior to each experiment, the quartz crystal sensor with zinc sulfide coating (referred to as ZnS sensor hereafter) was cleaned as follows: soaked in hydrochloride acid solution (0.01 M) and sonicated for 5 minutes, followed by thorough rinsing with Milli-Q water. For a typical QCM-D experiment, a cleaned ZnS sensor was inserted into flow module with the ZnS surface facing testing solution. The flow module was then mounted on the Q-sense E4 chamber platform. Milli-Q water at same pH of the testing solution was pumped into the flow module by an IPC-N peristaltic pump (Ismatec, Switzerland) at a flow rate of 0.15 ml/min. For each measurement, a stable baseline (with frequency variation less than 1 Hz for at least 10 minutes) was first achieved using Milli-Q water and then followed by injection of testing solution.

4.2.3 Micro-flotation

Flotation tests were carried out with a modified Hallimond tube that is described by Francis and Liu [11]. Typically, 1.5g sphalerite particles were mixed with 150ml of 10^{-2} M NaCl solution. Copper sulfate was added as activator, followed by some amount of calcium chloride. pH was adjusted to desired value with sodium hydroxide (0.2M) and hydrochloric acid (0.2M) right after the addition of calcium chloride. The conditioning time with activators was set to be 10 min since longer conditioning time did not significantly increase the recovery of sphalerite [12]. After the addition of potassium amyl xanthate solution, the pulp was conditioned for 30s in the beaker and then transferred to the flotation tube. A controlled flow of nitrogen was used as flotation gas at 20~30ml/min and 25psig. The floating portion was collected after 5min. They were filtered and dried in oven to calculate the final recovery of sphalerite.

4.2.4 Scanning electron microscope

The scanning electron microscopy (SEM) measurement was carried out on a JAMP-9500F JEOL Auger micro-probe. The instrument was equipped with a Schottky field emitter. The accelerating voltage and emission current for SEM imaging were 25kV and 10nA, respectively. The sample was rotated 30° away from the primary electron beam to face the electron energy analyzer.

4.2.5 Contact angle

Static contact angles of water on sample surfaces were measured using a drop shape analyzer (DSA100, Krüss, Germany) equipped with an optical microscope and illumination system. The sessile drop method with drop volumes of 10-20 μL was employed at room temperature (21.0±0.5°C). Contact angle was measured within 5 sec after the water droplet was dropped onto a solid surface. The shape of the sessile drop was recorded and fitted by the computer to calculate the contact angle.

4.3 Results and discussions

4.3.1 Calcium adsorption

Upon pumping calcium chloride solution of 0.015 M (600ppm Ca) at pH 6.5 into the flow module with ZnS sensor mounted, a negative frequency change was observed, which was accompanied by dissipation increase as shown in Figure 4.1(a). When the frequency curve almost reached a plateau, pump was stopped and the flow module was rinsed with Milli-Q water at pH 6.5. The frequency value was observed to go up to zero, indicating the adsorbed calcium has been rinsed away. The reversible adsorption suggests that calcium is not chemically bonded to the zinc sulfide surface. The large dissipation ($\Delta D/\Delta f > 2\times10^{-7}$) indicates that calcium ions are loosely bound to the surface. The experiment was repeated using calcium chloride solution with same concentration at pH 10, and the result was similar to the one at pH 6.5 as shown in Figure 4.1(b).

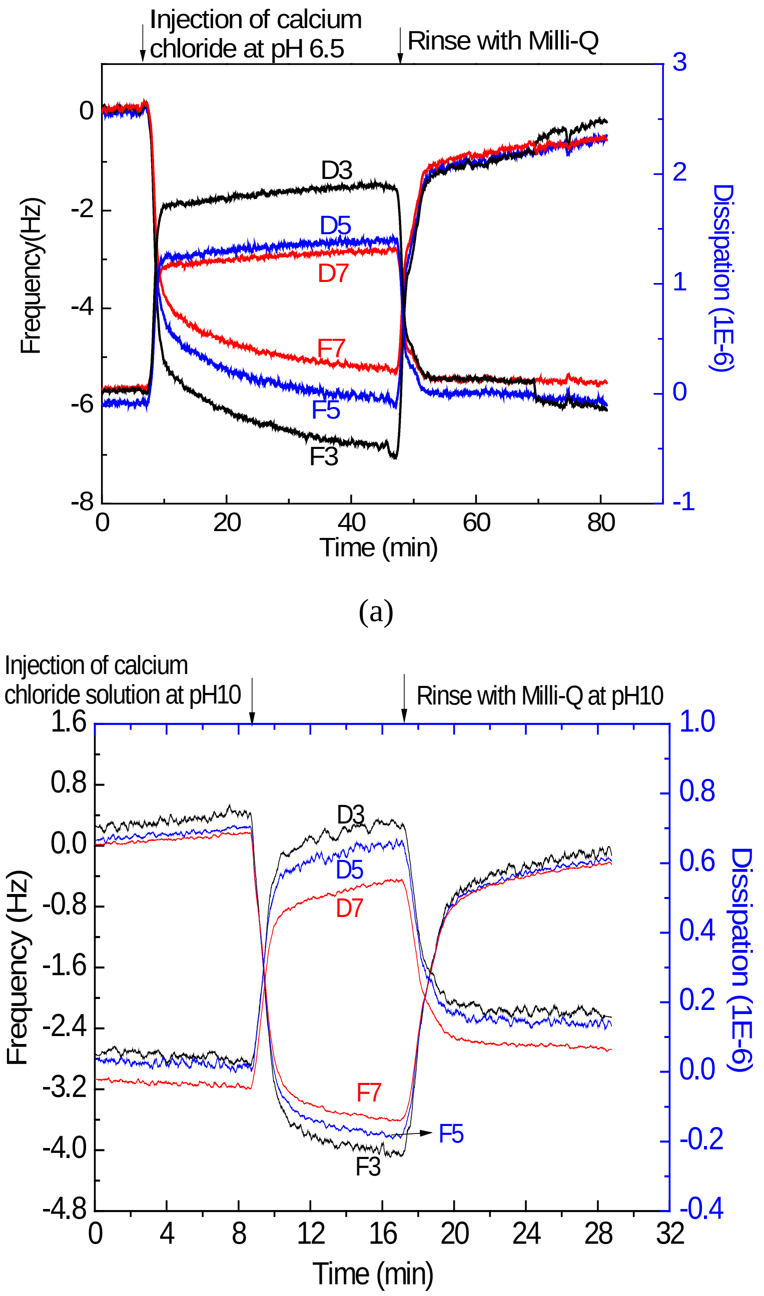

(a)

(b)

Figure 4.1 Frequency and dissipation changes with time during the QCM-D measurement on the adsorption of calcium on ZnS sensor. A baseline with Milli-Q water was stabilized at first 8 minutes, and calcium chloride solution with concentration of 0.015 M was pumped into the chamber at a flow rate of 0.15 ml/min. After the frequency drop reached a plateau, Milli-Q water was injected to rinse the ZnS sensor surface. Data at multiple overtones (n=3, 5 and 7) are presented to show the overlap of different overtones, which indicates the adsorbed layer is rigid and thin. (a) Calcium adsorption at pH 6.5; (b) Calcium adsorption at pH 10.

A micro-flotation test was carried out to investigate the effect of calcium on sphalerite flotation. The recovery of sphalerite in presence of calcium chloride solution with different concentrations at pH 10 is shown in Figure 4.2. It can be seen that there is no significant recovery change in the presence of calcium up to 2500 ppm. Given the fact that calcium is reversibly adsorbed onto zinc sulfide surface as indicated in Figure 4.1(b), the reason why no recovery change was observed is probably that copper and PAX have stronger interaction with zinc sulfide surface than calcium. In other word, even a layer of calcium is attracted to the surface, copper and PAX molecues can penetrate the calcium layer to form a chemical bond with zinc sulfide surface. Therefore, the flotation of sphalerite is not affected by the presence of calcium ions.

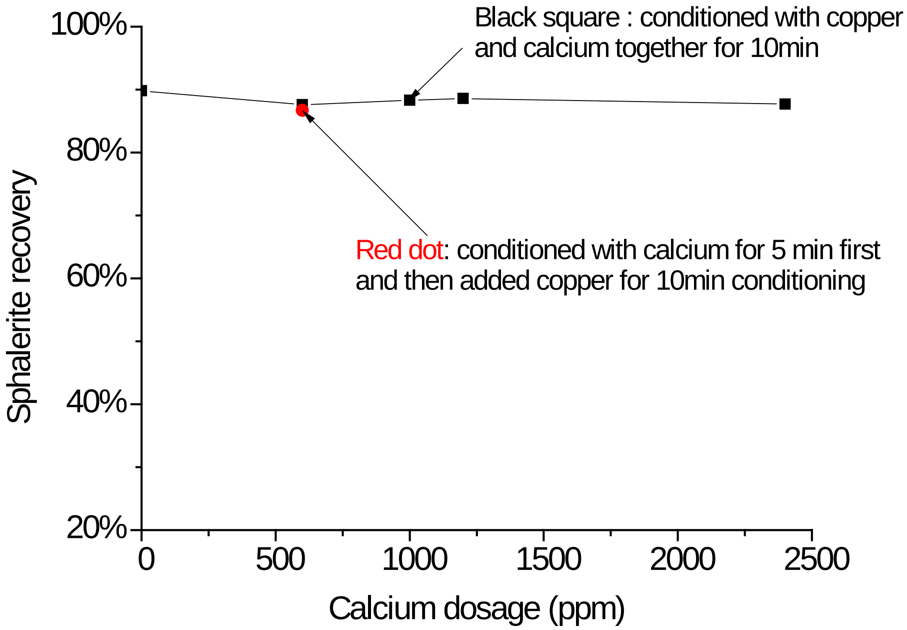

Figure 4.2 Recovery of sphalerite in the presence of calcium chloride solution at pH 10. Copper sulfate (10^{-3}M) was used activator. The concentration of potassium amyl xanthate (PAX) was 5×10^{-5}M. Conditioning time for copper and was set to be 10 minutes and 30 seconds, respectively.

4.3.2 Effect of calcium on zinc sulfide activation

The effect of calcium on zinc sulfide activation and xanthate adsorption was investigated with QCM-D, and the results are shown in Figure 4.3. Comparing Figure 4.3(a) and Figure 4.3(b), Figure 4.3(c), it can seen that the uptake of copper was significantly retarded with the presence of 600 ppm calcium. This result contradicts to the micro-flotation result which shows that the presence of calcium does not affect the recovery of sphalerite, although the pH and concentration of copper in two tests are different. A possible reason is that the flotation of sphalerite only requires very small amount of xanthate on the surface, and hence the retardation of xanthate adsorption in Figure 4.3(a) does not affect recovery of sphalerite.

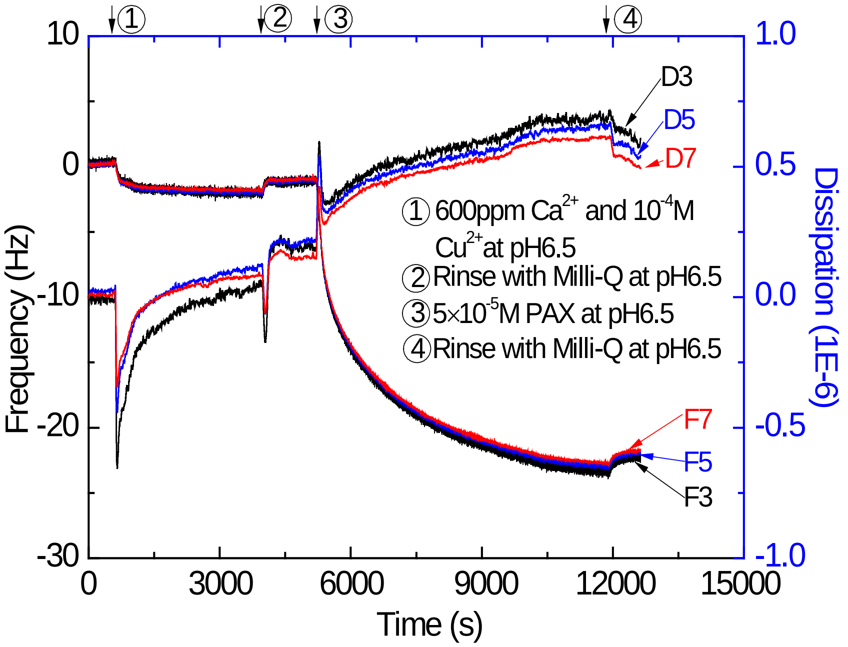

(a)

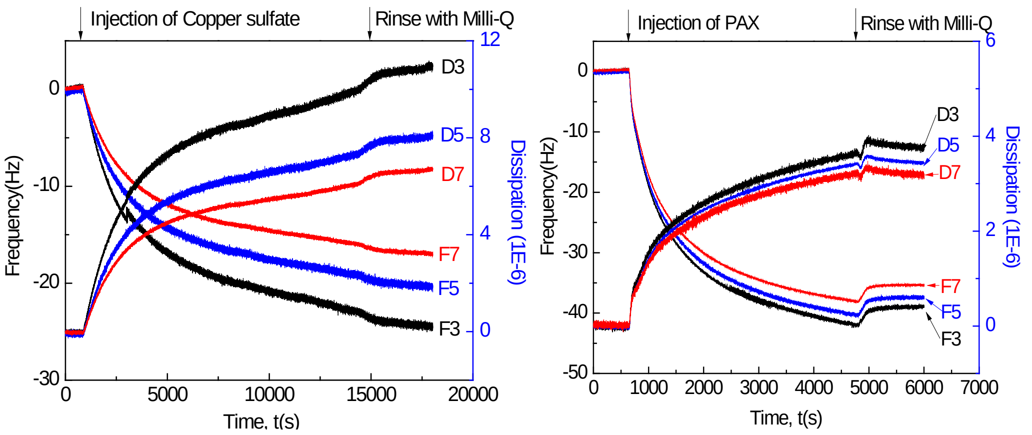

(b) (c)

Figure 4.3 Frequency and dissipation changes with time during the QCM-D measurement of zinc sulfide activation and xanthate adsorption. (a) Activation with copper and PAX adsorption in the presence of 600ppm calcium. The solution with 10^{-4}M copper sulfate and 600ppm calcium chloride at pH 6.5 was injected into QCM-D chamber with ZnS sensor mounted. After the frequency drop reached a plateau, Milli-Q water at pH 6.5 was pumped into the chamber to rinse the ZnS sensor. Finally, 5×10^{-5}M PAX solution at pH 6.5 was pumped into the chamber. (b) Activation with copper sulfate (10^{-4}M) at pH 6.5 without calcium (c) PAX adsorption after activated with copper at pH 6.5 without calcium

4.3.3 Surface energy calculation

For gypsum crystallization on zinc sulfide surface rather than in solution phase, the free energy is given by equation 4.1

$$\Delta G = \gamma_{ZnS-Gyp} - (\gamma_{ZnS-solution} + \gamma_{Gyp-solution}) \qquad 4.1$$

Where $\gamma_{ZnS-Gyp}$, $\gamma_{ZnS-solution}$ and $\gamma_{Gyp-solution}$ are expressed by equation 4.2, 4.3 and 4.4.

$$\gamma_{ZnS-Gyp} = (\sqrt{\gamma_{ZnS}^{LW}} - \sqrt{\gamma_{Gyp}^{LW}})^2 + 2(\sqrt{\gamma_{ZnS}^{+}\gamma_{ZnS}^{-}} + \sqrt{\gamma_{Gyp}^{+}\gamma_{Gyp}^{-}} - \sqrt{\gamma_{ZnS}^{+}\gamma_{Gyp}^{-}} - \sqrt{\gamma_{Gyp}^{+}\gamma_{ZnS}^{-}}) \qquad 4.2$$

$$\gamma_{ZnS-solution} = \gamma_{ZnS} - \gamma_{solution}\cos\theta_{ZnS} \qquad 4.3$$

$$\gamma_{Gyp-solution} = \gamma_{Gyp} - \gamma_{solution}\cos\theta_{Gyp} \qquad 4.4$$

In order to calculate ΔG in equation 4.1, the surface energies in equation 4.2-4.4 need to be known. A three-probing liquid method was carried out to calculate the surface energies of gypsum and zinc sulfide.

The surface energy of the cleaved surface of gypsum as the form of selenite, whose {010} plane is the particular crystallographic plane which can be cleaved by inserting razor blade parallel to {010} face, and ZnS sensor were derived using the sessile drop method based on the contact angles of the three probe liquids. Contact angles (θ) of the liquid droplets were measured on freshly cleaved gypsum surface and purged with nitrogen at room temperature and ambient humidity. Contact angles were measured within 5 sec after the droplet of probe liquid is dropped onto gypsum surfaces. The shape of the sessile drop was recorded and fitted by the computer and used to calculate the contact angle. The detailed three probe liquids method is shown below:

Surface energy γ, and the relative contributions to γ from Lifshitz–van der Waals (γ^{LW}) and Lewis acid base (γ^{AB}) components can be calculated by a method developed by van Oss *et al.* Surface tension can be given as

$$\gamma = \gamma^{\mathrm{LW}} + \gamma^{\mathrm{AB}}. \qquad 4.5$$

The AB component of the surface tension (γ^{AB}) is defined to comprise all electron-acceptor–electron-donor, or Lewis acid-base interactions, given by

$$\gamma^{\mathrm{AB}} = 2\sqrt{\gamma^{+}\gamma^{-}} \qquad 4.6$$

The LW, electron donor and electron acceptor components, γ^{LW}, γ^{-}, and γ^{+}, can be calculated from the contact angle measurement. When a drop of a liquid (L) is deposited on a solid surface (S), the contact angle between the drop and the surface (θ_L) is a function of the components and parameters of the surface tensions of the liquid (γ_L) and the solid (γ_S). The Young–Dupre equation describes the relations among these elements:

$$\gamma_{\mathrm{L}}(\cos\theta_{\mathrm{L}} + 1) = 2\sqrt{\gamma_{\mathrm{S}}^{\mathrm{LW}}\gamma_{\mathrm{L}}^{\mathrm{LW}}} + 2\sqrt{\gamma_{\mathrm{S}}^{+}\gamma_{\mathrm{L}}^{-}} + 2\sqrt{\gamma_{\mathrm{S}}^{-}\gamma_{\mathrm{L}}^{+}} \qquad 4.7$$

To solve the surface tension components of the solid, $\gamma_{\mathrm{S}}^{\mathrm{LW}}$, γ_{S}^{-}, and γ_{S}^{+}, three probe solutions must be used to yield three equations. Surface tension components for liquid, $\gamma_{\mathrm{L}}^{\mathrm{LW}}$, γ_{L}^{-}, and γ_{L}^{+}, are characteristic of the three probe liquids (i, ii, and iii); surface tensions of i, ii, and iii are designated $\gamma_{i}, \gamma_{ii}, \gamma_{iii}$, respectively. Substituting the values of $\gamma_{\mathrm{L}}^{\mathrm{LW}}$, γ_{L}^{-}, γ_{L}^{+} and θ_{L} into Equation 13 and combining three equations together, we obtain a matrix to solve for the solid surface tensions γ_S^{LW}, γ_S^- , and γ_S^+:

$$\begin{bmatrix} \gamma_S^{LW} \\ \gamma_S^+ \\ \gamma_S^- \end{bmatrix} = \left\{ \left[2 \begin{pmatrix} \sqrt{\gamma_i^{LW}} & \sqrt{\gamma_i^-} & \sqrt{\gamma_i^+} \\ \sqrt{\gamma_{ii}^{LW}} & \sqrt{\gamma_{ii}^-} & \sqrt{\gamma_{ii}^+} \\ \sqrt{\gamma_{iii}^{LW}} & \sqrt{\gamma_{iii}^-} & \sqrt{\gamma_{iii}^+} \end{pmatrix} \right]^{-1} \begin{pmatrix} \gamma_i \ [\cos\theta_i + 1] \\ \gamma_{ii} \ [\cos\theta_{ii} + 1] \\ \gamma_{iii} \ [\cos\theta_{iii} + 1] \end{pmatrix} \right\}^2 \qquad 4.8$$

By using the above equations, one can determine Lifshitz-van der Waals (LW), and the acid and base components of surface energy of gypsum (CaSO4•$2H_2O$) and ZnS sensor. The surface energy was determined as γ ~48 mJ/m^2 for freshly cleaved selenite plane and ~50 mJ/m^2 for freshly cleaned ZnS sensor. The detailed surface energy components are listed in Table 4.2.

By using equation 4.1, 4.2, 4.3 and 4.4, the free energy ΔG is calculated and the result is shown in Table 4.3. Since ΔG is positive (20.14), gypsum crystallization on zinc sulfide surface is not thermodynamically favourable.

Table 4.1 Probing liquid used for measuring the surface energy [13]

Probing liquid	γ^{total}	γ^{LW}	γ^{+}	γ^{-}
Ethylene glycol	48.00	29.00	1.92	47.00
Diiodomethane	50.80	50.80	0.00	0.00
DMSO	42.97	29.20	0.20	237.00
Water	72.80	21.80	25.50	25.50
Glycerol	64.00	34.00	3.92	57.40
Formamide	58.00	39.00	2.28	39.60

Table 4.2 Contact angle measurement results and surface energy components of gypsum and ZnS sensor

	Surface energy components					**Contact angles**					
	γL	γ+	γ-	γAB	γtotal	Water	Glycerol	Formamide	EG	DMSO	Diiodomethane
Gypsum	47.14	0.002	47.87	0.62	47.76	-	-	-	22	33	22.1
ZnS	44.31	0.202	39.31	5.63	49.94	38.2	45.3	31.5	-	-	-

Table 4.3 Free energy calculation of gypsum crystallization on zinc sulfide surface

$\gamma_{gypsum\text{-}ZnS}$	$\gamma_{gypsum\text{-}solution}$	$\gamma_{ZnS\text{-}solution}$	ΔG
-0.48	-13.83	-6.80	20.14

4.3.4 Scanning electron microscope

An experimental study of gypsum crystallization on sphalerite surface was performed in this section. In order to avoid the adsorption of gypsum formed in bulk onto sphalerite surface, a tea-bag and de-sliming approach [14] was taken as follows.

1) About 2 grams of sphalerite particles with size ~100μm and 5~μm were cleaned with pH 2 HCL solution for 10 minutes

2) The particles were then dried with nitrogen

3) Filled the particles into a nylon tea bag

4) Put the tea bag into the mixing solution of 0.021M calcium chloride and sodium sulfate as shown in Figure 4.4

5) Sealed the container of the solution

6) Took out the tea bag after 24 hours

7) Transferred the particles into another container filled with ethanol

8) Sonicated the container for 5 minutes

9) Decanted the container and add fresh ethanol

10) Repeated step 8) and 9) for 5 times

11) Dried the particles with nitrogen and sent for SEM characterization

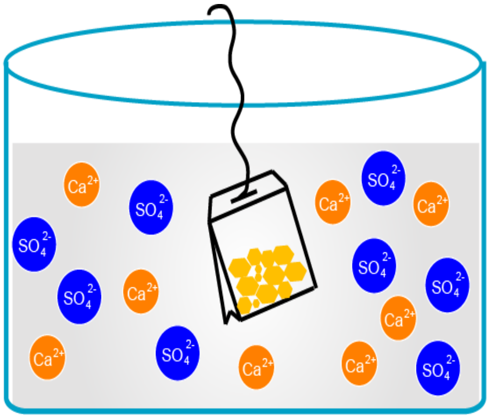

Figure 4.4 Schematic showing of the tea-bag approach

The morphology sphalerite particles was characterized with SEM, and the results are shown in Figure 4.5 and Figure 4.6. In Figure 4.5, there are clearly some big needle shape crystals which are typical shape of gypsum formed in solution. The sphalerite particles and gypsum crystals do not appear to aggregate together and therefore the surface of sphalerite is smooth without obvious needle shape gypsum crystal. For Figure 4.6, the particle size of sphalerite is about 100 μm. There is no big gypsum crystal as what was observed in Figure 4.5. However, some tiny needle crystals can be seen on the surface of sphalerite, appearing to be growing on the surface. The possibility of coagulation of gypsum formed in bulk and sphalerite still cannot be ruled out even a tea-bag desliming approach is taken [15].

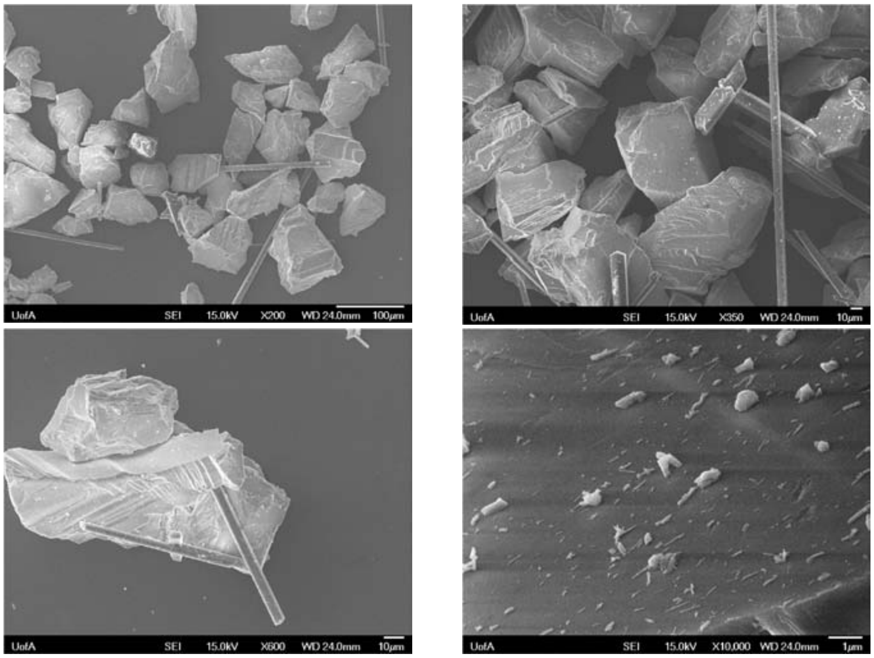

Figure 4.5 Morphology of sphalerite particles (~5μm) after dipping into calcium sulfate solution for 24 hours using a tea-bag approach described above. The needle shape crystal is gypsum.

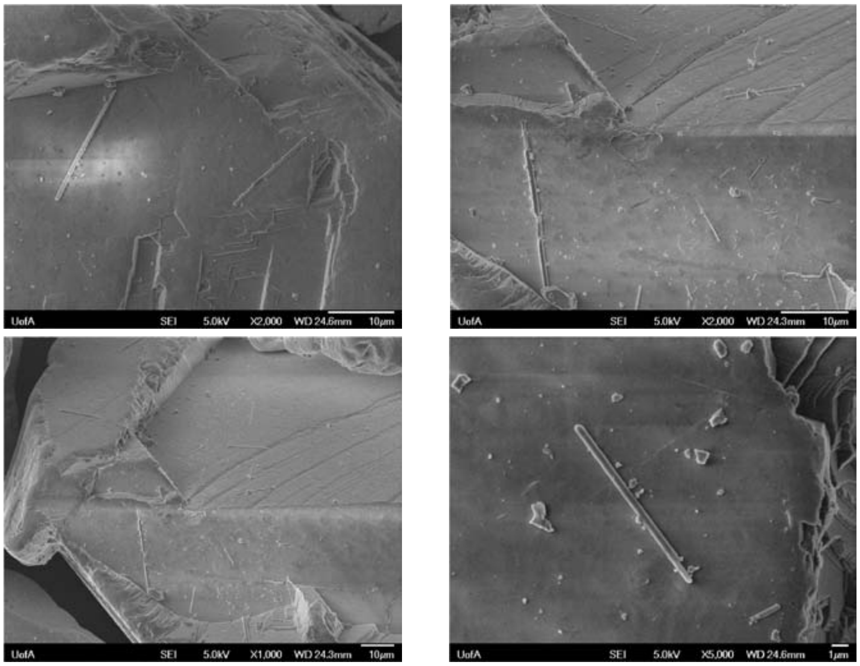

Figure 4.6 Morphology of sphalerite particles (~100μm) after dipping into calcium sulfate solution for 24 hours using a tea-bag approach described above. The needle shape crystal is gypsum.

4.4 Conclusions

In this study, the effect of calcium sulfate on sphalerite flotation is investigated and following conclusions are drawn.

1) Calcium adsorption on zinc sulfide surface was reversible at pH 6.5 and pH 10
2) The presence of calcium hindered the uptake of copper and adsorption of potassium amyl xanthate at pH 6.5
3) The recovery of sphalerite was not affected by the presence of calcium at pH 10 when the activator concentration was very high
4) Theoretical calculation showed the gypsum crystallization on zinc sulfide surface was not thermodynamically favorable
5) For small sphalerite particle, gypsum was not prone to nucleate or adsorb to sphalerite surface from saturated solution. For big sphalerite particle, tiny gypsum crystals were observed on the surface.

4.5 References

[1] D.W. Fuerstenau, A century of developments in the chemistry of flotation processing, Society for Mining, Metallurgy and Exploration, Inc.(SME), 2007.

[2] F.K. Ikumapayi.

[3] B. Nanthakumar, D. Grimm, M. Pawlik, International Journal of Mineral Processing, 92 (2009) 49-57.

[4] C. Sui, F. Rashchi, Z. Xu, J. Kim, J.E. Nesset, J.A. Finch, Colloids and Surfaces A: Physicochemical and Engineering Aspects, 137 (1998) 69-77.

[5] M.J. Pearse, Minerals Engineering, 18 (2005) 139-149.

[6] D. Lascelles, J. Finch, C. Sui, Canadian metallurgical quarterly, 42 (2003) 133-140.

[7] A. DiFeo, J.A. Finch, Z. Xu, International journal of mineral processing, 61 (2001) 57-71.

[8] C. Sui, F. Rashchi, Z. Xu, J. Kim, J. Nesset, J. Finch, Colloids and Surfaces A: Physicochemical and Engineering Aspects, 137 (1998) 69-77.

[9] G. Lefèvre, M. Fédoroff, Physics and Chemistry of the Earth, Parts A/B/C, 31 (2006) 499-504.

[10] S.R. Rao, Xanthates and related compounds, M. Dekker, 1971.

[11] F. Chachula, Q. Liu, Fuel, 82 (2003) 929-942.

[12] J. Laskowski, Q. Liu, Y. Zhan, Minerals engineering, 10 (1997) 787-802.

[13] C. Della Volpe, S. Siboni, Journal of colloid and interface science, 195 (1997) 121-136.

[14] R.S.C. Smart, Minerals engineering, 4 (1991) 891-909.

[15] S.C. Sun, Trans. AIME, 153 (1943) 479.

Chapter 5 Understanding the Deposition and Surface Interactions of Gypsum*

5.1 Introduction

Water is a process medium in mineral processing. Most minerals processing plants are practicing reclamation of process water to reduce the consumption of fresh water,[1, 2] and high level of salinity is contained in the recycled water due to environmental regulation restriction on total dissolved solids (TDS) of discharge water. For example, in sulphide flotation plants practicing water recycling, high levels of calcium ions are frequently experienced.[3] In some process water, Ca^{2+} ion concentrations exceed 2.5×10^{-2} M (1000 ppm)[4] The Ca^{2+} ions mainly come from dissolution of calcium-containing minerals[5] and the addition of lime as a pH modifier and pyrite depressant.[4] A high concentration of sulphate ions (SO_4^{2-}) also exists in the process water of sulphide flotation plants owing to either oxidization of sulphide or addition of zinc sulphate and copper sulphate as deactivator and activator in the case of sphalerite flotation.[6] When a recycled water stream with a high concentration of calcium (Ca^{2+}) and sulphate (SO_4^{2-}) ions is incorporated in the process, potential precipitation of calcium sulphate dihydrate ($CaSO_4•2H_2O$, referred to as gypsum hereafter) on both desired sulphide minerals and silicate gangues makes both mineral surfaces of same surface characteristics, thus decreasing the selectivity and flotation recovery[7, 8] A basic understanding of the interactions between gypsum precipitates, silicates, and sulphide surfaces is greatly needed, not only for sulphide minerals flotation, but also for many other industrial operations with gypsum and silicates involved in aqueous media [9].

Athough many studies reported the complex interactions between sulphide minerals, calcium and sulphate ions and other gangue particles from flotation and

---

*Published paper: F. Teng, H. Zeng, Q. Liu, Journal of Physical Chemistry C, 115 (2011) 17485-17494 electrochemical perspectives,[4, 10-12] little research has been committed to understanding directly epitaxial growth of gypsum on another solid substrate like silicates [13] or sulphide materials in the presence of high concentrations of both calcium and sulphate ions. A better understanding of the determinants and the nature of gypsum precipitation and crystallization on silicates may enhance the control of these precipitates on gangue minerals, leading to a better flotation performance of valuable minerals while minimizing environmental impacts. In the meantime, there is a great need to understand the interactions of gypsum surfaces due to their wide existence in the flotation system.[14]

Mica is a naturally occurring mineral that consists of hydrous silicates, most commonly of aluminum or potassium, which has the hexagonal sheet-like arrangement of the atoms and highly perfect cleavage characteristics for creating atomically smooth surfaces.[15] Mica is chosen as a supporting substrate for the crystallization of gypsum in this study as an example of silicate minerals. Atomic force microscope (AFM) and scanning electron microscope (SEM) were applied to investigate the morphology of the gypsum crystals grown on mica. Surface forces apparatus (SFA) has been used for many years to measure the physical forces between surfaces, including van der Waals and electrostatic forces in various vapors and liquids,[16] adhesion forces,[17] capillary forces, forces due to surface and liquid structure (e.g. solvation and hydration forces),[18] steric and hydrophobic interactions,[19] bio-specific interactions as well as friction and lubrication forces.[20] Due to its unique ability to provide a simultaneous direct measurement of the force, F, as a function of the absolute surface separation, D, and the local geometry of two interacting surfaces (the local radius R or contact area) measured *in situ* and in real time, SFA has been extensively used in many biologically and non-biologically related research, and could be an unique technique for the study of surface interactions in mineral systems.

Surface roughness has significant impact on many physical and mechanical properties of surfaces and materials and their interfacial interactions (adhesion, friction, local deformation or failure).[21-23] Roughness also affects the interactions and stability of colloidal particles in solutions, to which most classical contact mechanics models and colloid theories cannot be directly applied. Although significant progress has been made on theoretical contact mechanics models for rough surfaces[24, 25] and a recent experimental study was also reported on rough soft polymer surfaces,[26] there is no experimental report available on the surface interactions of rough hard materials. In this work, we have investigated the gypsum crystallization behaviour on silicate mineral, the interaction mechanism between coated gypsum surfaces and the roughness effects on the surface forces, and the surface interactions between silicate minerals in calcium sulphate solution of different concentrations, which are of both fundamental and practical importance in colloid and interface science, sulphide minerals flotation and many industrial operations.

5.2 Experimental

5.2.1 Materials

Calcium Sulphate Hemihydrate (USG Corporation, USA) and ethanol (91wt%, Fisher Scientific) were used as received without further purification. Muscovite mica sheets (grade #1, S&J Trading Inc. USA) were freshly cleaved prior to each experiment. Calcium hydroxide (98wt%, Fisher Scientific) and sulphuric acid (98wt%, Fisher Scientific) solutions were used for preparing gypsum surfaces with dipping method. All solutions used in this study were prepared using Milli-Q water (Millipore deionized, >18.2 MΩcm, 0.22-μm-filtered) and filtered by 0.2 μm filter after complete mixing. All tests were conducted at 23°C.

5.2.2 Analytic techniques

Morphology of gypsum crystal grown on mica sheets and the surface roughness were characterized with an atomic force microscope (AFM) (Multimode Veeco, Santa Barbara, CA, USA). Surface texture and element analysis of the samples were provided by a scanning electron microscope (SEM) (Zeiss EVO MA 15), equipped with a Bruker Silicon Drift Detector for Energy Dispersive X-Ray analysis (EDX). A surface forces apparatus, SFA (Surforce

LLC, Santa Barbara, CA, USA) was applied to measure the interaction forces between mica and gypsum surfaces.

5.2.3 Calcium sulphate solution preparation

Calcium sulphate solutions of four concentrations (0.00013 M, 0.001 M, 0.01 M and 0.033 M) were prepared by dissolving 0.0019g, 0.0145g, 0.145g and 0.478g hemihydrate in 100ml Milli-Q water. All solutions were mixed for at least 30 minutes (so no visible particles in solution), and filtered with 0.2 μm filter. pH of the filtered solutions was measured to be in the range of 4.9 - 5.1. The prepared solutions were later used in force measurement between two mica surfaces by a SFA.

5.2.4 Gypsum coating preparation

In the present study, mica was used as a supporting substrate for gypsum coating due to its highly perfect cleavage characteristics along {001} planes and atomically smooth surface in nature.[15] Clean mica surfaces were prepared by cutting into 20mm×20mm sheets and freshly cleaving in laminar flow hood. The mica sheets were then rinsed thoroughly with Milli-Q water and dried in laminar hood. Three different coating methods were utilized to prepare gypsum coating on mica sheet: (1) dropping method, (2) suspending method, and (3) dipping method. Figure 5.1 shows the three coating methods schematically.

5.2.4.1 Dropping method

The gypsum solutions were prepared by dissolving 0.35 g hemihydrate in 100 ml Milli-Q water. After mixed for about 10 minutes, the solutions were filtered by 0.2 μm filter (Millipore). 1-3 ml of above prepared solution was dropped onto a clean mica sheet to cover the whole surface as shown in Figure 5.1(a), and the mica sheet was left to completely dry in laminar hood at room temperature. After all liquid was evaporated, the sample was rinsed with ethanol and air-dried again in laminar hood for further characterization. It should be noted that gypsum crystallization could occur both in bulk solution and on mica surface during the drying process. The gypsum crystals in bulk solution could precipitate and attach onto mica or gypsum crystals previously grown on mica, some of which could not be easily rinsed away by ethanol. Therefore, the gypsum coating prepared using the dropping method was both attached and grown on mica.

5.2.4.2 Suspending method

A clean mica sheet was held by a pair of stainless steel tweezers, allowing one side of the mica sheet facing down immersed in the gypsum solutions prepared by dissolving 0.35 g hemihydrate in 100ml Milli-Q water, as shown in Figure 5.1(b). The sheet was suspended in the solution for different time (5 min, 20 min, 2, 4 and 17 hours), and then rinsed with ethanol immediately to remove all residues, and finally air-dried in laminar hood.

5.2.4.3 Dipping method [27]

0.02 M calcium hydroxide and sulphuric acid solutions were prepared as follows: 0.152 g calcium hydroxide was dissolved in 100 ml Milli-Q water and 0.2 g concentrated sulphuric acid (98 wt%) was added into 100 ml Milli-Q water slowly. After complete mixing and filtration with 0.2μm filter, gypsum was coated onto mica surface by following the procedure below (shown in Figure 5.1(c)):

1) A clean mica sheet was dipped into the 0.02 M calcium hydroxide solution for 1 minute. A thin liquid film was formed on the sample surface after taking out the sample from the solution. The sample was left in laminar hood for about 3 minutes to complete dry at room temperature.
2) The dried mica sample was dipped into Milli-Q water for ~2 seconds and air-dried in laminar hood.
3) The mica sample was then dipped into the sulphuric acid solution for 1 minute, and taken out and then it was left in laminar hood for ~3 minutes to completely dry at room temperature.
4) The dried mica sample was dipped into Milli-Q water for 2 seconds and air-dried in laminar hood.
5) Repeat steps 1) to 4) for various (3, 5 and 12) cycles.
6) Finally, the mica sheet was rinsed with ethanol and air-dried in a laminar hood.

5.2.5 Surface forces measurement

An SFA was used to investigate the interaction forces between two mica surfaces in solutions of calcium and sulphate ion concentrations ranging from 0.00013 to 0.033 M, and the forces between two gypsum-coated mica surfaces in air. Detailed setup for SFA experiments has been reported previously.[28, 29] Briefly, a thin mica sheet of 1-5 μm was glued onto a cylindrical silica disk (radius R=2 cm). The back surfaces of the mica substrates were coated with 50-55 nm thick semi reflective layer of silver, required to obtain multiple-beam interference fringes of equal chromatic order (FECO), which were used to monitor the surface separation, shape, deformations and the contact area in real time and in situ. The two curved mica surfaces were then mounted into the SFA chamber in a crossed-cylinder geometry, which roughly corresponded to a sphere of radius R approaching a flat surface based on the Derjaguin approximation: $F(D) = 2\pi RW(D)$, where $F(D)$ was the force between the two curved surfaces, and $W(D)$ was the interaction energy per unit area between two flat surfaces. A schematic drawing of the SFA experimental setup for measuring gypsum surfaces interaction was shown in Figure 5.2. The distance D=0 was set as the adhesive contact between two bare mica surfaces in air. The normal forces between the mica surfaces in gypsum solution were measured by moving the lower surface supported by a double-cantilever ‘force springs’ by a distance $\Delta D_{\text{applied}}$. The actual distance that the surfaces moved relative to each other, ΔD_{meas}, was measured by multiple beam interferometry (MBI). The changed force ΔF between the surfaces, when they came to rest at a separation D, was therefore, $\Delta F(D) = k\,(\Delta D_{\text{applied}} - \Delta D_{\text{meas}})$, where k was the spring constant. When $\partial F(D)/\partial D > k$, there was a mechanical instability and the lower surface jumped either toward or away from the upper surface during approach or separation processes, respectively. The forces between two gypsum surfaces, coated on mica sheets by using dipping method, were also measured in air. The distance D=0 was referred to the contact of two bare mica sheets prior to gypsum coating.

(a) Dropping method

(b) Suspending method

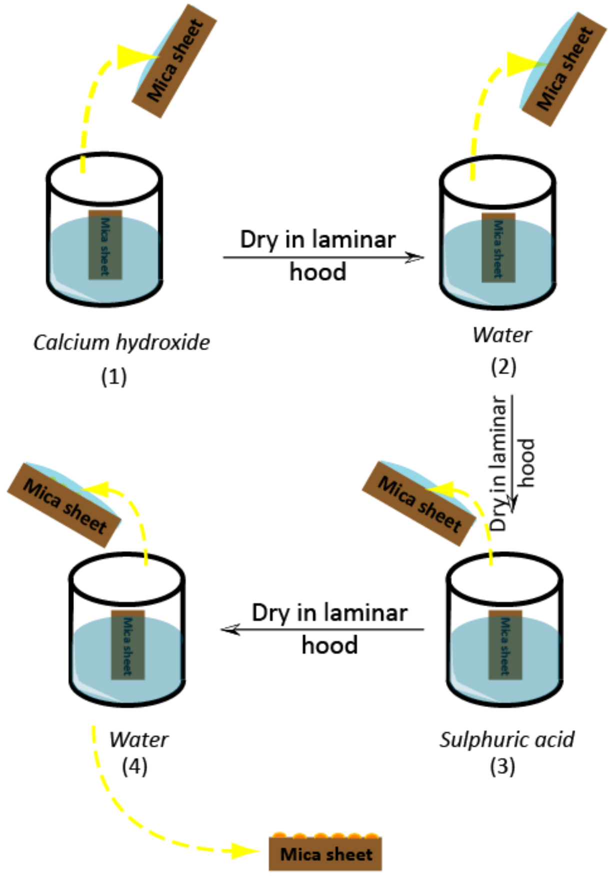

(c) Dipping method

Figure 5.1 Schematic of three methods for coating gypsum on mica sheets. a) Dropping method, a droplet of hemihydrate solution was dropped onto the mica surface. b) Suspending method, mica sheet was faced down to touch surface of gypsum solution. c) Dipping method.

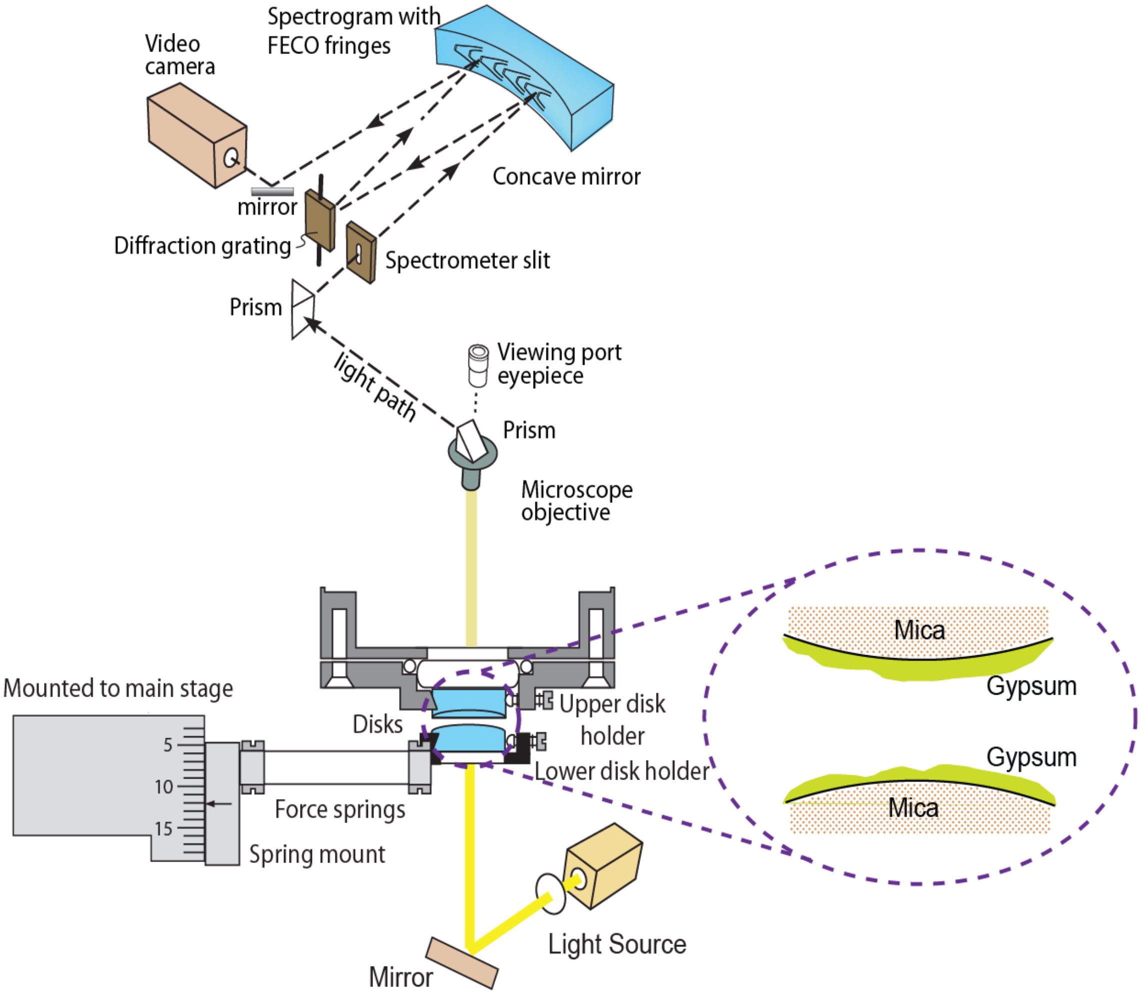

Figure 5.2 Schematic drawing of the surface forces apparatus (SFA) experimental setup for measuring the interactions between two gypsum-coated mica surfaces

5.3 Results and discussion

5.3.1 Morphology characterization of gypsum coatings

The AFM images of gypsum coatings on mica prepared by three methods: dropping, suspending and dipping are given in Figure 5.3, which show that the coated crystals have different sizes and geometric features. The crystals coated by dropping method shown in Figure 5.3(a) exhibit both pyramid and needle type structure with much higher feature in normal direction to the mica sheet than that prepared by other two coating methods shown in Figure 5.3(b) and (c), which is attributed to high crystal growth rate achieved at high supersaturation degree that increased quickly as water gradually evaporated in laminar hood.[30] Crystals with tree-like architecture were formed all over the mica surface prepared using suspending method as shown in Figure 5.3(b). As the suspending time increased from 5 minutes to 17 hours, the branches of tree-like structure developed into larger needle crystals. The time-dependent gypsum crystal morphology of samples prepared by suspending method is shown in Figure 5.4, indicating a three-stage evolution of coated gypsum crystals includes three stages: (1) stage I, crystal branches of similar size were formed, most of which were interlinked with each other; (2) stage II, more gypsum crystal branches were formed on the mica surface while previously formed crystals continued growth in size and height, which increased the surface coverage gradually; (3) stage III, as suspending time increased, gypsum crystal branches merged and developed into large needle-like structure, which was the typical morphology of gypsum crystals formed in bulk solutions, with crystal length and height in tens of micrometers. Figure 5.3(c) shows the morphology of gypsum crystals grown on mica by dipping the mica sheet into 0.02 M calcium hydroxide and 0.02 M sulphuric acid solutions for 3 cycles. The gypsum crystals were observed to distribute uniformly on the mica surface, and the crystal cluster structure was different from Figure 5.3(a) and (b) obtained using the other two coating methods. It is also worth mentioning that the root mean square (RMS) roughness was in the order of Fig. 5.3 (a)>(b)>(c), of which the RMS was ~300 nm, ~40 nm, and ~10 nm respectively. The smoothest surfaces were acquired by the dipping method among the three methods used.

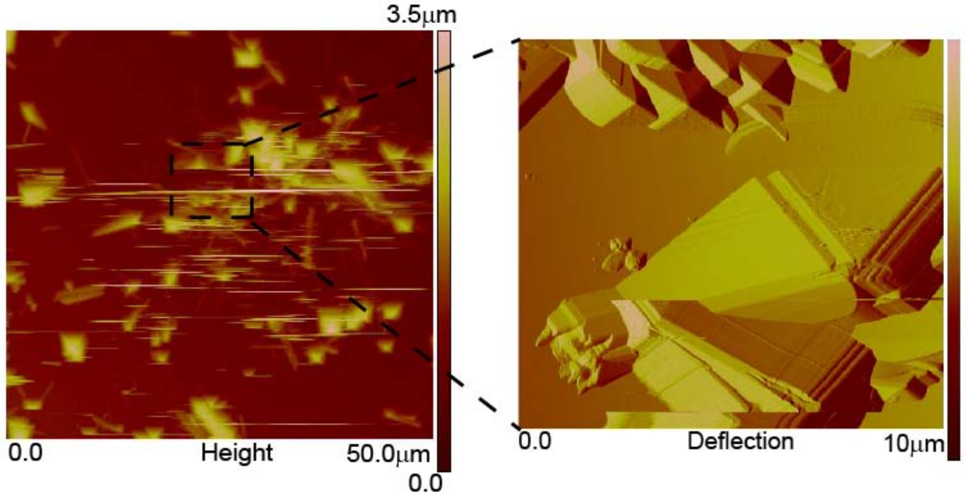

(a) Dropping

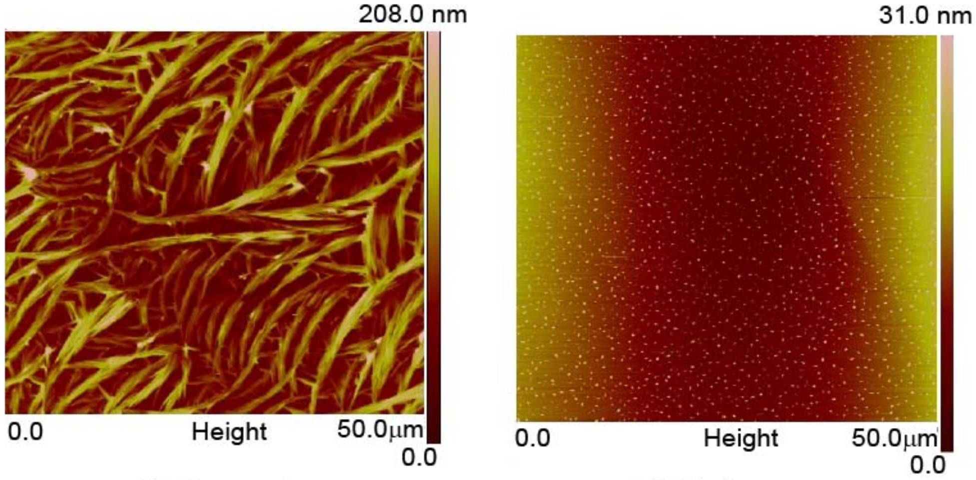

(b) Suspending (c) Dipping

Figure 5.3 Topographical AFM images of gypsum crystals coated on mica using three different methods. (a) Dropping method, ~3 ml 3.5 g/L hemihydrate solution was dropped onto freshly cleaved mica sheet, and the mica sheet was left in laminar hood for 30 minutes to allow water to fully evaporate and then rinsed with ethanol afterwards. Top right figure is the deflection image of AFM scanning in a local area to show the shape of the crystals. (b) Suspending method, freshly cleaved mica sheet was partially immersed into 3.5g/L hemihydrate solution with only one surface immersed in the solution for 20 minutes. (c) Dipping method, freshly cleaved mica sheet was dipped into aqueous solutions of calcium hydroxide (0.02 M) and sulphuric acid (0.02 M) sequentially for 3 cycles (detailed procedure is described in the experimental part).

The dipping method for depositing gypsum on mica is considered to be a crystallization process induced by evaporation and acid-base reaction, as shown in the schematic in Figure 5.5. After retracting the mica sheet from calcium hydroxide solution, a layer of aqueous solution was left on the mica substrate and Ca^{2+} ions were attracted to the negative charged mica surface. As water evaporated during drying step, the supersaturation degree was increased to induce crystallization of calcium hydroxide at the sites with higher concentration of calcium ions. Quick rinsing with Milli-Q water could flush away the calcium hydroxide crystals that were not strongly adhered to the mica surface. By the next dipping step, the formed calcium hydroxide crystals reacted with sulphuric acid to substitute hydroxyl groups by sulphate groups. A new liquid layer was left upon retracting the mica sheet from sulphuric acid solution. Similar as previous drying step, crystallization occurred as water evaporated, and calcium sulphate dihydrate crystals were formed. At the end of dipping process, the mica sheet was rinsed with ethanol to flush away all gypsum precipitates without strong binding to the substrate. The size of gypsum crystals and thickness of coating layer can be controlled by varying the numbers of dipping cycle.

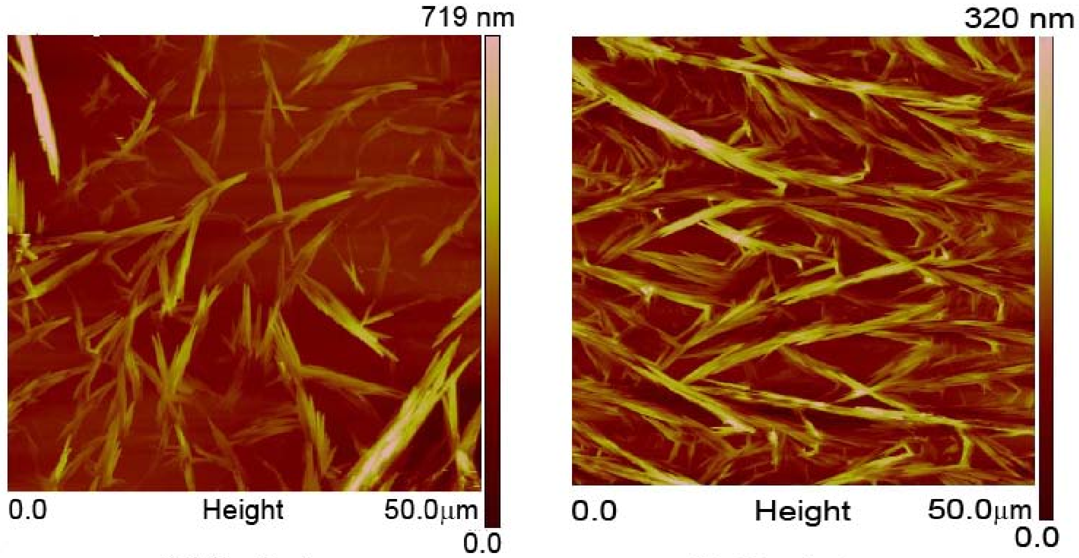

(a) 5 minutes (b) 20 minutes

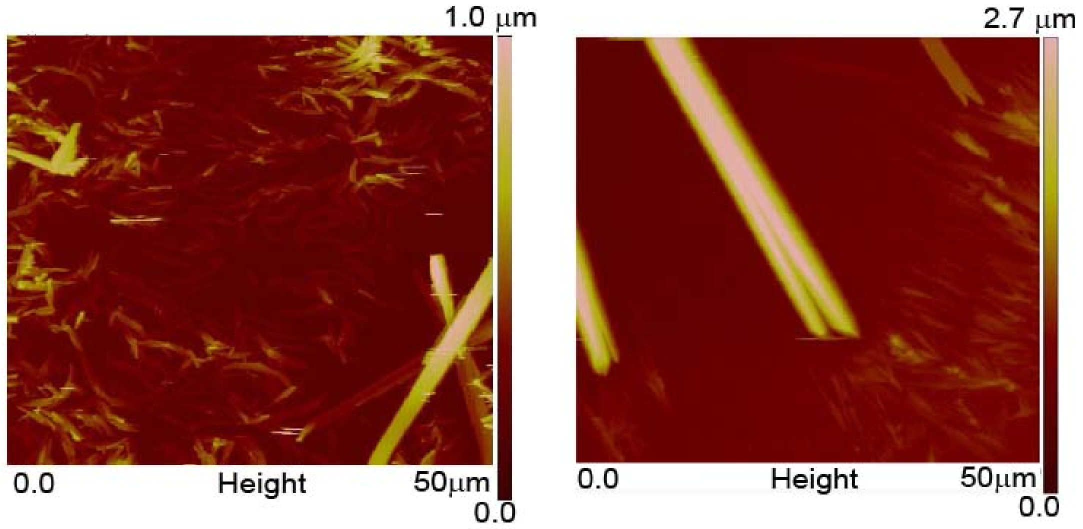

(c) 2 hours (d) 17 hours

Figure 5.4 Topographical AFM images of coated gypsum crystals on mica sheets suspended in 3.5g/L hemihydrate solution for different time: (a) 5 minutes, (b) 20 minutes, (c) 2 hours and (d) 17 hours.

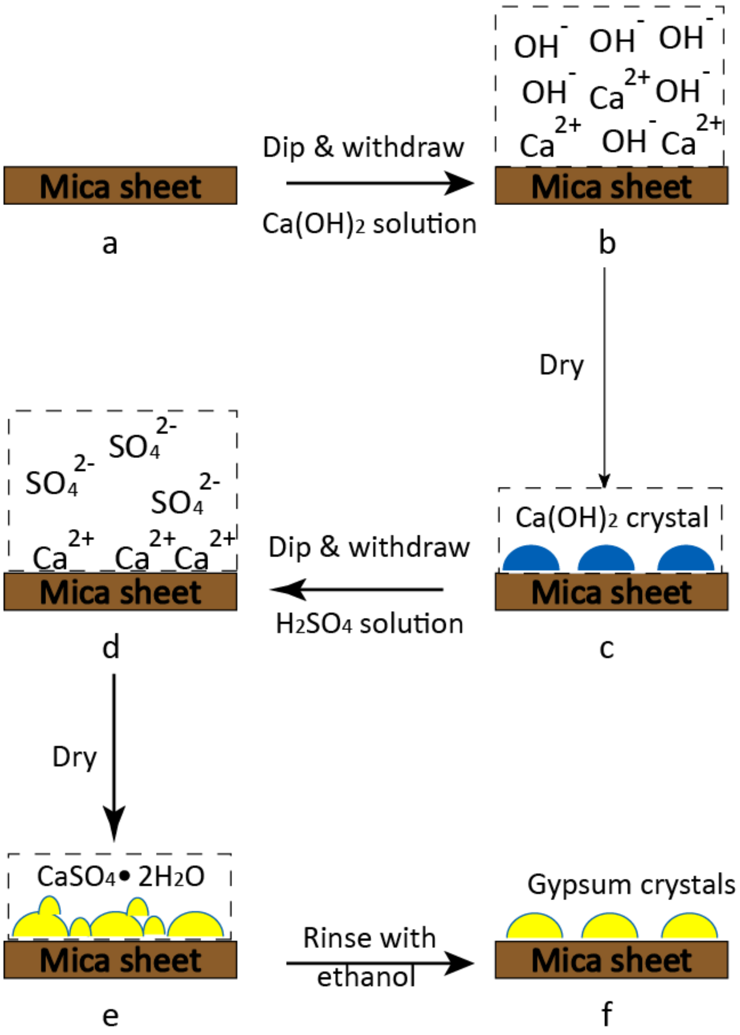

Figure 5.5 Schematic diagram of proposed crystallization mechanism induced by evaporation and acid-base reaction to coat gypsum onto mica surfaces using dipping method. (a) Freshly cleaved mica sheet. (b) Dipping and retracting mica sheet from calcium hydroxide solution with a liquid film containing calcium and hydroxyl ions left on surface. Positively charged calcium ions are attracted to negatively charged mica surface due to the release of potassium ions from mica basal plane. (c) Drying in laminar hood, water gradually evaporates from the liquid film and calcium hydroxide crystallizes on the substrate. (d) Dipping and withdrawing the mica sheet from sulphuric acid solution with a liquid film containing calcium and sulphate ions left on surface. (e) Water evaporates from liquid film in laminar hood and gypsum crystallizes on mica. (f) Rinsing with

ethanol to flush away all gypsum precipitates without strong binding to the substrate.

Figure 5.6 is a scanning electron microscope (SEM) image of a gypsum coated mica sample using dipping method for 12 cycles. Spherical-like crystals were observed all over the mica surface. The energy-dispersive X-ray spectroscopy analysis (EDX) coupled with the SEM confirmed that the ratio between calcium and sulphur atoms was ~1.0, which indicated that the formed crystals were gypsum (Ca:S=1:1) based on the fact that there was neither calcium nor sulphur in mica.

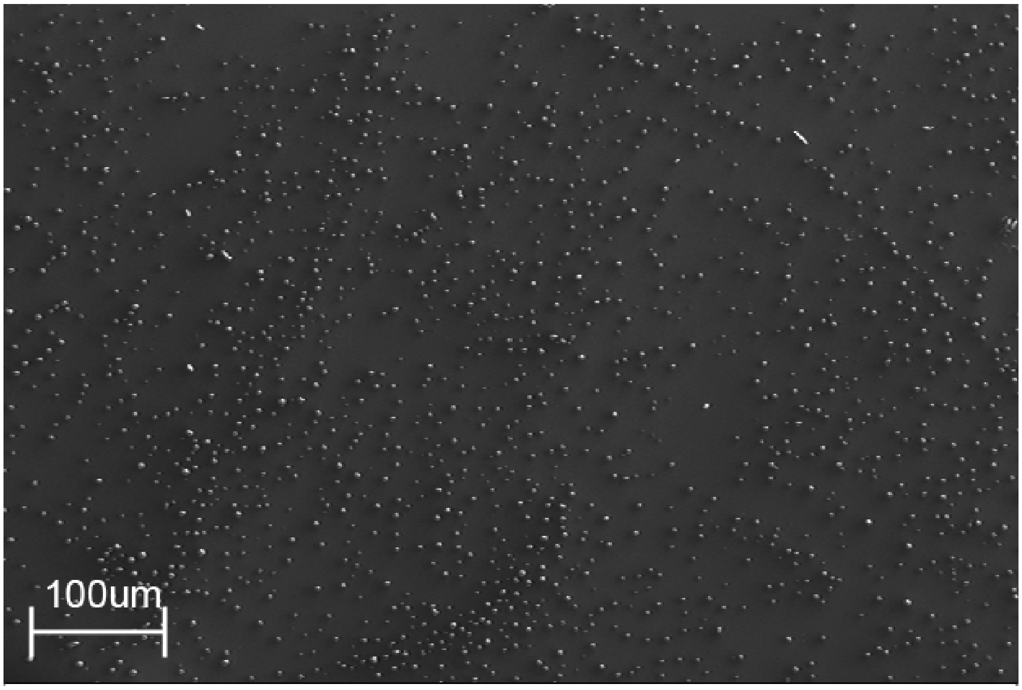

Figure 5.6 SEM image of coated gypsum on mica sheet by dipping method for 12 cycles.

5.3.2 Mica-mica interaction in calcium sulphate/$CaSO_4$ solution

In order to understand the effect of calcium sulphate solution on surface interactions of silicate minerals, the forces between two mica surfaces in calcium sulphate solution with different concentrations were measured using the SFA. The results are shown in Figure 5.7. The Derjaguin-Landau-Verwey-Overbeek (DLVO) theory [28] was applied to fit and describe the interactions of mica surfaces in $CaSO_4$ solutions. The DLVO theory describes the interaction energies between two charged surfaces in a liquid medium, which includes the attractive van der Waal energy and repulsive electrical double-layer energy due to the so-called double layer of counterions. The van der Waal energy per unit area E between two flat mica surfaces across aqueous solution with a separation distance D is given by

$$E_{VDW}(D) = -A_{\text{mica-water-mica}} / 12\pi D^2 \qquad \mathrm{J/m^2}, \qquad 5.1$$

where $A_{\text{mica-water-mica}}$ is the Hamaker constant for mica-water-mica system, which approximately equals to -2.2 $\times$ 10^{-20} J.[28, 31] The corresponding repulsive electrical double-layer energy per unit area between two flat mica surfaces in $CaSO_4$ solution (a 2:2 electrolyte aqueous system) with constant surface potential at T=296K is

$$E_{EDL}(D) = \frac{64CN_AkT}{\kappa}\tanh^2\left(\frac{ze\psi}{4kT}\right)e^{-\kappa D} = 1.81\times10^{-12}\kappa\tanh^2\left(\frac{\psi}{51.5}\right)e^{-\kappa D} \qquad \mathrm{J/m^2}, \qquad 5.2$$

where C is the concentration of $CaSO_4$ solution (mol/L), and N_A is Avogadro constant. Ψ is the surface potential of mica surface in mV, which is usually in the range of -50 to -150 mV.[32] z is the valence of electrolyte, and z=2 for $CaSO_4$ solution. κ^{-1} is the Debye length, given below for a 2:2 electrolyte system:

$$\kappa^{-1} = \frac{0.152}{\sqrt{C}}\,\mathrm{nm}, \qquad 5.3$$

where C is the solution concentration in mol/L.[16]

Therefore, the total interaction energy including van der Waal and electrical double-layer energies for two flat mica surfaces in $CaSO_4$ solution is

$$E_{TOTAL} = E_{VDW} + E_{EDL} = -2.2\times10^{-20}/12\pi D^2 + 1.85\times10^{-12}\kappa\tanh^2\left(\frac{\psi}{51.5}\right)e^{-\kappa D} \quad \mathrm{J/m^2}, \quad 5.4$$

According to the Derjaguin approximation, the interaction forces between two mica surfaces in crossed-cylinder geometry in SFA measurement can be related to E_{TOTAL} by[28]

$$F(D)/R = 2\pi E_{TOTAL}(D) = -2.2\times10^{-20}/6D^2 + 1.14\times10^{-11}\kappa\tanh^2\left(\frac{\psi}{51.5}\right)e^{-\kappa D}\,\mathrm{J/m^2}, \quad 5.5$$

The fitting curves by applying Equation 5.5 were show in Figure 5.7. For low concentrations (0.00013 M, 0.001 M and 0.01M) of $CaSO_4$, the DLVO model fits the experimental results very well, with the mica surface potential ~-85 mV consistent with the literature value [33] and Debye length κ^{-1}=13.9 nm, 5.7 nm and 2.4 nm for the 0.00013 M, 0.001 M and 0.01M $CaSO_4$ solutions respectively, which are close to the theoretical values 13.3 nm, 4.8 nm and 1.5 nm given by Equation 5.3. It should be noted that the activity of an ion in many colloidal systems is less than its concentration (i.e., the activity coefficient is less than 1). Especially for multivalent electrolytes, the activity coefficients can deviate markedly from unity, even in relatively dilute solutions. For example, the activity coefficients for monovalent and divalent ions are ~0.96 and ~0.75, respectively at a concentration of 10^{-3} M.[34] Based on the experimentally measured Debye length in Figure 5.10, the activity coefficients for $CaSO_4$ at $\sim 1.3 \times 10^{-4}$, 10^{-3} and 10^{-2} M are 0.92, 0.7 and 0.4 respectively, which are very close to the values reported by Lilley, *et al.* for $CaSO_4$ under the similar concentrations.[35]

For $CaSO_4$ solution at 0.033 M, which is higher than saturation concentration of gypsum, the DLVO model fails to fit the force-distance profile shown in Figure 5.7(d). An evident “hard wall” distance of 50 nm is observed from the force curve, which may be attributed to the nucleation and precipitation of gypsum from supersaturated solution. The presence of gypsum crystals hinders the contact of two mica surfaces. In real industrial applications, it is not easy to distinguish nucleation/crystallization or attachment of gypsum on mineral surfaces because of the very high concentrations of $CaSO_4$ and the presence of gypsum crystals in bulk solutions. However, for the present study, we believe that the observed repulsive force between two mica surfaces in the presence of 0.478 g/100 ml calcium sulphate hemihydrate solution (0.033 M) was mainly due to the nucleation/crystallization of gypsum on mica surfaces. The attachment of gypsum crystals from solution was rather limited. It should be noted that in practice, the solubility of calcium sulphate hemihydrate of ~0.65 g/100 ml [36, 37] is higher than the solubility of dihydrate of ~0.24 g/100 ml at 20°C, and the solution was observed to be still optically clear after the duration of the SFA measurement (~1 hour), and thus the gypsum crystallization in bulk solution with 0.478 g/100 ml calcium sulphate hemihydrate was very limited.

The force measurement results between two silicate surfaces in the presence of calcium sulphate solution indicate that the addition of gypsum at low concentration decreases the repulsive forces between silicate surfaces due to the compression of double layer, therefore facilitating the coagulation and settling of clay minerals in various mineral operations and tailing stream. However, when the calcium sulphate solution becomes saturated or oversaturated, gypsum can nucleate and form crystals on negative charged silicates, which prevents the silicates from coagulating in mineral processing. On the other hand, if the gypsum grows on the surfaces of valuable minerals to be recovered or removed from the mineral system, one will lose the separation efficiency.

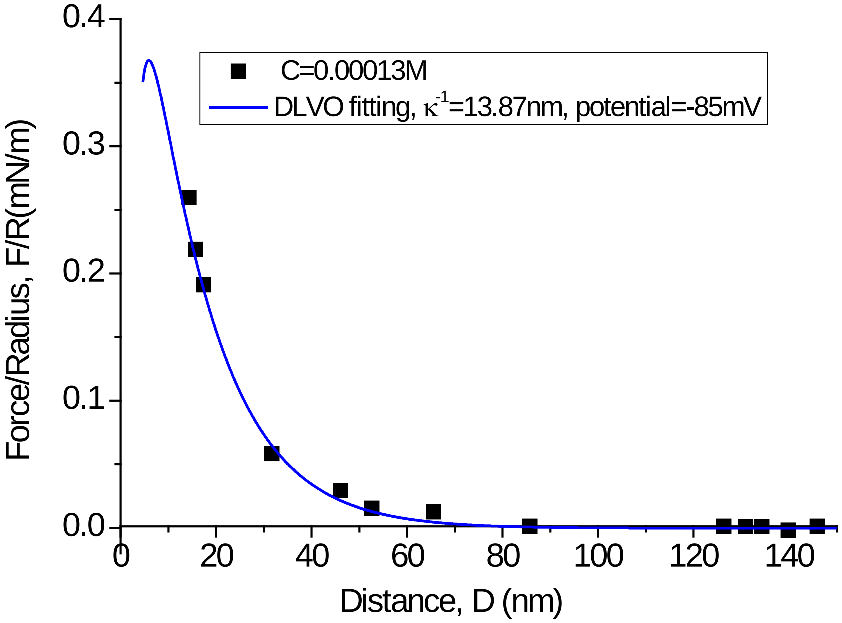

(a)

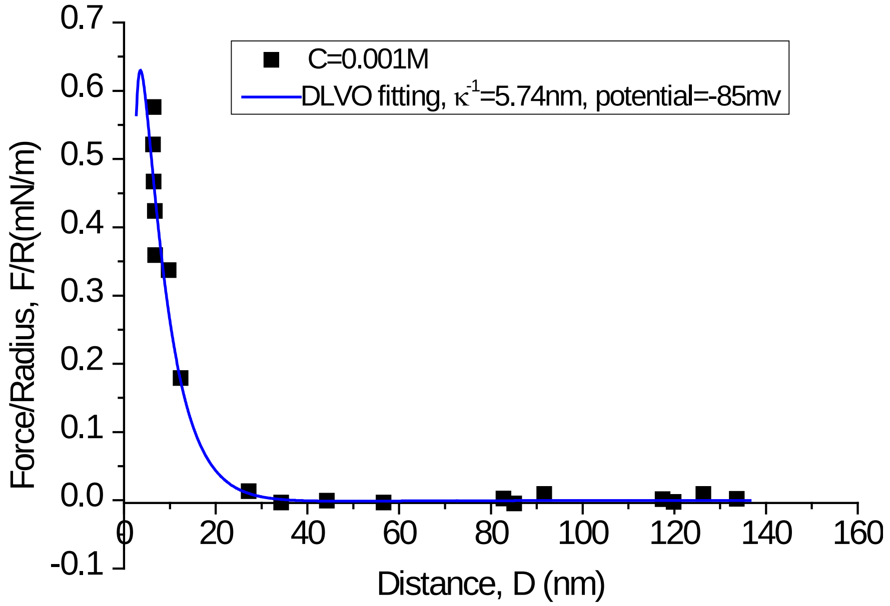
0.7
0.6
0.5
0.4
0.3
0.2
0.1
0.0
-0.1
Force/Radius, F/R(mN/m)
0
20
40
60
80
100
120
140
160
Distance, D (nm)
■ C=0.001M
DLVO fitting, κ-1=5.74nm, potential=-85mv

(b)

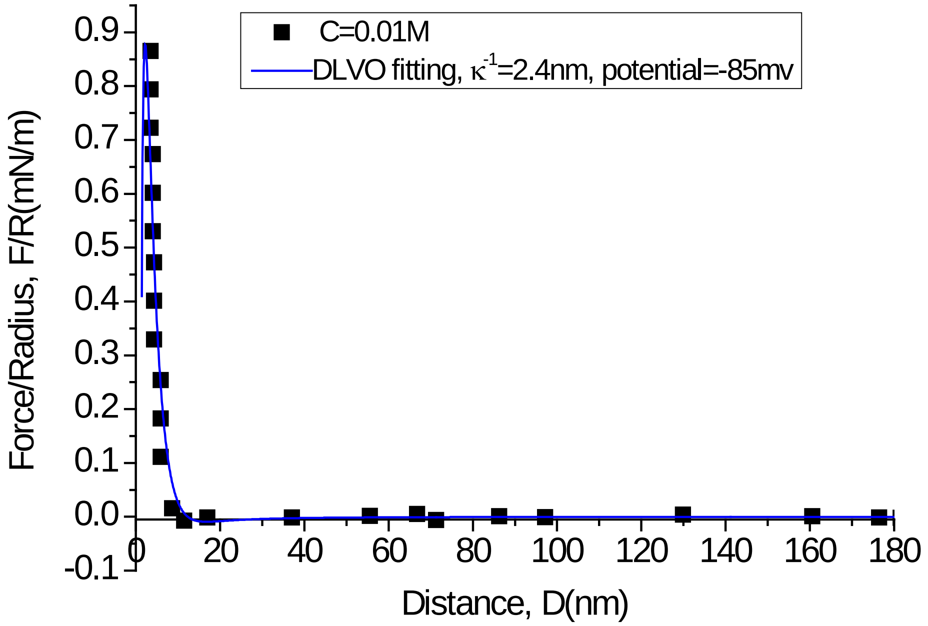
0.9
0.8
0.7
0.6
0.5
0.4
0.3
0.2
0.1
0.0
-0.1
Force/Radius, F/R(mN/m)
0
20
40
60
80
100
120
140
160
180
Distance, D(nm)
■ C=0.01M
DLVO fitting, κ-1=2.4nm, potential=-85mv

(c)

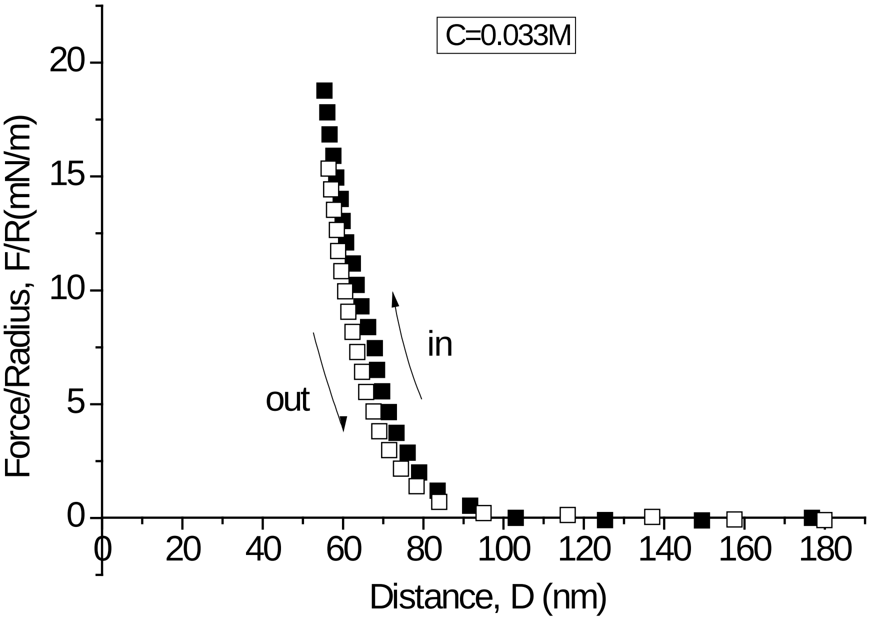

(d)

Figure 5.7 Interaction forces between two mica surfaces in $CaSO_4$ solution of different concentrations, (a) 0.00013 M, (b) 0.001 M, (c) 0.01 M, and (d) 0.033 M.

5.3.3 Surface forces between two rough gypsum surfaces

The samples prepared by dipping method were chosen for force measurement with a SFA due to the smaller RMS roughness compared with dropping and suspending methods. Two silica disks glued with thin mica sheet on the top, treated by dipping methods in 0.02 M calcium hydroxide and sulphuric acid solutions by turns, were mounted against each other in the SFA chamber and then brought into contact using a motor-controlled micrometer. Figure 5.8 shows the typical force-distance profiles for three samples by dip coating for 5, 8, and 12 cycles with RMS roughness of 4, 17 and 200 nm respectively. Pure repulsive force was observed for all three samples after the rough gypsum surfaces were brought into initial contact. The approach (loading) and separation (unloading) force curves almost overlapped with each other. The absence of attractive force can be attributed to the surface roughness of coated gypsum layers, as the result of the competition between attractive van der Waals force and repulsive elastic force of asperities upon exerting compressive force.[38] During separation (unloading), no obvious adhesive forces were measured under low compressive load (maximum *F*/*R*: 15-25 mN/m or maximum compressive force: 0.3-0.5 mN) as shown in Figure 5.8, while adhesion was observed at higher load conditions (see Figure 5.9), which is similar to the randomly rough polymer surface in a previous study.[26]

The normal forces measured on approach (and separation) after initial contact exhibited an exponential repulsion with decay length λ varying from 5.5 nm to 38 nm, as shown in Figure 5.8(b). A noticeable trend is that the exponential decay length λ increases with increasing rms roughness of the coated surfaces. λ reflects how fast the separation between two supporting substrate surfaces reaches a "hard wall", which means the supporting mica-mica separation at which the thickness of the confined gypsum becomes asymptotic with increased normal load or pressure. The smaller the decay length is, the faster the separation reaches hard wall. As the surfaces get rougher (having larger RMS), the onset of the repulsive force (first contact of the outermost asperities) shifts to larger separation distances.

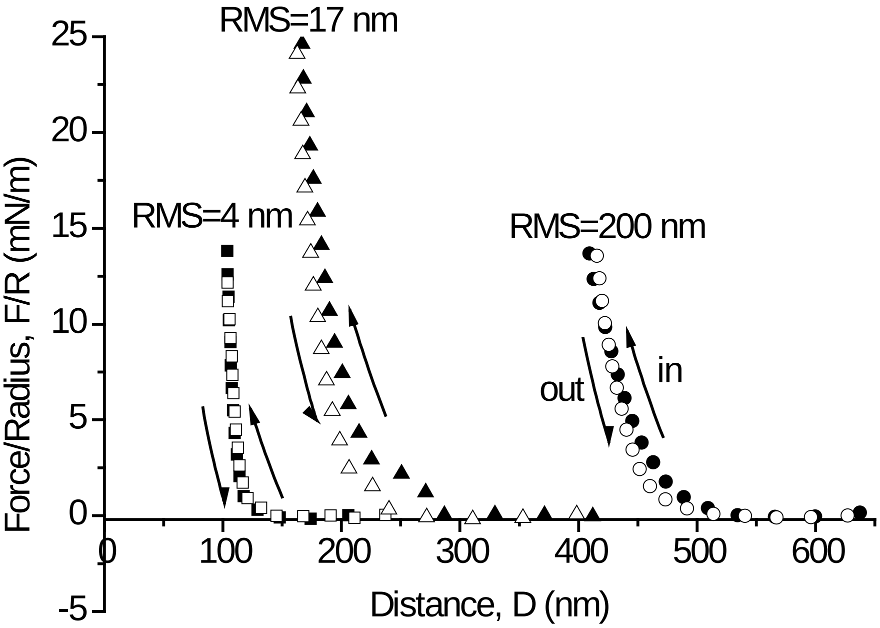

(a)

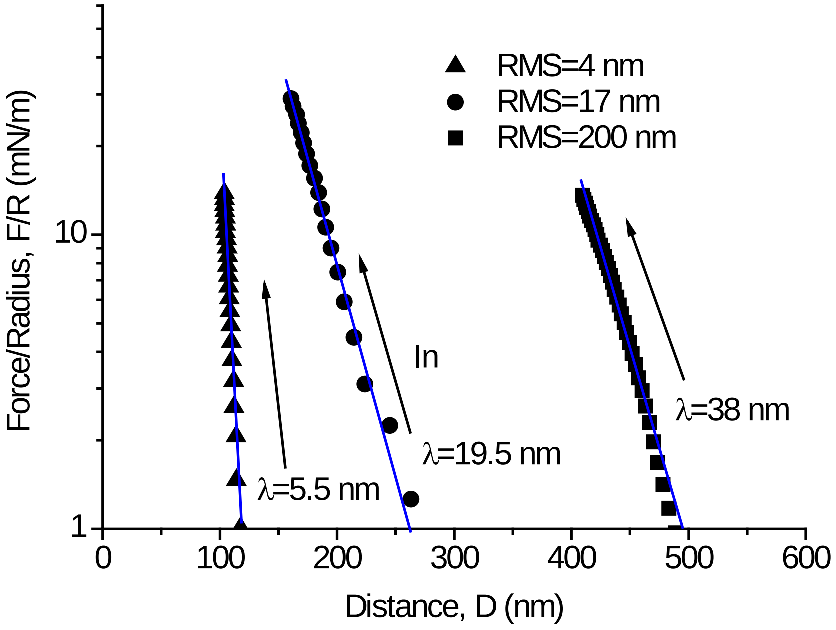

(b)

Figure 5.8 (a) Force-distance profiles of rough gypsum surfaces with different RMS in a linear plot. Filled symbols correspond to surfaces on approach (in) and open symbols on separation (out). (b) Same data on a semi-log plot to illustrate the exponentially repulsive force-distance regime.

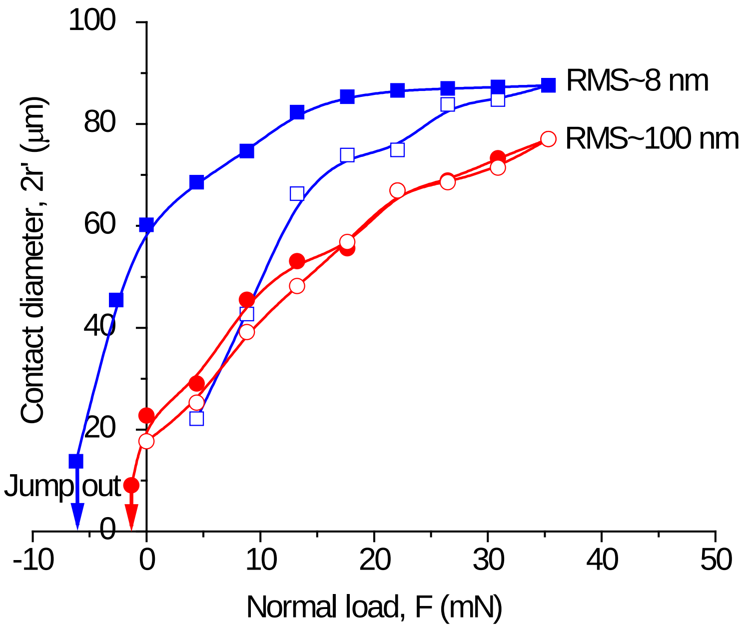

Figure 5.9 Contact diameter *vs.* applied normal load *F* (positive load corresponds to compressive force and negative load means adhesion force) for two sets of

gypsums with RMS of ~8 and ~100 nm. Open symbols correspond to surfaces on approach (loading or compression) and solid symbols on separation (unloading or decompression).

The contact deformation and adhesion between two elastic and smooth curved surfaces are normally described by the Johnson-Kendall-Roberts (JKR) theory.[39] It allows for the estimation of the adhesion energy from the measured adhesion force F_{ad} needed to separate the two contacting surfaces. For two crossed-cylindrical surfaces of radius R, F_{ad} is given by [17, 40]

$$F_{ad}=3\pi R\gamma=1.5\pi RW \qquad 5.6$$

where γ is the surface energy, and W is the work of adhesion ($W=2\gamma$). As mentioned above, no obvious adhesion was observed for two contacting rough gypsum surfaces when the applied maximum load was small (<0.5 mN). While increasing the maximum load applied, adhesive forces were observed during separation. Figure 5.9 shows the diameter of the flatten contact area *vs*. external load. A maximum load F=35.3 mN (F/R=1770 mN/m) or pressure ~4.5 MPa was applied to two pairs of rough gypsum surfaces with RMS of ~8 and ~100 nm. Based on Equation 5.6, an effective surface energy γ_{eff} can be obtained γ_{eff} =32.8 mJ/m^2 (W_{eff} =65.6 mJ/m^2) and γ_{eff} =7 mJ/m^2 (W_{eff} =14 mJ/m^2) for the gypsum surfaces with RMS of ~8 and ~100 nm respectively. The adhesion energies were found to increase with decreasing the RMS roughness of the gypsum coated surfaces, approaching the literature values for thermodynamic surface energy of gypsum 30-100 mJ/m^2,[41-44] which was also determined as γ ~48 mJ/m^2 for the freshly cleaved selenite (one variety of gypsum) plane in this study by contact angle measurement through the sessile drop method using three probe liquids one non-polar (diiodomethane) and two polar (dimethylsulfoxide and ethylene glycol) liquids (see Appendix).[45, 46] It should be noted that large gypsum crystal islands appeared as the gypsum coating became rougher with more dipping cycles, and the measured adhesion energies of deposited gypsum layers could be affected by not only the RMS roughness but also the surface coverage of gypsum crystals on mica.

The above surface forces and adhesion measurement for two randomly rough gypsum surfaces is the first study of its kind for rough crystal surfaces. Interestingly, our results on the exponential force-distance relation and effective adhesion energies increasing with lowering RMS roughness for crystal surfaces, are very close to the previous results on randomly rough soft polymer surfaces by Benz, *et al.*[26, 47] Our results further indicate that the exponential repulsion may generally exist for various kinds of randomly rough surfaces including organic polymer materials and inorganic crystal materials.

5.3.4 Greenwood-Williamson theory fitting

In order to further investigate the origin of the observed repulsive forces in Figure 5.8, a well-established contact mechanics theory for rough surfaces is employed to fit the force curves. Generally, the observed forces between two mica sheets coated with gypsum include attractive van der Waals force and repulsive elastic force arising from the contacting asperities upon exerting compressive force. If at least one of the two interacting surfaces is very rough, the real contact area will be small when they are in contact, and repulsive elastic force may overwhelmingly dominate over van der Waals force. Therefore, the contribution of van der Walls force to the interaction between such two contacting surfaces can be ignored, the observed force is purely elastic force due to asperities interactions,[24, 48] where the Greenwood-Williamson theory (referred as GW theory hereafter),[49] developed by Greenwood and Williamson to describe the contact of randomly rough surfaces, can be used to fit the repulsive force observed in an asymmetric geometry (rough gypsum surface against smooth mica surface) under low external load shown in Figure 5.10.

The GW theory can be applied to the contact between a plane and a nominally flat surface covered with a large number of asperities whose summits are all spherical. All summits are presumed to have the same radius *r*, and the height denoted as z of all asperities that are uniformly distributed across the surface follows a Gaussian distribution with mean height μ and standard deviation σ. The height distribution is given by

$$f(z) = \frac{1}{\sqrt{2\pi\sigma^2}} e^{\frac{-(z-\mu)^2}{2\sigma^2}} \quad 5.7$$

If the number of asperities in unit area (m^2) is known as n, the number N of asperities with height exceeding d in an area of A (m^2) will be (A and n can be considered as constant if the exerted force is not too big)

$$N(z > d) = \int_{d}^{d_{\max}} nAf(z)dz \quad 5.8$$

where $d_{\max}$ is the maximum height of all asperities.

Assuming the contact behaviour of each asperity on the rough surface follows the Hertzian equation,[50] the loading force of individual asperity can be given as a function of separation d between two surfaces

$$F_{individual} = \frac{4}{3} E r^{\frac{1}{2}} d^{\frac{3}{2}} \quad 5.9$$

where E is the plane stress modulus of the material.[25]

Assuming that the contact of individual asperity behaves independently, the GW theory gives the total interacting force as

$$F = \frac{4}{3} EAnr^{1/2} \int_{d}^{d_{\max}} (z-d)^{2/3} \frac{1}{\sqrt{2\pi\sigma^2}} \exp(-\frac{(z-u)^2}{2\sigma^2})dz \quad 5.10$$

.

The theoretical GW interaction curves compared with the experimental results are given in Figure 5.10, which shows that the prediction by the GW theory agrees with the experimental data reasonably well. The values of plane stress modulus of gypsum (E), mean height, radius of summit, and maximum height used in the theoretical calculation are given in Table 5.1. The theoretical plane stress modulus of gypsum (60−70 GPa) is close to the values reported in literature.[51] The experimental hard-wall distances for two samples, ~80 nm and ~200 nm, are close to the mean heights of the asperities (100 nm and 220 nm) used in the calculation in Table 5.1. The observed onset of the experimental repulsion forces at about 150 nm and 240 nm is the same as the theoretical values in Table 5.1. However, it should be noted that the GW theory will not be valid if the applied compressive force is too high or the deformations of asperities are too big, as the GW theory is the expansion of Hertzian model, of which the basic assumption is that the normal (squeezing) force must be small so that the real contact area is very small compared to the nominal contact area. The above analysis shows that the observed repulsive force for rough gypsum surfaces is mainly the elastic force due to asperity interactions.

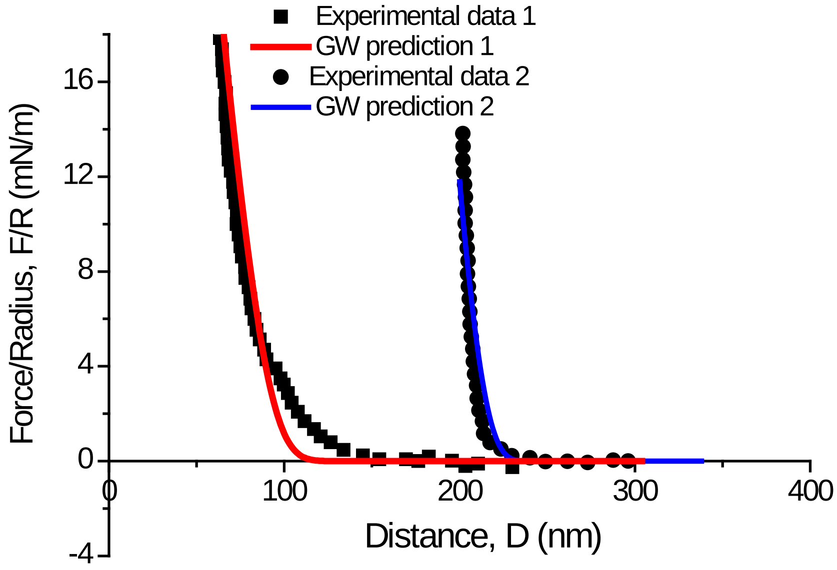

Figure 5.10 Theoretical interaction force-distance curves predicted by the Greenwood-Williamson theory for the experimental force-distance measurements (solid symbols) for two asymmetric cases (one rough gypsum surface interacting with a mica surface)

Table 5.1 Parameters used for GW theory prediction in Figure 5.10

	plane stress modulus of gypsum(E)/Gpa	standard deviation/nm	mean height/ nm	radius of summit/nm	maximum height/nm
GW prediction 1	60	10	100	5	150
GW prediction 2	70	15	220	25	240

5.4 Conclusions

In this study, the precipitation and crystallization of gypsum onto a silicate mineral (mica) was investigated through three coating methods: dropping, suspending and dipping. All three coating methods can lead to successful gypsum coatings on mica sheets, of which the dipping method gives the relatively smooth gypsum surface. The surface forces between two dip coated gypsum surfaces of various roughness were investigated in air by an SFA.

For the first time, exponential force-distance repulsion relation was obtained for the two randomly rough gypsum crystal surfaces after the initial contact during the loading-unloading force measurement, which is similar to the previous report on soft randomly rough polymer system. No obvious adhesion was observed between dip coated rough gypsum surfaces under low load (<0.5 mN), while adhesion forces was measured under higher load or pressure (~35 mN or 4.5 MPa) and the effective surface energies γ_{eff} were estimated as $\gamma_{\mathrm{eff}}=32.8$ mJ/m^2 ($W_{\mathrm{eff}}=65.6$ mJ/m^2) and $\gamma_{\mathrm{eff}}=7$ mJ/m^2 ($W_{\mathrm{eff}}=14$ mJ/m^2) for the rough gypsum surface with RMS of ~8 and ~100 nm respectively. The adhesion energies were found to increase with decreasing roughness of the coated gypsum surfaces, approaching the thermodynamic surface energy of gypsum ~48 mJ/m^2 estimated by a three-probe-liquid contact angle measurement, agreeing well with the literature value. The theoretical prediction by the Greenwood-Williamson theory agrees with the experimental results for surface interactions between a rough gypsum surface and a smooth mica sheet, which shows that the observed repulsive force for rough gypsum surfaces is mainly elastic force due to asperity interactions.

The surface forces between two silicate mineral surfaces (mica) in gypsum solutions of various concentrations were directly measured by SFA. The results agree well with the DLVO theory at low $CaSO_4$ concentrations (10^{-4}–10^{-2} M) but deviates from the theory at higher concentration, which may be due to nucleation/crystallization of gypsum crystals on mica and/or small particles in $CaSO_4$ solutions of high concentrations.

Our results are closely related to the complex interactions in sulphide minerals flotation and other industrial processes with gypsum and silicates involved in aqueous media, which provides an insight into the basic interaction mechanisms of gypsum, silicates and other mineral particles in mineral flotation processes.

Appendix:

Contact Angle Measurement of Gypsum Surface through Sessile Drop Method using Three Probe Liquids

Surface energy of a cleaved gypsum surface as the form of selenite, whose {010} plane is the particular crystallographic plane which can be cleaved by inserting razor blade parallel to {010} face, were derived using the sessile drop method based on the contact angles of the three probe liquids, including one non-polar (diiodomethane) and two polar (Dimethyl sulfoxide and ethylene glycol) liquids. Contact angles (θ) of the liquid droplets were measured on freshly cleaved gypsum surface, purged with nitrogen at room temperature and ambient humidity. Contact angles were measured within 5 sec after the droplet of probe liquid was dropped onto gypsum surfaces. The shape of the sessile drop was recorded and fitted by the computer and used to calculate the contact angle. The detailed three probe liquids method is shown below:

Surface energy γ, and the relative contributions to γ from Lifshitz–van der Waals (γ^{LW}) and Lewis acid base (γ^{AB}) components can be calculated by a method developed by van Oss *et al.* Surface tension can be given as

$$\gamma = \gamma^{\mathrm{LW}} + \gamma^{\mathrm{AB}}. \qquad 5.11$$

The AB component of the surface tension (γ^{AB}) is defined to comprise all electron-acceptor–electron-donor, or Lewis acid-base interactions, given by

$$\gamma^{\mathrm{AB}} = 2\sqrt{\gamma^{+}\gamma^{-}} \qquad 5.12$$

The LW, electron donor and electron acceptor components, γ^{LW}, γ^{-}, and γ^{+}, can be calculated from the contact angle measurement. When a drop of a liquid (L) is deposited on a solid surface (S), the contact angle between the drop and the surface (θ_L) is a function of the components and parameters of the surface tensions of the liquid (γ_L) and the solid (γ_S). The Young–Dupre equation describes the relations among these elements:

$$\gamma_{\mathrm{L}}(\cos\theta_{\mathrm{L}} + 1) = 2\sqrt{\gamma_{\mathrm{S}}^{\mathrm{LW}}\gamma_{\mathrm{L}}^{\mathrm{LW}}} + 2\sqrt{\gamma_{\mathrm{S}}^{+}\gamma_{\mathrm{L}}^{-}} + 2\sqrt{\gamma_{\mathrm{S}}^{-}\gamma_{\mathrm{L}}^{+}} \qquad 5.13$$

To solve the surface tension components of the solid, γ_S^{LW}, γ_S^-, and γ_S^+, three probe solutions must be used to yield three equations. Surface tension components for liquid, γ_L^{LW}, γ_L^-, and γ_L^+, are characteristic of the three probe liquids (i, ii, and iii); surface tensions of i, ii, and iii are designated $\gamma_i, \gamma_{ii}, \gamma_{iii}$, respectively. Substituting the values of γ_L^{LW}, γ_L^-, γ_L^+ and θ_L into Equation 13 and combining three equations together, we obtain a matrix to solve for the solid surface tensions γ_S^{LW}, γ_S^-, and γ_S^+:

$$\begin{bmatrix} \gamma_S^{LW} \\ \gamma_S^+ \\ \gamma_S^- \end{bmatrix} = \left\{ \left[2 \begin{pmatrix} \sqrt{\gamma_i^{LW}} & \sqrt{\gamma_i^-} & \sqrt{\gamma_i^+} \\ \sqrt{\gamma_{ii}^{LW}} & \sqrt{\gamma_{ii}^-} & \sqrt{\gamma_{ii}^+} \\ \sqrt{\gamma_{iii}^{LW}} & \sqrt{\gamma_{iii}^-} & \sqrt{\gamma_{iii}^+} \end{pmatrix} \right]^{-1} \begin{pmatrix} \gamma_i \ [\cos\theta_i + 1] \\ \gamma_{ii} \ [\cos\theta_{ii} + 1] \\ \gamma_{iii} \ [\cos\theta_{iii} + 1] \end{pmatrix} \right\}^2 \qquad 5.14$$

By using the above equations, one can determine Lifshitz-van der Waals (LW), and the acid and base components of surface energy of gypsum (CaSO4•$2H_2O$). The surface energy was determined as γ ~48 mJ/m^2 for freshly cleaved selenite plane.

Table A5.1 Three probe liquids for measuring the surface energy of gypsum [52]

Probing liquid	γ^{total}	γ^{LW}	γ^+	γ^-
Ethylene glycol	48.00	29.00	1.92	47.00
Diiodomethane	50.80	50.80	0.00	0.00
DMSO	42.97	29.20	0.20	237.00

Table A5.2 Surface energy of gypsum surface (freshly cleaved selenite plane)

	Contact angles (degree)			**Surface tension parameters (mJ/m^{-2})**				
	θ_{EG}	θ_{Dii}	θ_{DMSO}	γ^{LW}	γ^+	γ^-	γ^{AB}	γ^{total}
Gypsum surface	22.0	22.1	33.0	47.14	0.002	47.87	0.62	47.76

5.5 References

[1] P. Broman, Complex Sulphide Ores, (1980) 28-39.

[2] S. Rao, J. Finch, Minerals Engineering, 2 (1989) 65-85.

[3] M. Moignard, R. James, T. Healy, Australian Journal of Chemistry, 30 733-740.

[4] C. Sui, F. Rashchi, Z. Xu, J. Kim, J.E. Nesset, J.A. Finch, Colloids and Surfaces A: Physicochemical and Engineering Aspects, 137 (1998) 69-77.

[5] B. Nanthakumar, D. Grimm, M. Pawlik, International Journal of Mineral Processing, 92 (2009) 49-57.

[6] M.J. Pearse, Minerals Engineering, 18 (2005) 139-149.

[7] S. Mathur, P. Singh, B. Moudgil, International Journal of Mineral Processing, 58 (2000) 201-222.

[8] R.M. Beauchamp, Choung, J.W., and Xu, Z., , Interfacial Phenomena in fine particle technology, (2006) 101-116.

[9] M.I. Al-Wakeel, C.L. Lin, J.D. Miller, Minerals Engineering, 22 (2009) 244-253.

[10] F. Ikumapayi, B. Johansson, K.H. Rao, in, Luleå: Luleå tekniska universitet, 2010.

[11] G. Levay, R.S. Smart, W.M. Skinner, Journal of the South African Institute of Mining and Metallurgy, 101 (2001) 69-75.

[12] F. Rashchi, Z. Xu, J. Finch, Colloids and Surfaces A: Physicochemical and Engineering Aspects, 132 (1998) 159-171.

[13] R.D. Cody, H.R. Shanks, Journal of Crystal Growth, 23 (1974) 275-281.

[14] A. DiFeo, S.R. Rao, J.A. Finch, Minerals Engineering, 17 (2004) 557-559.

[15] F. Ostendorf, C. Schmitz, S. Hirth, A. Kuhnle, J.J. Kolodziej, M. Reichling, Nanotechnology, 19 (2008).

[16] J.N. Israelachvili, G.E. Adams, Journal of the Chemical Society-Faraday Transactions I, 74 (1978) 975-&.

[17] H.B. Zeng, N. Maeda, N.H. Chen, M. Tirrell, J. Israelachvili, Macromolecules, 39 (2006) 2350-2363.

[18] H.B. Zeng, B.X. Zhao, J.N. Israelachvili, M. Tirrell, Macromolecules, 43 (2010) 538-542.

[19] E.E. Meyer, K.J. Rosenberg, J. Israelachvili, Proceedings of the National Academy of Sciences of the United States of America, 103 (2006) 15739-15746.

[20] H.B. Zeng, N. Pesika, Y. Tian, B.X. Zhao, Y.F. Chen, M. Tirrell, K.L. Turner, J.N. Israelachvili, Langmuir, 25 (2009) 7486-7495.

[21] N.S. Pesika, H.B. Zeng, K. Kristiansen, B.X. Zhao, Y. Tian, K. Autumn, J. Israelachvili, J. Phys.-Condes. Matter, 21 (2009).

[22] B. Zappone, K.J. Rosenberg, J. Israelachvili, Tribol. Lett., 26 (2007) 191-201.

[23] J. Israelachvili, N. Maeda, K.J. Rosenberg, M. Akbulut, J. Mater. Res., 20 (2005) 1952-1972.

[24] B. Persson, Physical Review Letters, 87 (2001) 116101.

[25] B. Persson, Surface Science Reports, 61 (2006) 201-227.

[26] M. Benz, K. Rosenberg, E. Kramer, J. Israelachvili, J. Phys. Chem. B, 110 (2006) 11884-11893.

[27] K. Duan, A. Tang, R.Z. Wang, Materials Science & Engineering C-Biomimetic and Supramolecular Systems, 29 (2009) 1334-1337.

[28] J.N. Israelachvili, Intermolecular and surface forces, 2nd ed., Academic Press, London, 1991.

[29] J. Israelachvili, Y. Min, M. Akbulut, A. Alig, G. Carver, W. Greene, K. Kristiansen, E. Meyer, N. Pesika, K. Rosenberg, H. Zeng, Reports on Progress in Physics, 73 (2010).

[30] E.A. Abdel-Aal, M.M. Rashad, H. El-Shall, Crystal Research and Technology, 39 (2004) 313-321.

[31] N. Alcantar, J. Israelachvili, J. Boles, Geochimica et Cosmochimica Acta, 67 (2003) 1289-1304.

[32] R.M. Pashley, Journal of Colloid and Interface Science, 83 (1981) 531-546.

[33] R. Pashley, J. Israelachvili, Journal of Colloid and Interface Science, 97 (1984) 446-455.

[34] M. Kohonen, M. Karaman, R. Pashley, Langmuir, 16 (2000) 5749-5753.

[35] T. Lilley, C.C. Briggs, Proceedings of the Royal Society of London. A. Mathematical and Physical Sciences, 349 (1976) 355.

[36] J. Beretka, J.W. Van Der Touw, Journal of Chemical Technology & Biotechnology, 44 (1989) 19-30.

[37] A.J. Lewry, J. Williamson, J. Mater. Sci., 29 (1994) 5279-5284.

[38] B. Persson, S. Gorb, Journal of Chemical Physics, 119 (2003) 11437-11444.

[39] K. Johnson, K. Kendall, A. Roberts, Proceedings of the Royal Society of London. Series A, Mathematical and Physical Sciences, 324 (1971) 301-313.

[40] H. Zeng, Y. Tian, B. Zhao, M. Tirrell, J. Israelachvili, Macromolecules, 40 (2007) 8409-8422.

[41] M.R. Christoffersen, J. Christoffersen, M.P.C. Weijnen, G.M. Vanrosmalen, Journal of Crystal Growth, 58 (1982) 585-595.

[42] W. Wu, in: Department of Chemistry, State Uni¨ersity of New York at Buffalo, Buffalo, 1994.

[43] W. Wu, G.H. Nancollas, Advances in Colloid and Interface Science, 79 (1999) 229-279.

[44] F. Alimi, H. Elfil, A. Gadri, Desalination, 158 (2003) 9-16.

[45] C. Van Oss, Colloids and Surfaces A: Physicochemical and Engineering Aspects, 78 (1993) 1-49.

[46] D. Kwok, Y. Lee, A. Neumann, Langmuir, 14 (1998) 2548-2553.

[47] C. Yang, B.N.J. Persson, J. Israelachvili, K. Rosenberg, Epl, 84 (2008).

[48] K.N.G. Fuller, D. Tabor, Proceedings of the Royal Society of London Series a-Mathematical Physical and Engineering Sciences, 345 (1975) 327-342.

[49] J. Greenwood, J. Williamson, Proceedings of the Royal Society of London. Series A, Mathematical and Physical Sciences, 295 (1966) 300-319.

[50] S. Timoshenko, Engineering societies monographs, (1951) 506 p.

[51] I. Yilmaz, G. Yuksek, International journal of rock mechanics and mining sciences, 46 (2009) 803-810.

[52] C. Della Volpe, S. Siboni, Journal of colloid and interface science, 195 (1997) 121-136.

Chapter 6 Selective precipitation of gypsum on functional surface

6.1 Introduction

Water is a process medium in mineral processing. Most minerals processing plants are practicing reclamation of process water to reduce the consumption of fresh water, and high level of salinity is frequently experienced in the recycled water. For example, calcium ion concentration exceeds 2.5×10^{-2} M (1000 ppm) in some process water [1]. The Ca^{2+} mainly comes from dissolution of calcium-containing minerals and the addition of lime as a pH modifier and pyrite depressant[1]. A high concentration of sulfate ions (SO_4^{2-}) also exists in the process water of sulfide flotation plants owing to either oxidization of sulphide or addition of zinc sulphate and copper sulphate as deactivator and activator in the case of sphalerite flotation [2]. When a recycled water stream with a high concentration of calcium (Ca^{2+}) and sulphate (SO_4^{2-}) ions is incorporated in the process, potential precipitation of calcium sulfate dihydrate ($CaSO_4{\bullet}2H_2O$, referred to as gypsum hereafter) on both desired sulfide minerals and silicate gangues makes both mineral surfaces of same surface characteristics, thus decreasing the selectivity and flotation recovery [3, 4]. The presence of large amount of gypsum also causes serious scaling on the internal walls of pipes or heat exchangers [5], which leads to an increase in energy consumption and downtime for equipment maintenance. Therefore, an intuitive idea to solve this problem is to remove calcium and sulfate ions from the process water. Two approaches have been reported to remove gypsum: 1) remove calcium ion before gypsum precipitation (adding carbonate or carbon dioxide to form calcium carbonate precipitates) [1]; 2) enhance the nucleation and crystallization of gypsum by adding seeds [6]. Although there are some industrial practices using either approach, the removal efficiency has been proved not sustainable due to the introduction of other ions into the system, high cost or aging problem of the added seeds.

Previous studies have suggested inorganic minerals can grow on functional surface, exhibiting different orientation and nucleation kinetics from the bulk nucleation[7, 8]. It is intriguing to investigate what functional surface would induce highest gypsum nucleation rate. Using such kind of functional surface, we can make gypsum selectively nucleate on desired particles by engineering the surface to be the same characteristic with the functional surface. In this study we report some preliminary results of this innovative strategy to remove calcium sulfate from the process water.

Alkanethiols with different functional end groups grown on gold surfaces were used as functional surfaces for this study, schematically shown in Figure 6.1. The nucleation and crystallization rate of gypsum on the above functionalized surfaces will be investigated using a quartz crystal microbalance with Dissipation (QCM-D). The fundamental principle of QCM-D is that the quartz crystal is oscillated at different resonance frequency for a short period of time, the driving current is then turned off and the decay-curve (or ringdown) is measured as the oscillation dampens. The shift of oscillation frequency is related to the mass change of the crystal. Therefore, one can study the real-time adsorption of molecules on crystal surface by measuring the changes in the oscillation frequency. The decay rate or dissipation factor is related to the elasticity and viscosity of the molecular layer on the sensor. By measuring the frequency and dissipation, it becomes possible to analyze the state of molecular layers bound to the sensor surface, their mass, thickness and structural (viscoelastic) properties in real-time with extremely high sensitivity.

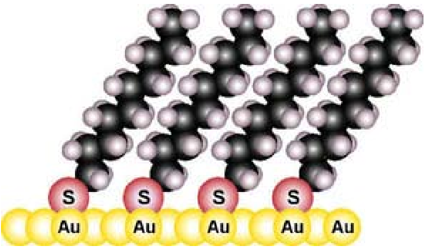

Figure 6.1 Schematic showing of self assembling of alkanethiol on gold [9]

6.2 Experimental

6.2.1 Materials

Calcium chloride and sodium sulfate solutions were prepared by dissolving $CaCl_2 \cdot 2H_2O$ (Fisher, 99.5%) and Na_2SO_4 (Fisher, 99%) in 18MΩ Milli-Q water. HCL (Sigma, 37%) and NaOH (Fisher, 99.7%) were used for pH adjustment. Three alkanethiols used to prepared functional surfaces in this study were 1-dodecanethiol (Sigma, 98%) 11-mercaptol-1-undecanol (sigma, 97%) and 12-mercaptododecanoic acid (Sigma, 96%). All of them were dissolved in anhydrous ethyl ethanol (Commercial Alcohol, Canada). Ammonia solution (Fisher, 30%) and reagent hydrogen peroxide (Fisher, 25%) were mixed with Milli-Q water at ratio of 1:1:5 to prepare cleaning solution for sensor cleaning.

6.2.2 Quartz crystal microbalance with dissipation (QCM-D)

Gypsum nucleation rate on functional surface was investigate using a quartz crystal microbalance with dissipation (E4, Q-sense AB, Gothenburg, Sweden) with the capacity of measuring changes in resonance frequency (Δf) and energy dissipation (ΔD) of QCM-D sensors at 8 different overtones simultaneously. The AT-cut crystals with gold coating on the top were also purchased from Q-sense. All solutions used in QCM-D measurement were left in ultrasonic bath for 10 minutes to ensure complete dissolution and degassing. For each measurement, a stable baseline (absolute variation is less than 1 Hz for at least 20 minutes) corresponding to Milli-Q water was achieved followed by injection of mixing solution of calcium chloride and sodium sulfate. All measurements were conducted under 22’C, and the flow rate was kept at 0.15ml/min.

Data modeling and analysis was carried out with Qtools 3.0, in which Sauerbrey model and viscoelastic model can be chosen to converte frequency change to mass change. When the new formed film on the surface of sensor is uniform, rigid and thin compared to the sensor itself, the dissipation value change ΔD is smaller than $1\ 0^{6}$ for a 10Hz frequency change. In this case, sauerbrey model is used as the form of Sauerbrey equation:

$$\Delta m = C\frac{\Delta f}{n} \qquad 6.1$$

Where Δm and Δf is mass and frequency change respectively, and n is the resonance number of sensors (1, 3, 5, 7, 9, 11, 13). C is a constant depends on the physical property of sensor (C=17.7ng/cm^2 in our system). In this study, overtone 3 is used.

If the adsorbed film is soft, indicating thickness and mass of the film is not ignorable, the Sauerbrey equation is not valid any more. The coupling between film and bulk liquid causes energy dissipation of system. The dissipation factor, ΔD, is the inverse of Q factor and defined by

$$\Delta D = \frac{E_{Dissipated}}{2\pi E_{Stored}} \qquad 6.2$$

Where $E_{\text{dissipated}}$ is the energy dissipated during one period of oscillation and E_{stored} is the energy stored in the oscillating system. During measurement the driving power of oscillator is switched on and off repeatedly, and resonance frequency is measured when oscillator is on; when it is switched off, the amplitude of oscillation decays as an exponentially damped sinusoidal function. Dissipation is calculated from the damping rate.

6.2.3 Self assembled monolayer preparation

Prior to use, the gold coated quartz crystal sensors (Q-Sense AB, Götenborg, Sweden) were put into UV Ozone for 10 minutes, cleaned and sonicated in "base Piranha" solution (30% Ammonia solution: 25% H_2O_2: Milli-Q Water=1:1:5) for 15 minutes at 75 °C, rinsed with Milli-Q water and dried with dry nitrogen. A self-assembled monolayer of alkanethiol on the gold coated quartz crystal sensors was prepared by immersing of a gold coated quartz crystal sensor into 1mM ethanolic solution of a ω-functionalized alkanethiol $HS(CH_2)_{11}X$ ($X=CH_3$, OH, COOH) for 24 hours at room temperature, and then was rinsed with ethanol and Milli-Q water.

6.2.4 QCM-D study of gypsum crystallization kinetics

The calcium sulfate solution was prepared in Milli-Q water at a concentration of 0.02M by mixing calcium chloride solution and sodium sulfate solution at equimolar amounts. More precisely, the calcium-containing and sulfate containing solutions were prepared by dissolving 0.588 g calcium chloride dihydrate and 0.568 g anhydrous sodium sulfate in 100ml Milli-Q water respectively. Before the QCM-D measurement, the calcium-containing and sulfate-containing solutions were put in an ultrasonic bath, filtered through 0.22μm filter (Millipore), and slowly mixed volume to volume to yield a aforementioned concentration of 0.02M, which corresponds to a gypsum supersaturation degree of 2 (base on Ksp(gypsum)=2.1×10^{-4}). The resulting pH of the mixing solution had a pH of 4.5, and it was adjusted to 7 after the mixing. The supersaturated solution did not yield any visible particles for at least 10 hours, which was also evident by conductivity measurement.

Upon mounting freshly cleaned functionalized sensor into the QCM-D chamber, Milli-Q water at a pH of 7 was flushed over the sensor surface for at least 20 minutes to establish a stable baseline. The prepared supersaturated calcium sulfate solution was pumped into the chamber at a flow rate of 0.15ml/min. A sharp frequency drop was observed at the initial 10 minutes, and the pump was stopped when a plateau was achieved after approximate 20 minutes. Then the chamber was sealed by putting two ends of the pumping pipe into water to prevent water inside the chamber from evaporating.

6.3 Results and discussion

6.3.1 Self assembled monolayer characterization

6.3.1.1 FTIR

The IR spectra of monolayer were obtained using a Polarization Modulation-Infrared Reflection Absorption Spectroscopy (PM-IRRAS) [10]. The PM-IRRAS measurements were performed on a Nicolet 6700 FT-IR spectrometer, equipped with an external tabletop optical mount, which included a photoelastic modulator (PEM) with a modulation frequency of 50 kHz, a synchronous sampling demodulator, and a MCT-A detector. The IR spectra were recorded with Omnic software by setting the PEM half-wave retardation at 1700 cm-1. 1000 scans were added and averaged for each spectrum with a resolution of

8 cm-1, and the beam incident angle was set to 80° to achieve a high signal-to-noise ratio. All IR spectra were collected at ambient conditions. Due to the phase modulation technique, no reference sample was needed in the experiments, and the random noise from moisture and CO2 was effectively suppressed.

Figure 6.2 and Figure 6.3 show the PM-IRRAS spectra at the region of interest. Base on the peak assignments given by Porter et al. [11], Figure 6.2: 2923 cm^{-1} and 2850 cm^{-1} are assigned to CH2 υ_a and υ_s respectively. 2966 $cm^{-1}$and 2877 cm^{-1} are assigned to CH3 υ_a(ip) and $\upsilon_{s.}$ The peak at 1740cm^{-1} in Figure 6.2 is the stretching of C=O.

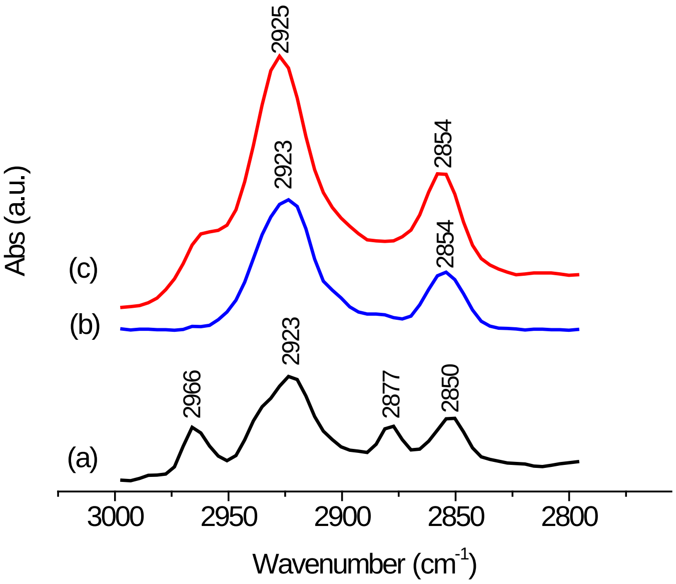

Figure 6.2 FTIR spectra showing the C-H stretching region of different alkanethiols adsorbed on gold: (a) HS-$(CH_2)_{11}$-CH_3; (b) HS-$(CH_2)_{11}$-OH; (c) HS-$(CH_2)_{11}$-COOH

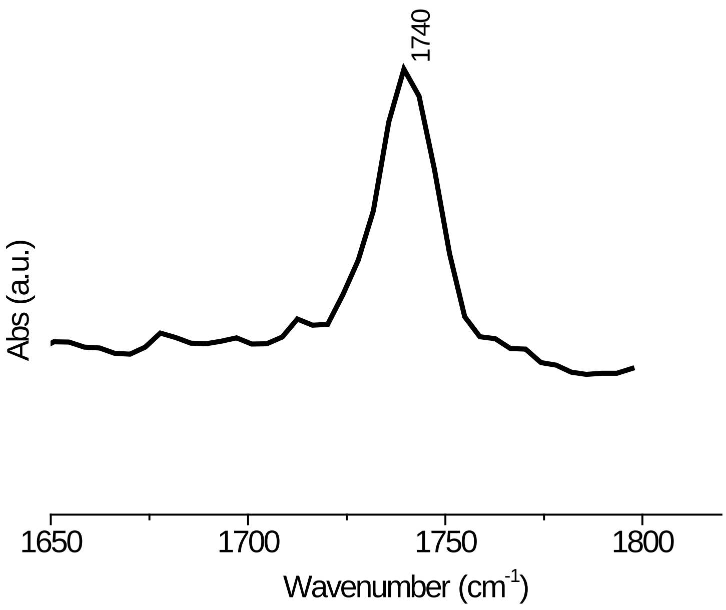

Figure 6.3 FTIR spectra showing the C=O stretching of HS-$(CH_2)_{11}$-COOH

6.3.1.2 Contact angle

Static contact angles of water on various functional surfaces were measured using a drop shape analyzer (DSA, Krüss, Germany) equipped with an optical microscope and illumination system. The sessile drop method with drop volume of 10-20 µL was employed at room temperature. Contact angles were measured within 5 sec after the droplet of probe liquid is dropped onto sample surfaces. The shape of the sessile drop was recorded and fitted by the computer and used to calculate the contact angle. The result is shown in Table 6.1.

Table 6.1 Contact angles of water droplet on functional surfaces

$HS(CH_2)_{11}X$	Contact angle
Bare gold sensor	15±6
$HS(CH_2)_{11}CH3$	94±9
$HS(CH_2)_{11}OH$	21±6
$HS(CH_2)_{11}COOH$	34±5

6.3.2 QCM-D

The result of QCM-D measurement of gypsum nucleation on functional surfaces from supersaturated calcium sulfate solution is showed in Figure 6.4. Among all three SAMs, COOH-terminated surface induced the highest growth rate of gypsum followed by OH-terminated surface. The nucleation of gypsum on both COOH-terminated and OH-terminated exhibited an induction periods, which were 9.5 hours and 10.5 hours, respectively. The formation of gypsum was inhibited on CH_3-terminated surface. It is reported that negatively charged surface induces the nucleation of inorganic minerals.

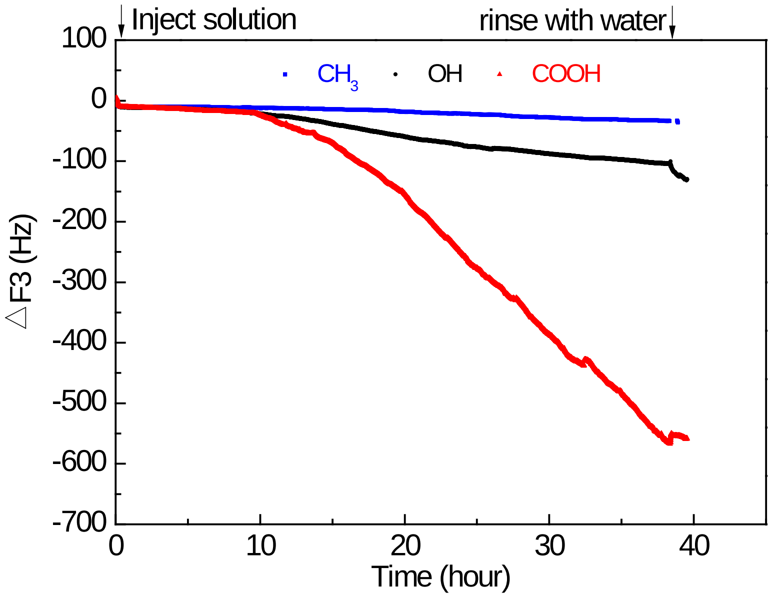

Figure 6.4 QCM-D measurement of gypsum growth on different functional surfaces. After mounting gold sensors treated with three different kinds of alkanethiol into QCM-D chamber, a stable baseline was established for 30 minutes. The mixing solution of $CaCl_2$ and Na_2SO_4 with a concentration of 0.029M was pumped into the chamber at the flowrate of 0.15ml/min. An initial ~10Hz drop was observed for all three functional surfaces. Stop the pump when the plateau was achieved at around 30 minutes. Obvious frequency drop was see on OH and COOH-terminated surfaces at the ninth hour.

6.3.3 Gypsum morphology

After the QCM-D measurement, the sensors were taken out from the chamber, rinsed with ethanol and dried with nitrogen. The morphology of formed crystals on the functional surface was observed with a confocal microscope (Axio CSM 700, Zeiss, Germany), and the images are shown in Figure 6.4. In Figure 6.4(b), only small rods were observed. Figure 6.4 (c) showed some 10-20μm long crystals with aspect ratio ~3 (L:W). Larger crystals with smaller aspect ratio were observed in Figure 6.4(d), some of them interlocked with each other.

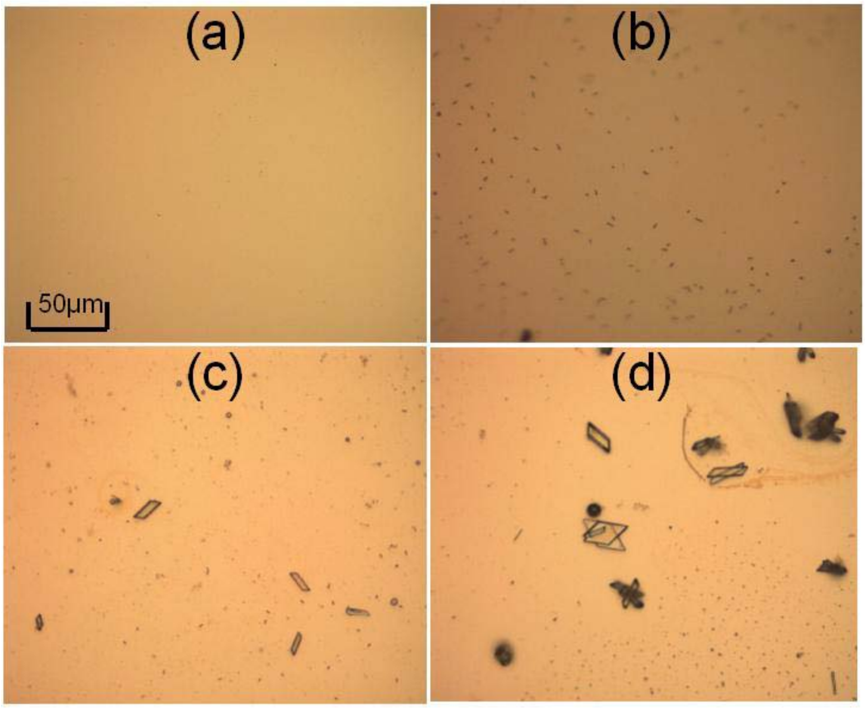

Figure 6.5 Optical micrographs of gold sensors (a) pure gold sensor, (b) gypsum crystal grown on CH_3-terminated SAM, (c) gypsum grown on OH-terminated SAM, (d) gypsum grown on COOH-terminated SAM.

6.3.4 Mechanism discussion

From previous reports and our own results, we know that negatively charged surface promotes the gypsum crystal formation on functional surface. The strength of interaction between calcium ion and functional groups, shown in Figure 6.5, is believed to determine the growth rate of gypsum on SAM. There is no interaction between calcium ion and CH_3 group as shown in Figure 6.6(a) so that the nucleation of gypsum on CH_3 terminated functional surface is not expected. The strong interaction between calcium ion and COOH group in Figure 6.6 (c) is found. Therefore, the nucleation of gypsum on COOH terminated functional surface is more favourable than other surfaces, which agrees with the QCM-D result in this study.

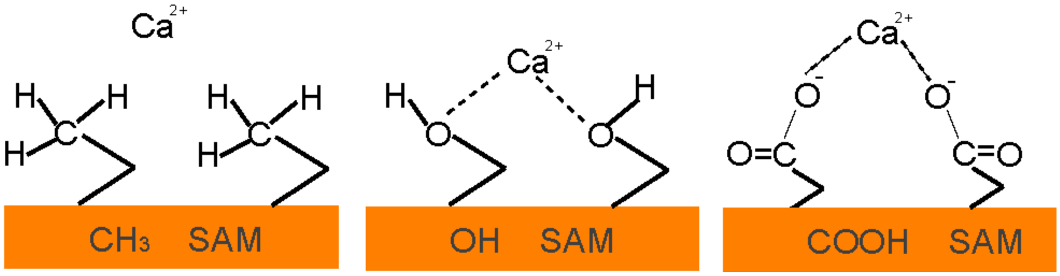

(a) (b) (c)

Figure 6.6 Interaction of calcium ions with functional groups on the SAM

6.4 Conclusions

We quantitatively measured the gypsum growth rate on functional surfaces using a QCM-D, and the results indicate that negatively charged surface (COOH-terminated) acts as potent substrate for gypsum nucleation. The grown crystals exhibit different orientation from the bulk crystallization.

6.5 References

[1] C. Sui, F. Rashchi, Z. Xu, J. Kim, J.E. Nesset, J.A. Finch, Colloids and Surfaces A: Physicochemical and Engineering Aspects, 137 (1998) 69-77.

[2] M.J. Pearse, Minerals Engineering, 18 (2005) 139-149.

[3] R.M. Beauchamp, Choung, J.W., and Xu, Z., , Interfacial Phenomena in fine particle technology, (2006) 101-116.

[4] S. Mathur, P. Singh, B. Moudgil, International Journal of Mineral Processing, 58 (2000) 201-222.

[5] Z. Amjad, Journal of colloid and interface science, 123 (1988) 523-536.

[6] J. Nyvlt, O. Söhnel, M. Matuchova, M. Broul, Amsterdam, New York, (1985).

[7] J. Aizenberg, A.J. Black, G.M. Whitesides, Nature, 398 (1999) 495-498.

[8] S. Mann, D.D. Archibald, J.M. Didymus, T. Douglas, B.R. Heywood, F.C. Meldrum, N.J. Reeves, Science, 261 (1993) 1286.

[9] http://dysa.northwestern.edu/Publications/TOC/2004_Witt_CurrOrgChem.jpg.

[10] M. Muro, Y. Itoh, T. Hasegawa, The Journal of Physical Chemistry B, 114 (2010) 11496-11501.

[11] M.D. Porter, T.B. Bright, D.L. Allara, C.E.D. Chidsey, Journal of the American Chemical Society, 109 (1987) 3559-3568.

Chapter 7 Conclusions and future work

7.1 Major conclusions

This study is the first of its kind to apply the QCM-D technique to investigate sphalerite activation, which indroduces a new *in-situ* approach to investigate surface adsorption and activation in many mineral processes and surface modifications. The major findings and conclusions of this thesis work are summarized as follows:

1) The zinc sulfide coating on ZnS sensor (Q-sense) used in this study has been shown to have similar surface properties to natural sphalerite.

2) QCM-D provides a unique *in-situ* approach for a systematic study of the zinc sulfide activation mechanism in various solution conditions through monitoring the real-time mass change on ZnS sensor with high sensitivity ~0.5 ng/cm^2.

3) The activation of ZnS sensor by silver was confirmed by the mass increase of ZnS sensor coupled with subsequent xanthate adsorption during QCM-D measurement, the change of surface wettability, and the presence of Ag_2S on the surface. The activation of zinc sulfide with silver at pH 5 was found to follow a two-stage kinetics: an initial rapid stage fitted well with a logarithmic function followed by a slower stage fitted using a parabolic equation. The above two-stage zinc-silver reaction kinetics implies that the first stage is a chemisorption process while diffusion is the rate-determined step in the later stage, which is evident by the penetration of silver atoms into bulk ZnS film through argon sputtering followed by XPS measurement on the activated ZnS surface.

4) It was found that zinc sulfide can be activated by copper at pH 6.5 and by lead at pH 6.5 and 9. The activation kinetics at pH 6.5 was fitted well with a pseudo-second order model, while the activation kinetics with lead at pH 9 could be fitted well with a pseudo-first order model for the initial rapid stage and the Elovich model for the second stage. The above activation kinetics

indicates zinc sulfide activation with copper and lead at pH 6.5 is a process of chemisorptions between hydrolysis species (mainly MOH^+) and zinc sulfide surface. At pH 9, the activation mechanism is more complicated and may involve physisorption initially and chemisorption in the later stage.

5) Xanthate does not adsorb onto zinc sulfide surface but adsorb on activated zinc sulfide, which increases the hydrophobicity of zinc sulfide. The adsorption of xanthate on activated zinc sulfide leads to monolayer coverage under acidic condition while more xanthate is adsorbed onto activated zinc sulfide under alkaline condition, which is attributed to either multilayer adsorption or increased surface area of zinc sulfide after activated at alkaline pH.

6) The adsorption of calcium on zinc sulfide surface was found to be reversible under neutral and alkaline condition. The presence of calcium did not affect the recovery of sphalerite although QCM-D measurement showed that calcium could retard the uptake of copper and adsorption of xanthate at neutral pH.

7) A tea-bag desliming approach was employed to observe the deposition of gypsum from supersaturated solution onto sphalerite surfaces. Gypsum crystals were observed on sphalerite surfaces using a scanning electron microscope, however theoretical analysis on the surface interaction energy showed that the nucleation of gypsum on sphalerite surface was not thermodynamically favorable. It requires further experimental investigation to determine if gypsum could nucleate on sphalerite surface.

8) The forces between two silicate mineral surfaces (mica) in calcium sulfate solution of different concentrations were directly measured by a surface forces apparatus (SFA). The force-distance profiles could be well fitted by the DLVO theory at low $CaSO_4$ concentration (10^{-4}-10^{-2} M) but deviates at higher concentration. Exponential force-distance repulsion relation was obtained for two rough gypsum crystal surfaces with root-mean-square (RMS) roughness

between 4 and 200 nm on approach and separation after the initial contact. The effective surface energies were estimated as γ_{eff} =32.8 and 7 mJ/m^2 for gypsum surfaces with RMS of ~8 and ~100 nm respectively, which increase with decreasing the RMS roughness, approaching the thermodynamic value ~48 mJ/m^2 estimated by a three-probe-liquid contact angle measurement. The repulsive force observed for rough gypsum surfaces was found to be mainly elastic force due to asperity interactions.

9) Monolayers (SAMs) of alkanethiols with -CH_3, -OH and -COOH terminal groups were self-assembled on gold QCM-D sensors. The functionalized QCM-D sensor surfaces were then applied to investigate the impact of above functional groups on the nucleation and growth of gypsum. It was found that gypsum was able to grow on the SAMs and the growth rates followed the order as -COOH>-OH>-CH3. The gypsum formation dependence on surface functional groups provides new insight into the development of novel technologies or selective nucleate seeds for selectively removing gypsum (or high Ca^{2+} and SO_4^{2-} ions) from mineral process water.

7.2 Suggestions for future work

7.2.1 Activation study with QCM-D

The present study provides a new tool to study the zinc sulfide activation, and the analysis of activation kinetics enhances the understanding of activation mechanism. However, there are still a lot of unanswered questions as to the effect of activator concentration on activation kinetics, competitive adsorption of different activators and the effect of impurity. Therefore, more work needs to be conducted as listed below:

1) Study the effect of activator concentration on activation kinetics. The theoretical analysis showed that the adsorption rate increased with solute concentration up to a “saturated” point. A QCM-D study of zinc sulfide activation with various activator concentrations needs to be performed at

acidic, neutral and alkaline pH. This investigation will not only enhance the understanding of activation mechanism but also provide the fundamental basis for choosing the optimum activation dosage in plant practice.

2) A molecular simulation of how activator atom adsorbs to zinc sulfide surface will help elucidate the activation mechanism and verify the conclusions that are drawn from QCM-D measurement of zinc sulfide activation in this study.

3) In most flotation plants, both copper and lead ions are present in the zinc circuit. Using an atomic analysis spectroscopy, Sun et al. found that there was no synergistic effect of copper and lead on zinc sulfide activation. Therefore, it is pertinent to investigate activation kinetics in the presence of copper and lead ions using a QCM-D.

7.2.2 Effect of calcium sulfate

A preliminary investigation of the role in sphalerite flotation was performed in the present study. Due to the complex mineral composition and solution chemistry, the effects of calcium sulfate may include ion adsorption, heteroaggregation of solid particles, nucleation& crystallization on mineral surfaces and complexion of calcium with chemical agents. Some of these effects have been studied in this study to some degree. Further studies on the following subjects would form a complete picture of the roles of calcium sulfate in sulfide flotation:

1) Micro-flotation study of the effect of calcium on sphalerite flotation in the presence cupric ions as activator with various concentrations

2) QCM-D study of the effect of calcium on activator uptake and xanthate adsorption under acidic and alkaline condition

3) Zeta-potential measurement of heteroaggregation of gypsum particles and unactivated/activated sphalerite particles

4) QCM-D study of gypsum nucleation on zinc sulfide surface

5) Self-assembled monolayers with three functional groups ($-CH_3$, -OH, -COOH) were prepared in the present work to study the selective precipitation of gypsum. The nucleation of gypsum on phosphate ($-PO_4$) or sulfate ($-SO_3$) terminated monolayers needs to be investigated with QCM-D.